

SURFACE AND INTERFACE MODIFICATION BY LOW ENERGY ION BEAMS

By

DIPAK BHOWMIK

(PHYS04201404008)

Variable Energy Cyclotron Centre, Kolkata

A thesis submitted to the

Board of Studies in Physical Sciences

In partial fulfillment of requirements

for the Degree of

DOCTOR OF PHILOSOPHY

of

HOMI BHABHA NATIONAL INSTITUTE



June, 2019

Homi Bhabha National Institute

Recommendations of the Viva Voce Committee

As members of the Viva Voce Committee, we certify that we have read the dissertation prepared by Dipak Bhowmik entitled "Surface and interface modification by low energy ion beams" and recommend that it may be accepted as fulfilling the thesis requirement for the award of Degree of Doctor of Philosophy.

Chairman - Dr. Vaishali Naik



Date: 28/6/19

Guide / Convener - Dr. Prasanta Karmakar



Date: 28/06/2019

Examiner – Dr. Dipak Kumar Goswami



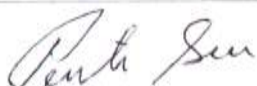
Date: 28/06/2019

Member 1- Dr. Dirtha Sanyal



Date: 28/6/19

Member 2- Dr. Pintu Sen



Date: 28/6/2019

Member 3- Dr. Biswarup Satpati



Date: 28/6/2019

Final approval and acceptance of this thesis is contingent upon the candidate's submission of the final copies of the thesis to HBNI.

I hereby certify that I have read this thesis prepared under my direction and recommend that it may be accepted as fulfilling the thesis requirement.

Date: 28/06/2019

Place: Kolkata

<Signature>

Co-guide (if applicable)



<Signature>

Guide

STATEMENT BY AUTHOR

This dissertation has been submitted in partial fulfillment of requirements for an advanced degree at Homi Bhabha National Institute (HBNI) and is deposited in the Library to be made available to borrowers under rules of the HBNI.

Brief quotations from this dissertation are allowable without special permission, provided that accurate acknowledgement of source is made. Requests for permission for extended quotation from or reproduction of this manuscript in whole or in part may be granted by the Competent Authority of HBNI when in his or her judgment the proposed use of the material is in the interests of scholarship. In all other instances, however, permission must be obtained from the author.


Dipak Bhowmik

DECLARATION

I, hereby declare that the investigation presented in the thesis has been carried out by me. The work is original and has not been submitted earlier as a whole or in part for a degree / diploma at this or any other Institution / University.



Dipak Bhowmik

List of Publications arising from the thesis

Journal

1. “Synthesis of nano-patterned and Nickel Silicide embedded amorphous Si thin layer by ion implantation for higher efficiency solar devices”, **D. Bhowmik**, S. Bhattacharjee, D. Lavanyakumar, V. Naik, B. Satpati, and P. Karmakar, **Applied Surface Science** (2017), 422 11-16.
2. “Physicochemical variation of mica surface by low energy ion beam irradiation”, **Dipak Bhowmik**, Prasanta Karmakar, **Nuclear Inst, and Methods in Physics Research B**, (2018), 422, 41–46.
3. “Dynamic scaling behavior of mica ripples produced by low energy Ar^+ ion erosion”, **Dipak Bhowmik**, Debasree Chowdhury, and Prasanta Karmakar, **Surface Science**, (2019), 679, 86-92.
4. “Presence of reactive impurities in Ar^+ ion beam plays a key role for Si ripple formation”, **Dipak Bhowmik**, Manabendra Mukherjee and Prasanta Karmakar, **Nuclear Inst, and Methods in Physics Research B**, (2019) 444, 54–61.
5. “Tailoring and investigation of surface chemical nature of virgin and ion beam modified muscovite mica”, **Dipak Bhowmik** and Prasanta Karmakar, **Surf. Interface Anal.** (2019), 51, 667–673.

Conferences Proceedings

1. **D. Bhowmik**, P. Karmakar, "Energy dependent ripple growth on Si (100) by N^+ ion beam irradiation Energy dependent ripple growth on Si (100) by N^+ ion beam irradiation", **AIP Conference Proceedings** 1832, 080019 (2017).
2. **Dipak Bhowmik**, Prasanta Karmakar, "Enhancement of optical absorption of Si (100) surfaces by low energy N^+ ion beam irradiation" **AIP Conference Proceedings** 1953, 100071 (2018).



Dipak Bhowmik

Dedicated to my mother

ACKNOWLEDGEMENTS

Finally, I am getting the opportunity to thank all for being a part of my doctoral journey. I would like to express my gratitude to those who have constantly helped me throughout the Ph.D. work.

I would first like to express my deep sense of gratitude to my thesis supervisor Dr. Prasanta Karmakar who has introduced me in the field of low energy ion beam induced pattern formation and guided me very carefully throughout the Ph.D. work. His immense knowledge on experimental technique and interpretation on any results really help me to learn a lot.

I am very much indebted to the directors of VECC, Prof. D.K. Srivastava, Prof. Alope Chakrabarty, Sri Amitava Roy, and Dean Academic Prof. Jane Alam for providing me the infrastructure and full-fledged facilities in the institute. I also thank Dr. Tilak Ghosh, Dean of Student Affairs, for the administrative co-operation.

I thank Dr. Vaishali Naik, Group Head of RIBF where I have got all the facilities for thesis work. I also thank Mr. D. Lavanyakumar of RIBF group for his constant help during the ion beam irradiation experiment. I acknowledge Mr. Chinmay Giri, Mr. Sanket Haque, Mr. Sayed Masum, and all other members of RIBF group for the help and fruitful accompany during irradiation experiment.

I would like to thank Dr. Biswarup Satpati, SINP for giving me the chance of cross-sectional TEM measurement. I am grateful to Prof. Manabendra Mukherjee, SINP for providing me the XPS measurements. I also thank Mr. Goutam Sarkar and Dr. Sukanta Barman for XPS measurements. I acknowledge Prof. Pintu Sen and Mr. Arghya Dutta for GIXRD measurement, and Prof. P.M.G. Nambissan and Smt. Soma Roy for optical measurements, respectively. I thank Mr. Abhijit Roy and Dr. Tapas Ghosh for their help during contact angle measurement.

I am thankful to Sampadi (Dr. Sampa Bhattacharjee), Debasreedi (Dr. Debasree Chowdhury), my seniors in lab, VECC for spending valuable time and their constant helps & encouragements. I thank my junior labmate Mr. Joy Mukherjee for the discussions. I also thank Mr. Subhas Ghosh.

I express my sincere gratitude to Prof. Rodolfo Cuerno of Catedrático de Universidad, Spain and Prof. R. Mark Bradley of Colorado State University, USA for valuable discussions on scaling theory of pattern formation by ion beam, and sharing his thoughts and helpful correspondence in understanding the mechanism of ion beam induced nanopatterning, respectively.

I thank to Ajit, Ashik, Homnath, Ranabir, Nachiketa, Samrangy, Shabnam, and Safikul, my classmates during doctoral course work (2014-2015) for their amazing accompany. I am thankful to all senior and junior scholars for spending good time with me in RRRSW. I thank the Table Tennis team (Homnath, Ajit, Arindamda, Santuda, Ayanda, Ashifda, Noor, Sumitda, Amalda, Sudipta) with whom I spent time.

Last but not the least, it would be impossible to complete without the support of my beloved Ma, Baba, and Dada. Thank you for your unconditional love, support, and encouragement. I also thank my all teachers who taught me from childhood. I thank my family members and close friends for encouraging a lot.

VECC, Kolkata

June, 2019


Dipak Bhowmik

Contents

	Page No
Synopsis	xi
List of Figures	xvi
List of Tables	xxiii
1. General Introduction	1
1.1 Introduction	1
1.2 Applications of ion beam modified surfaces and interfaces	3
1.3 Outline of this thesis	4
2. Theoretical background	6
2.1 Fundamentals of ion-solid interaction	6
2.1.1 Interatomic potential	6
2.1.2 Binary collision	8
2.1.3 Stopping of ions	8
2.1.4 Distribution of deposited energy	11
2.2 Sigmund's sputtering theory	13
2.3 Dependence of sputtering yield with ion energy and angle	14
2.4 SRIM and TRIM: Monte Carlo Simulation	16
2.5 Theory of ion beam induced surface pattern formation	17
2.5.1 Bradley and Harper model	18
2.5.2 Non-linear extension of BH theory	23

2.5.3	General continuum equation	25
2.5.4	Role of mass redistribution on ion-induced pattern formation	25
2.5.5	Effects of implants and impurities on pattern formation	28
2.6	Dynamic scaling theory for pattern formation	28
2.6.1	Dynamic scaling concept	28
2.6.2	Scaling theory for anisotropic surfaces	31
3.	Experimental procedures and characterization techniques	33
3.1	Low energy ion beam system for surface and interface modification	33
3.2	Characterization techniques	40
3.2.1	Atomic Force Microscopy (AFM)	40
3.2.2	X-ray Photoelectron Spectroscopy (XPS)	44
3.2.3	Transmission Electron Microscopy (TEM)	45
3.2.4	X-ray Diffraction (XRD)	48
3.2.5	Ultraviolet-Visible Spectroscopy	49
4.	Surface and near surface modification of Si by ion beam irradiation for photovoltaic and de-wetting applications	50
4.1	Synthesis of nano-patterned and plasmon active buried thin layer by ion implantation for higher efficiency solar devices	51
4.1.1	Introduction	51
4.1.2	Experimental	52
4.1.3	Results and discussions	53

4.1.4 Conclusion	62
4.2 Ripple pattern formation on Si by N ion bombardment, optical and wettability	
study of the patterned surfaces	63
4.2.1 Introduction	63
4.2.2 Experimental	65
4.2.3 Results and discussions	66
4.2.4 Conclusion	81
5. The modifications of muscovite mica surface by low energy ion bombardment	83
5.1 Dynamic scaling behavior of mica ripples produced by low energy	
Ar ⁺ ion erosion	84
5.2 Hydrophobicity study and change of chemical nature on ion bombarded	
mica surfaces	100
5.3 Detailed investigation of surface chemical nature of virgin and ion	
beam modified muscovite mica surface	108
6. Role of impurity in low energy Ar⁺ ion beam on Si ripple pattern formation	117
7. Summary and outlook	133
8. References	137

Synopsis

Low-energy ion beam sputtering (IBS) is a very important technique to modify surface and interface of a material and to develop periodic patterns on a large area solid surface at nanoscale level. Such types of periodic structures are very useful in the field of thin film growth, plasmonics, nanoscale magnetism, and catalyst [1-3]. The first periodic nanopattern formation was observed by Navez et al. [4] in 1962 on the glass surface by 4 keV air ion bombardment. Since that time, the ion beam induced pattern formation was studied extensively by both experimentally and theoretically for the basic understanding as well as potential applications. However, the detailed physical mechanism of pattern formation by ion beam sputtering (IBS) was not clear that time. Bradley and Harper [5] in 1988 proposed a successful model for explaining the periodic pattern formation based on Sigmund's sputtering theory [6]. However, the BH theory had some shortcomings to explain several experimental observations like the non-zero critical angle for ripple pattern formation, a saturation of ripple amplitude [7]. Later on, the effect of mass redistribution [8, 9], ion implantation [10], and the presence of external impurities was considered. Although a lot of works have been carried out, the complete understanding of ion-solid interaction and pattern formation are still needed. In this thesis, we have investigated surface nanopatterning and plasmon active buried layer formation on Si like important semiconducting surface for the application in solar devices, and the critical role of chemically reactive impurities in the projectile beam on the pattern formation. Also, the periodic pattern formation on mica like multi-elemental substrate and its detailed chemical modifications by ion bombardment are studied here.

The present thesis is devoted to the experimental study of surface and interface modifications of Si as well as muscovite mica in terms of periodic pattern formation by low

energy (3-12 keV) ion bombardment. The clean Si (100) and cleaved muscovite mica of size 1cm×1cm have been used for the irradiation. The irradiation was performed by 2.4 GHz ECR ion source of the Radioactive Ion Beam Laboratory at Variable Energy Cyclotron Centre, Kolkata with vacuum pressure maintained at $\sim 10^{-7}$ mbar. The surface morphologies of irradiated samples have been characterized by an Atomic Force Microscope (AFM). Also, the cross-sectional Transmission Electron Microscopy (TEM) is used to get the information below the surface. X-ray Photoelectron Spectroscopy (XPS) characterizes the detailed surface chemical composition and chemical change during the ion bombardment. Besides these, the X-ray Diffraction (XRD) for structural study, UV-Visible Spectrometer for optical study, and contact angle measurement for wettability study are used in this thesis. In parallel to the experimental study, we have carried out theoretical estimation based on the simulation package Stopping and Range of Ions in Matter (SRIM) [11]. In-depth statistical analysis of the growth of patterns with time is estimated using WSxM freeware [12].

In our studies, we have synthesized the nanostructure on Si surface and formed plasmon active thin buried layer for the potential application in higher efficient solar devices. We have bombarded 10 keV Ni^{1+} ion on Si (100) surface with fluence 1×10^{17} ions/cm² at normal incidence to achieve simultaneous amorphization, surface pattern and buried layer formation. The rim-surrounded crater like periodic nanostructure on Si has been observed by AFM study, whereas the amorphization and implanted buried layer just below the surface are detected by a cross-sectional Transmission Electron Microscope. Due to the plasmon active buried nickel silicide (Ni_2Si) layer formation, the surface shows an increase of optical absorption in the visible spectrum. The Ni_2Si layer acts as a good anti-reflecting electrode as well as an intermediary

between solar light and semiconductor for plasmon induced resonance energy transfer and direct electron transfer from plasmon to Si surface.

We have also studied the growth of ripple pattern and tunable hydrophobicity of Si surface due to 5-12 keV N^+ ion bombardment at an oblique angle incidence. Nitrogen being reactive, it reacts with Si surface during bombardment and forms silicon nitride (Si_3N_4) compound. The variation of the vertical and horizontal dimension of the ripple pattern with ion energy has been studied in detail. We have found an interesting fact that the experimentally observed ripple wavelength and surface rms roughness are directly proportional to the theoretically calculated lateral straggling and penetration depth of the ion, respectively. We have carried out the optical measurement of N bombarded Si surfaces, which shows the enhancement of optical absorption in the visible range compared to the pristine Si surface. The tuning of hydrophobicity in terms of ion beam parameters is discussed for N bombarded Si surfaces. We have found that the hydrophilic Si surfaces become hydrophobic due to ion-induced physical and chemical modifications.

Another important study has been carried out in this thesis is the physicochemical modification of muscovite mica [$KAl_2(Si_3Al)O_{10}(OH)_2$] like multi-elemental layered substrate by two types (Ar^+ & N^+) of ion bombardment. The naturally available mica can easily be cleaved to get an atomically flat crystalline surface, and it is very useful in many fields of atomic and molecular scale studies, such as atomic force microscopy calibration, supported lipid bilayers formation, DNA research, etc. [13-15]. We have observed well periodic ripple pattern formation on the mica surface by 12 keV Ar^+ and N^+ bombardment at an oblique ion incidence with different ion fluences. We have discussed the growth of ripple pattern in terms of continuum models as well as dynamic scaling theory. Mica being a layered substrate, the ion bombardment

leads to the depletion of upper K atoms, and the underlayer aluminosilicate is modified significantly. The negative aluminosilicate layer becomes active after ion bombardment and chemisorbs hydrocarbon from the ambient environment. The detailed modifications of the aluminosilicate layer are discussed by XPS studies. Due to the chemical and physical change of mica, the super-hydrophilic mica surface becomes hydrophobic after ion bombardment.

The most important finding in this thesis is the role of impurity in the low energy Ar^+ ion beam on Si pattern formation. The pattern formation by unintentional contaminations [16-19] and externally incorporated impurities during ion bombardment [20-23] has already been observed on Si surface, but the effect of impurity in the ion beam itself has not been considered before. We have explored this for the first time. We have investigated the pattern formation on Si by the mass analyzed pure and unanalyzed impure 3- 10 keV Ar^+ ion bombardment and exposed the role of beam impurities on Si ripple pattern formation. It has been observed that the pure mass analyzed Ar^+ beam cannot form pattern as reported earlier, but the mass unanalyzed Ar^+ ion beam, which is a mixture of Ar and other common reactive impurities (C, O and N) can easily form well defined periodic ripple pattern at oblique incidence. Our results will give a boost to study the beam purity and surface chemistry of the patterns, formed by the mass unanalyzed ion beam. It will also stimulate to expand the theoretical understanding by incorporating the effect of common impurities in the primary ion beam.

In summary, our experimentally observed results, presented in this thesis, are very useful in one hand for the fundamental understanding of pattern formation and ion-solid interaction; on the other hand, the study on plasmon active buried layer formation on Si and hydrophobicity study of mica can be used for photovoltaic device and interaction of biological substrates with the mica surface, respectively. The study of beam impurity will stimulate the low energy mass

unanalyzed ion beam users to investigate the surface chemistry and role of surface chemical change in the pattern formation in detail.

List of Figures

2.1: Schematic diagram of ion-solid interaction.

2.2: Energy loss with ion energy for N ion irradiation on a Si surface.

2.3: Schematic diagram of the random trajectory of the ion.

2.4: Schematic diagram of the energy distribution of an incident ion in the target.

2.5: Sputtering yield of Si surface by N bombardment at 60° with ion beam energy.

2.6: Sputtering yield of Si surface by 10 keV N bombardments with ion incidence angle.

2.7: Schematic diagram of energy deposition at different points which shows the different erosion rate at points in convex (trough) and concave (crest). The erosion rate is at trough (A,B and C is higher than crest (A',B' and C')).

2.8: variation of S_x and S_y with ion incidence angle for 10 keV N bombardments on Si.

2.9: Variation of curvature coefficients with incidence angle for 10 keV N bombardments on Si.

3.1: Schematic of ECR ion source and low energy ion separator.

3.2: Photography of low energy ion beam experiment set up in VECC Kolkata.

3.3: Schematic diagram of the ECR ion source.

3.4: Mass spectrum of ions on target chamber by 6 keV extraction volage from ECR ion source showing different ions extracted from ECR ion source.

3.5: Mass spectrum of ions on target chamber 6 keV extraction voltage from ECR to show Ag isotope separation.

3.6: *Sample holder for ion beam irradiation experiment.*

3.7: *Force distance curve of AFM operation.*

3.8: *Schematic diagram of the working principle of AFM.*

3.9: *Schematic diagram of the working principle of XPS.*

3.10: *Schematic diagram of TEM.*

4.1: *AFM topography of (a) bare Si(100) surface, (b) 10 keV Ni⁺ (fluence 1×10^{17}) bombarded Si(100) surface showing rim surrounded crater structure, (c) line profile along the marked line on (b), (d) The Power Spectral Density profiles of the bare and the irradiated Si, calculated from AFM data of (a) and (b).*

4.2: *Distribution profile of (a) implanted Ni atoms and (b) Si vacancy due to 10 keV Ni ion bombardment on Si at normal incidence (TRIM simulation); (c) Cross-sectional TEM view of 10 keV Ni⁺ ion implanted Si(100).*

4.3: *(a) cross-sectional scanning TEM (STEM) high angle annular dark-field (HAADF) image, (b) STEM-HAADF, Si-K, Ni-K and overlay map of Si and Ni generated from area 1 of (a), (c) Si-K and Ni-K X-ray line profiles along the line 2 of (a).*

4.4: *Cross-sectional STEM-HAADF and EELS spectra showing Nickel silicide formation during 10 keV Ni⁺ ion bombardment on Si (a) Cross sectional STEM-HAADF image for ion fluence of 1×10^{17} ions/cm², (b) Low-loss spectra at t positions 1, 2, 3 of (a), (c) Core-loss spectra at Ni-L_{2,3}-edge at position 4 of (a).*

4.5: *GIXRD spectra of Ni implanted Si samples.*

4.6: *Reflectance data showing a decrease in reflectance from bare Si, to Ni implanted Si.*

4.7: AFM images of (a) 5 keV, (b) 6 keV, (c) 7 keV, (d) 8 keV, (e) 9 keV, (f) 10 keV and (g) 12 keV N^+ bombarded Si surfaces at incidence angle 60° with ion fluence 7×10^{17} ions/cm². The arrow in the right corner indicates the ion beam direction.

4.8: The power spectral density (PSD) function for all the ion energies with wavevector (k) along the projection of ion beam direction.

4.9: Variation of (a) ripple wavelength (λ), (b) lateral straggling (β), (c) rms roughness (w) of the surface and (d) ion penetration depth (a) with ion energy (E).

4.10: (a) Schematic of N^+ ion beam implantation on Si surface and (b) 7 keV, 8 keV N^+ ions distribution in Si calculated from TRIM simulation.

4.11: AFM images of (a) pristine or Bare Si (100) and (b) 8 keV N bombarded Si surface showing the increase in surface area.

4.12: Absorption data of bare Si and 7 keV, 8 keV N bombarded Si samples showing an increase in absorption from bare Si, to N implanted Si. In the experiment the reflectance was measured. As the Si sample is opaque, no light was transmitted through it. The absorption is calculated by subtracting the reflected light from the incident light.

4.13: AFM images of (a) 5, (b) 8 and (c) 10 keV Ar bombarded Si surfaces at an oblique ion incidence 60° with the surface normal with ion fluence 7×10^{17} ions/cm². The arrow in the right corner of each AFM image indicates the ion beam direction.

4.14: (a) Schematic diagram of water droplet on rippled Si surface. The water droplet on (b) pristine Si, (c) 5 keV Ar bombarded and (d) 5 keV N bombarded Si surface showing the contact angle.

4.15: (a) Contact angle of 10 keV N bombarded Si surfaces with time. (b) Contact angle and rms roughness of pristine Si and Ar bombarded Si surfaces. (c) Contact angle and rms roughness of N bombarded Si surfaces with ion energy.

4.16: TRIM calculation of (a) N atoms distribution in Si for different energy, (b) Si vacancy for N bombardment, (c) Ar atoms distribution in Si and (d) Si vacancy for Ar bombardment at an incidence angle 60° with different ion energy.

4.17: Cross sectional TEM view of (a) 12 keV Ar and (b) 12 keV N bombarded Si surface with ion fluence 7×10^{17} ions/cm² at an incidence angle 60° with the surface normal.

4.18: Si 2p high resolution XPS spectra for (a) pristine Si, (b) 10 keV Ar bombarded Si surface and (c) 10 keV N bombarded showing Si₃N₄ formation.

5.1: AFM morphologies of (a) virgin mica, 12 kV Ar⁺ bombarded mica surfaces with ion fluences (b) 2×10^{17} , (c) 3×10^{17} , (d) 5×10^{17} , (e) 6×10^{17} , (f) 8×10^{17} , (g) 9×10^{17} , and (h) 1×10^{18} ions.cm⁻² at 60° with the surface normal. The FFTs ($50 \mu\text{m}^{-1} \times 50 \mu\text{m}^{-1}$) are shown in the corner of each AFM images. The arrow indicates the ion beam direction.

5.2: Dependence of (a) C_{11} and (b) C_{22} in Eq. (5.2) with ion incidence angle, using the parameters calculated from TRIM.

5.3: Log – log variation of ripple wavelength with ion fluence showing ripple coarsening at high fluence.

5.4: Variation of (a) interface width (rms roughness) with ion fluence, (b) correlation length along the ripple wave vector direction and (c) correlation length perpendicular to the ripple wave vector direction with ion fluence.

5.5: Log – log variation of interface width (W) with lateral correlation length (ξ_x).

5.6: Structure factors $S_{x,y}(k_{x,y})$ in the direction (a) parallel and (b) normal to the ion beam for mica at different fluences.

5.7: Collapsed structure factor curves using the values of z_x and z_y calculated from the slope of Figure 5.4 (b) & (c) in the direction (a) parallel and (b) normal to the ion beam for mica at different fluences.

5.8: AFM images of oblique incidence 12 keV N^+ irradiated mica surfaces with fluence (a) 5×10^{17} , (b) 7×10^{17} , (c) 1×10^{18} ions/cm². Variation of (d) roughness and (e) wavelength with ion fluence. The FFTs ($50 \mu m^{-1} \times 50 \mu m^{-1}$) are shown in the corner of each AFM images. The arrows indicate ion beam direction.

5.9: (a) Schematic diagram of crystalline mica. (b) X-ray Photoelectron Spectra (XPS) of virgin, 12 KeV N^+ and Ar^+ bombarded mica for ion fluence 5×10^{17} ions/cm². (c) XPS survey scan in C and K region. (d) Relative atomic concentrations in atomic percent (%) determined from XPS survey scan (Fig. 5.9b).

5.10: Sputtering yield calculation (TRIM) of different elements of mica for 12 keV Ar^+ and N^+ ions bombardment at oblique angle (60°).

5.11: (a) Schematic diagram of contact angle measurement. Droplets of water on (b) virgin mica surface, (c) 12 keV Ar^+ irradiated mica with fluence 3×10^{17} ions/cm² and (d) 12 keV N^+ irradiated mica surface with fluence 1×10^{18} ions/cm².

5.12: (a) Contact angle measurement with time for 12 keV Ar^+ bombarded mica surface (fluence 9×10^{17} ions/cm²). Contact angle variation with ion fluence for (b) 12 keV N^+ bombarded and (c) 12 keV Ar^+ bombarded mica surfaces.

5.13: (a) High resolution XPS spectrum of Ar 2p for Ar bombarded mica, (b) 12 keV Ar ions distribution in mica calculated by TRIM. (c) N 1s core level XPS spectrum showing Si_3N_4 and

AlN formation for N bombarded mica and (d) 12 keV N ions distribution in mica calculated by TRIM.

5.14 : *High resolution XPS spectra of Si 2p and Al 2p for (a) & (d) virgin mica, (b) & (e) 12 keV Ar bombarded mica and (c) & (f) 12 keV N bombarded mica respectively.*

5.15: *High resolution XPS spectra of C 1s and O 1s for (a) & (d) virgin mica, (b) & (e) 12 keV Ar bombarded mica and (c) & (f) 12 keV N bombarded mica respectively.*

6.1: *AFM images of mass analyzed Ar bombarded Si surface with ion energy (a) 3 keV, (b) 5 keV, (c) 8 keV and (d) 10 keV at oblique angle incidence 60° with constant ion fluence 7×10^{17} ions/cm². The arrow in each image indicates the ion beam direction and Z scale is shown with each image. (e) The RMS roughness of mass analyzed Ar bombarded Si surfaces with ion energy.*

6.2: *High resolution Si 2p core level spectra of virgin Si, 5 keV and 10 keV mass analyzed Ar bombarded Si.*

6.3: *(a) High resolution Ar 2p core level spectra of 5 keV mass analyzed Ar bombarded Si surfaces. (b) TRIM calculation of implanted Ar distribution for 5 keV Ar bombarded Si at 60° .*

6.4 : *AFM images ($5\mu\text{m} \times 5\mu\text{m}$) of without mass analyzed Ar bombarded Si surface with ion energy (a) 3 keV, (b) 5 keV, (c) 8 keV and (d) 10 keV at oblique angle incidence 60° with constant ion fluence 7×10^{17} ions/cm². The FFTs are shown in the corner of each image showing parallel mode ripple pattern formation. The $1\mu\text{m} \times 1\mu\text{m}$ scan AFM images are also shown in the upper corner of each AFM images. The arrows indicate the ion beam direction and also Z scale is shown near each image. (e) The surface RMS roughness and (f) ripple wavelength of mass unanalyzed Ar bombarded Si surfaces with ion energy.*

6.5: (a) XPS survey of virgin Si and ion bombarded Si surfaces with mass analyzed beam and without mass analyzed beam. (b) Atomic concentration of different elements in virgin Si, 10 keV mass analyzed and mass unanalyzed Ar bombarded Si surfaces calculated from XPS survey.

6.6: Mass spectrum on Si (100) sample by 5 keV source voltage extracted from ECR ion source.

6.7: High resolution Si 2p core level spectra of (a) 5 keV mass unanalyzed and (b) 10 keV mass unanalyzed Ar bombarded surfaces showing chemical compound formation.

6.8: High resolution C 1s core level spectra of (a) virgin, (b) 10 keV mass analyzed and (c) 10 keV mass unanalyzed Ar bombarded surfaces showing SiC formation. (d) Ar 2p core level spectrum for 5 keV mass unanalyzed Ar bombarded Si surface.

List of Tables

5.1: *Parallel mode ripple pattern on mica for different energy.*

5.2: *Some reported binding energies (eV) of Si 2p and their compounds along with the present experimental value.*

5.3: *Some reported binding energies (eV) of Al 2p and their compounds along with the present experimental values.*

5.4: *Some reported binding energies (eV) of C 1s, N 1s, O 1s and their compound along with the present experimental value.*

6.1: *% area of unreacted Si and its compounds from Figure 6.7 (a) & (b).*

6.2: *Some reported binding energies (eV) of Si 2p, C 1s and their compound along with the present experimental value.*

Chapter 1

General Introduction

1.1 Introduction

The bombardment of the energetic ion beam on solid surfaces has brought great importance for several purposes like surface cleaning, ion etching, thin film deposition, etc. The bombarding ion on a surface leads to the removal of surface material, which is called sputtering. Due to the sputtering of the target material by the energetic ion beam, the electronic configuration of the target surface is modified, and different properties like electrical, optical and magnetic property change precisely. This is a very common tool for surface modification. Another important consequence of ion bombardment is the formation of well-defined periodic nanopatterns like dot, rim, ripple, etc. on different semiconducting as well as insulating surfaces. The applications of ion beam sputtering (IBS) and implantation are not limited to that discussed above, but it has much other significance in different fields of material science research and industrial applications also. Interestingly, despite all these achievements in this field, there are many shortcomings, which need to be found.

The energetic ion sputters the atoms from the surface and penetrates in the solid surface during bombardment; as a result, it modifies the upper surface as well as the interface of a material. The main advantages of ion bombardment technique are the control in its concentration and implantation depth, which cannot be obtained by any other procedure. The use of energetic ions can introduce the interaction of several ions with a surface without depending on any thermodynamic factors. The reactive ion bombardment can also change the surface chemistry of

the target material. Thus, ion bombardment can simultaneously modify a surface physically in terms of forming a periodic pattern as well as chemically in terms of chemical reaction with the target atoms. Therefore, nanopatterned surface and buried thin layer can be formed on a semiconducting material by an easy single step process. The application of plasmon active buried layer will be discussed in this thesis. The nanopattern formation leads to increase in the effective surface area; as a result, light performs multiple reflections in the surface, which aids to trap the light in the surface. This property can be used to get an anti-reflective coating (ARC) surface. The adhesion property of a surface strongly influences the interactions of atoms and molecules on it. Therefore, the tuning of adhesion property of a surface for “in vitro studies of bio-surface interactions model surfaces” is very important [24]. The adhesion property is generally measured in terms of hydrophobicity i.e., water contact angle. The tailoring of hydrophobicity is controlled by surface texturing, surface chemical modification, and surface engineering. Researchers used to tune the hydrophobicity by several methods. However, the energetic ion bombardment has unique advantages for tuning hydrophobicity of a surface due to its precise control on surface texturing and chemical alteration.

As the energetic ion bombardment can form the well-defined periodic pattern on a solid surface, the clear understanding of the formation mechanism is important. The first periodic pattern formation by energetic ion bombardment on the solid surface was observed in 1962 by Navez et al. [4], and the first theoretical model for understanding the pattern formation mechanism was proposed by Bradley and Harper [5] in 1988. Later on, the experimental observation on pattern formation was explained by several advanced continuum models [25-27]. As an alternative approach, the dynamic scaling theory is also used to describe the nature of growth of the surface morphology as a function of ion fluence. In this approach, different scaling

exponents are calculated from the morphological growth, and these exponents values select the growth to a particular continuum model or give an idea for developing a new model. The important parameter on pattern formation is the purity of the ion beam, which can affect the pattern formation. It was already observed the effects of beam contamination on pattern formation [16-21, 23, 28, 29]. So the studies on beam purity and surface chemistry during ion bombardment are very important.

1.2 Applications of ion beam modified surfaces and interfaces

The modifications of surface and interface by low energy ion bombardment have several potential applications in many fields of material science research. The surface modification with controlled ion bombardment can be used to form well periodic nanopattern on semiconducting [30-33] as well as insulating [24, 34, 35] and metallic surfaces [36-38]. The ion beam modified and patterned semiconducting surfaces can be used as an antireflecting coating (ARC) and photovoltaic devices because of its increased optical absorption in the visible range [39]. The energetic ion bombardment can easily change the surface morphology as well as surface chemistry simultaneously [40-42]. Using this physicochemical change of a surface during ion bombardment, nanostructure on the surface and a thin buried plasmon active layer just below the semiconducting surface can be formed by plasmon active metallic ion implantation, which is useful for the application in photovoltaic purpose. The modified nano-rippled surface is used for trapping of liquid crystal, thin film deposition, and the growth of quantum dot, wires [43-45] etc. Also, the rippled substrates, which are formed by ion bombardment, can be used to enable the optical and magnetic anisotropy by Ag and Fe deposition on the ion-modified surface [46, 47]. Recently, biological study like the “controlled alignment of DNA origami” on ion modified nanopatterned surfaces is being initiated [48]. The DNA interaction with patterned surface

increases the biocompatibility of the surface, which can be used for biomedical devices [49]. The low energy ion bombardment can control the adhesive properties of different solid surfaces by changing the surface chemical composition [24]. Therefore, the low energy ion-induced surface and interface modification is a useful tool for tailoring the hydrophobicity. High energy (MeV) ion-modified surface, which can be formed micron order pattern on the metal surface, is useful for biocompatible device [50].

1.3 Outline of this thesis

This thesis explores the modification of surface and interfaces in terms of pattern formation and ion implantation by low energy (~ 10 keV) ion bombardment on Si and mica surface. We have chosen semiconducting Si surface due to its potential applications in electronic devices and insulating multi-elemental naturally available muscovite mica $[\text{KAl}_2(\text{Si}_3\text{Al})\text{O}_{10}(\text{OH})_2]$ surface due to its layered and atomically flat surface. Also both the materials are inexpensive compared to other materials. In this thesis, the presentation of our work has been arranged in seven chapters. The first chapter i.e., this chapter is mainly about the general introduction of the thesis, application of pattern formation by the ion beam, and outline of this thesis. Chapter 2 gives the detailed theoretical background of ion-solid interaction and different developed continuum models for pattern formation by ion bombardment. Also, the dynamic scaling theory of the growth of a surface is discussed in this chapter. Chapter 3 demonstrates the experimental and characterization techniques, which have been used. Chapters 4, 5, and 6 describe the main research works of the present thesis. In chapter 4, Si surface is patterned, and a plasmon active buried layer is formed by Ni^+ ion implantation. We have shown that the nanopatterned surface and the plasmon active buried layer enhance the absorption of solar light on the Si surface. Further, the growth of ripple patterns on Si by different energy N^+ ion bombardment is

illustrated, and the applications of patterned surfaces for antireflective coating and tuning hydrophobicity are discussed. Chapter 5 describes the detailed ripple pattern formation on mica surface by two types of ion bombardment, one is inert Ar^+ ion and another is chemically active N^+ ion. The physicochemical variation of mica by ion bombardment is discussed in detail. Also, the detailed chemical changes of Ar and N bombarded mica surfaces and chemical compositions of virgin mica are studied. In chapter 6, the critical role of beam impurity on pattern formation and beam induced chemical change are discussed. Lastly, in chapter 7, the summary of this thesis and the scopes of this study for future work in the continuation of the present work for the development of basic understanding in pattern formation are discussed.

Chapter 2

Theoretical background

When an energetic ion interacts with a solid surface, it loses its energy by transferring momentum to the atoms in the solid, and it penetrates a certain depth and then stops. The penetration depth depends on the mass of the projectile ion, target surface, and incident ion energy. The energy loss mechanism is held by two processes, one is nuclear energy loss and another is electronic energy loss. The first one dominates at lower energy (keV), whereas the second one dominates at higher energy (MeV). During this collision, some atoms from the upper surface of solid are removed, which is called sputtering. Also, the ion bombardment leads to process diffusion, emits secondary ionized particles, secondary electron, and the secondary photon. The ions also create defects in the crystal. The schematic of ion-solid interaction is depicted pictorially in Figure 2.1. The potential energy function for the ion-solid interaction is necessary, as one can get an idea about the rate of energy loss by ions from potential energy. The detailed effects of sputtering, mass redistribution, implantation, and impurities with ion energy, incident angle, and ion-induced pattern formation are discussed in this chapter.

2.1 Fundamentals of ion-solid interaction

2.1.1 Interatomic potential

In the ion-solid interaction, the interatomic potential between the ion and solid needs to know as the temperature, pressure, scattering probability of ion-atom are directly related to their interacting potential. Here, the interaction between those atoms is discussed, which is in equilibrium, but velocities and energies exceed the thermal motion. As a result, the range of

interatomic potential is limited within the equilibrium distance in solids. The interaction distance, however, will depend on the collision energy. Therefore, some amount of overlapping and interpenetration of closed-shell will occur, which leads to modify the particle wave function at the point of impact. So, the idea of interatomic potential at small separation is important for a clear understanding of the problems related to the ion-solid interaction and radiation damage.

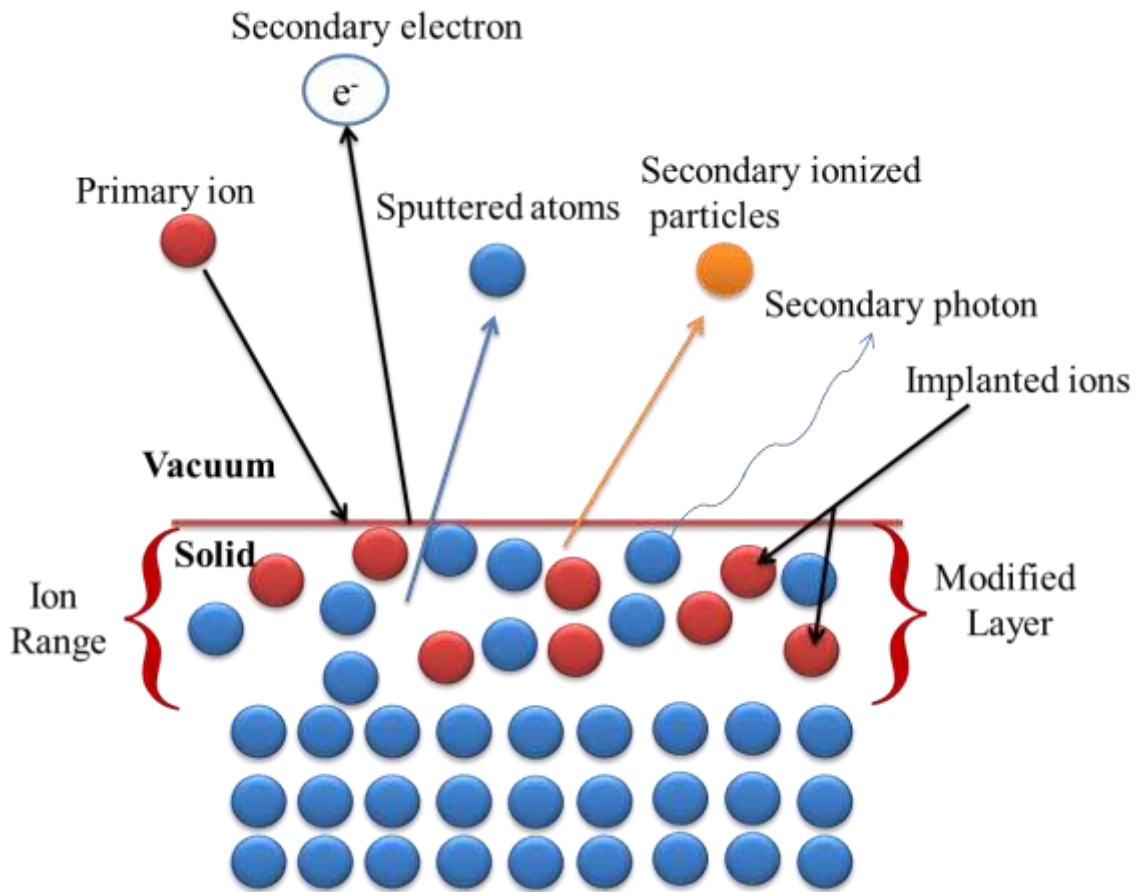


Figure 2.1: Schematic diagram of ion-solid interaction.

In the present case, as I will discuss mainly on low energy (few keV to 10's of keV) ion-induced surface modification throughout the thesis, I consider this energy range, which falls in the regime

$a_0 < r < r_0$, where a_0 , r , and r_0 are the Bohr radius of Hydrogen atom, separation between the colliding particles, and the separation between neighboring atoms in the crystal, respectively. In this regime, the potential energy leads to repulsion between two atoms, and the nuclear charge is screened by the electrons, which reduce the Coulomb potential. Thus, the interatomic potential between two atoms of atomic number Z_1 and Z_2 is

$$V(r) = \frac{Z_1 Z_2}{r} \chi(r) \quad (2.1)$$

where $\chi(r)$ is the screening function. It is defined as “the ratio of the actual atomic potential at some radius r to the Coulomb potential” [51]. For the large value of r , $\chi(r)$ should tend to 0, whereas for a small value of r , it should tend to 1.

2.1.2 Binary collision

When an energetic ion bombards a solid surface, it undergoes through a collision with the atoms in the solid. As a result, the incident ion loses its energy by momentum transfer to the atoms in solid. The energy of the ion is mainly lost by elastic i.e., nuclear interaction with ion and inelastic i.e., electronic interaction with ion. The incident ion penetrates the solid by gradually losing its energy and finally stops. It also creates primary recoil atoms in the solid and the recoiled atoms generate further recoils; thus forms a collision cascade. The collision can be treated as two body or binary collision where the mean free path of collision is much greater than the interatomic spacing. The detailed two-body collision is discussed in this reference [51].

2.1.3 Stopping of ions

(a) Energy loss of ions

During the collision of incident energetic ions with atoms and electrons in the solid, the incident ions lose energy at a rate dE/dx depending on the energy, mass, and the atomic number of ion and the substrate atom. Now, this energy loss is mainly dominated by “(i) nuclear loss in which the moving ion is transmitted as a translatory motion to the atom as a whole and (ii) electronic loss in which the moving particle excites the atomic electrons” [51]. Thus, the total rate of energy loss can be expressed as

$$\left(\frac{dE}{dx}\right)_{Tot} = \left(\frac{dE}{dx}\right)_n + \left(\frac{dE}{dx}\right)_e \quad (2.2)$$

The energy loss in the region of our interest is basically nuclear loss mechanism. The energy loss with ion energy, calculated by SRIM freeware [11], is shown for N^+ ion on Si surface in Fig. 2.2.

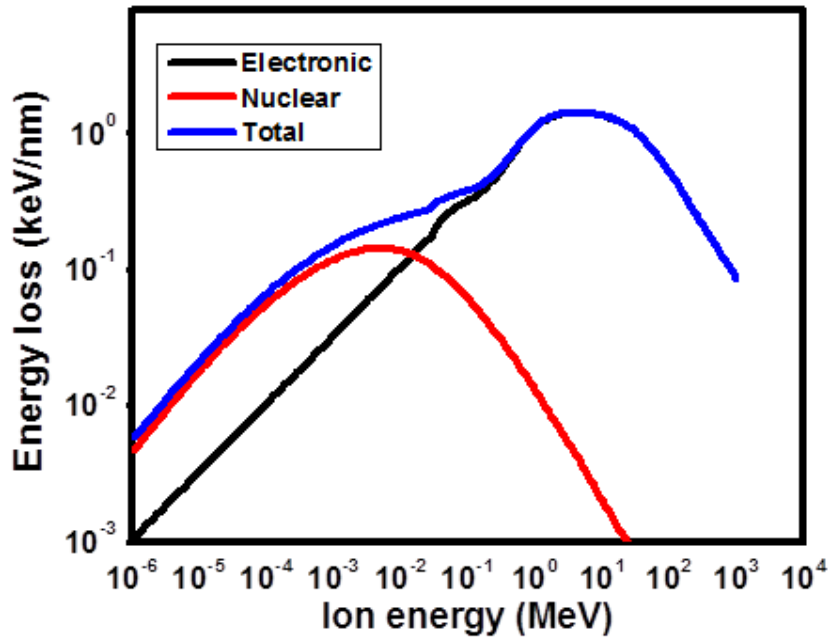


Figure 2.2: Energy loss with ion energy for N ion irradiation on a Si surface

It is found that the energy loss is dominated by the nuclear loss at ion energy range from eV to a few keV, and after that, the energy loss is dominated by the electronic loss. At higher energy, the

velocity of the ion is comparable to the Bohr's electron orbital velocity. As a result, the higher energetic ion interacts more with the electrons, and electronic energy loss dominates.

(b) Ion Range

As discussed above, the implanted ions lose energy by collision with the target atoms. After the consecutive collisions, when the incident ion loses all the energy, it stops. The distance upto which the ion penetrates from the upper surface is called range (R) of the ion. It is determined as

$$R = \int_{E_0}^0 \frac{1}{dE/dx} dE \quad (2.3)$$

where E_0 is the incident energy of ion, and the sign of dE/dx is negative as it decreases with the penetration distance. When the ion penetrates the target material, it follows the random trajectory as shown in Figure 2.3.

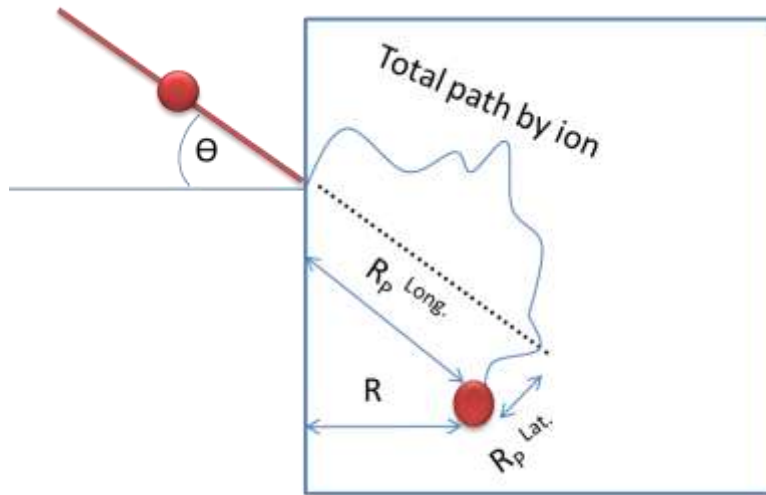


Figure 2.3: Schematic diagram of the random trajectory of the ion

The distance, travelled by the ion and energy loss, is also random. Hence, all the penetrated ions do not have the same depth, but they follow a distribution, which is called range distribution or

range straggling. The range distribution is mainly Gaussian. The total distance, travelled by the ion, is the path length, and the longitudinal range and lateral range from the end point of the trajectory are shown in Fig. 2.3. The range distribution can be calculated from the computer program Stopping Range of Ions in Matter (SRIM).

2.1.4 Distribution of deposited energy

The energy, deposited of an ion in a primary collision within a range dx for nuclear energy loss, is given by Winterborn et al. [52]

$$dE = S_n(E(x))dx = F_D(x)dx \quad (2.3)$$

where F_D is the energy distribution function with depth. $S_n(E)$ is the nuclear stopping cross-section. Sigmund derived the expression of $F_D(x)$ considering the linear collision cascade theory [6] and had shown that the average deposited energy at a point $r(x, y, z)$ in the target surface by an ion moving along the z -axis is :

$$F_D(r) = \frac{E}{(2\pi)^{3/2}\alpha\beta^2} \exp\left(-\frac{(z-h_0+a)^2}{2\alpha^2} - \frac{x^2+y^2}{2\beta^2}\right) \quad (2.4)$$

where E is the total energy deposited. The parameter a denotes the average penetration depth of ion. The parameters α and β indicate the width of the energy distribution along parallel (lateral) and perpendicular (longitudinal) direction of collision cascade, respectively. These parameters depend on the incident ion energy, ion mass, and also on the mass of the target atom. The distribution of deposited energy by the ion to the target atoms is shown in Figure 2.4. The ion range and straggling can be calculated from the computer simulation program SRIM. However, $F_D(x)$ cannot be calculated directly from SRIM. Although it is calculated from the number of displaced atoms extracted from SRIM. According to Bolse [53]

$$F_D(x) = n_v(x) \frac{E}{N_v} \quad (2.5)$$

Here, N_v and $n_v(x)$ are the total numbers of vacancy and vacancy density. These vacancies are generally created during ion bombardment and collision. If the transferred ion energy to the target atoms is greater than the displacement energy of that target atoms, there will create a vacancy by leaving the atoms from the lattice point, whereas the atom remains within the lattice as an interstitial atom if the transferred energy is less than the displacement energy of that atom. These interstitials and vacancies create the lattice defects at near surface regions of the solid at low energy ion bombardment as the ions can penetrate \sim nm range by the low energy ion bombardment. These defects after continuous bombardment lead to convert the crystalline surface to amorphous. The amorphous layer can be increased by increasing ion flux, ion energy etc.

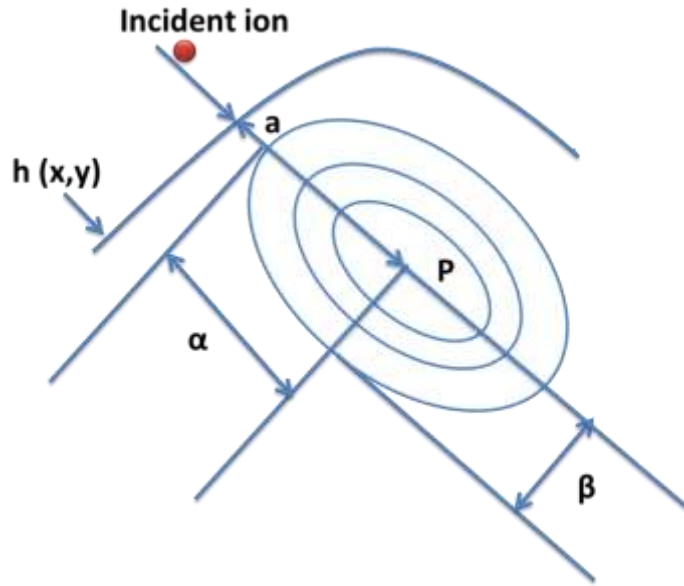


Figure 2.4: Schematic diagram of the energy distribution of an incident ion in the target.

2.2 Sigmund's sputtering theory

The most important theory of ion-solid interaction is Sigmund's sputtering theory. Based on this theory, different continuum models were developed to explain the ion beam induced surface pattern formation. Some basic assumptions like the homogeneous and isotropic target medium, the binary collisions, amorphous material, elastic collisions between ion-target, etc. were considered for developing the model. During the ion bombardment on a solid, an ion suffers a number of collisions with the atoms in the solid. The primary knock-on atom undergoes the secondary collisions and generates another recoiled atom. During this collision process, some atoms from the upper surface are removed, which is called sputtering or erosion of the surface. This sputtering is characterized by the parameter sputtering yield Y , which depends on the incident ion energy, mass, types of ions, target surface, and ion incident angle. The sputtering yield is defined as "the ratio of the number of emitted atoms from the target and the incident ions" [51]. According to Sigmund [6, 54], Y is proportional to the energy deposited in the target surface during an elastic collision as

$$Y(E, \theta) = \Lambda F_D(E, \theta) = \Lambda \alpha_I N \quad (2.6)$$

Here, $F_D(E, \theta)$ is the depth distribution function, which can be derived from the equation (2.4). θ is the angle of ion incidence with respect to the surface normal. α_I is a dimensionless function of mass ratio and θ . Λ is a material constant and is given by

$$\Lambda = \frac{3}{4\pi^2} \frac{1}{NC_0E_{sb}} \quad (2.7)$$

where N is the target atomic density, $C_0 = 0.018 \text{ nm}^2$ and E_{sb} is the surface binding energy.

2.3 Dependence of sputtering yield with ion energy and angle

The sputtering yield depends both on ion energy and incident angle. When the incident ion exceeds threshold energy, the sputtering of a surface is started. The sputtering yield of a surface increases first with increasing ion energy and then it decreases. The sputtering yield of Si with ion energy from 0 – 60 keV at incident angle 60° is calculated by SRIM and is shown in Figure 2.5.

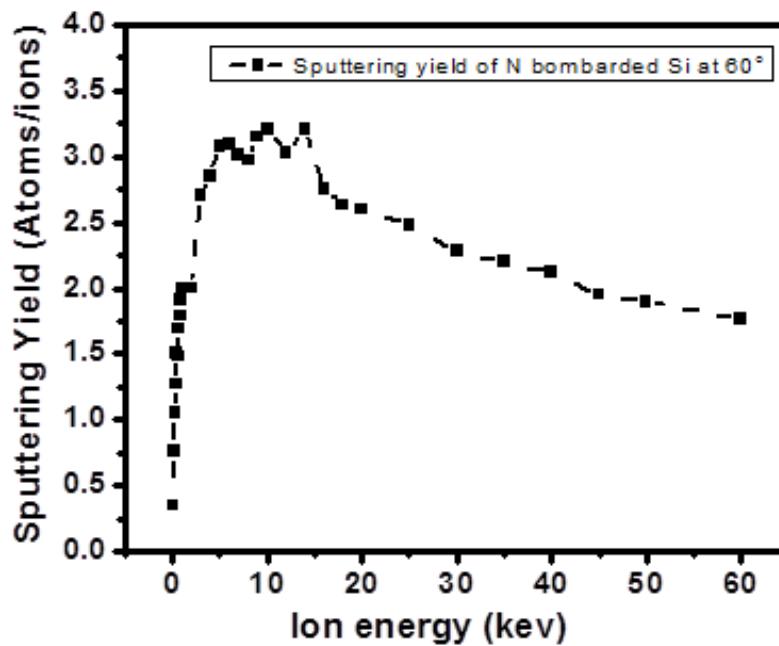


Figure 2.5: Sputtering yield of Si surface by N bombardment at 60° with ion beam energy.

Experimentally, it was also observed that sputtering yield increases with ion energy and at the higher incident energy it decreases [55, 56]. The sputtering yield of a surface increases with ion incident angle and reaches a maximum at a particular angle; after that, it decreases. The

sputtering yield of Si, calculated from SRIM for 10 keV N bombardments as a function of incident angle, is shown in Figure 2.6.

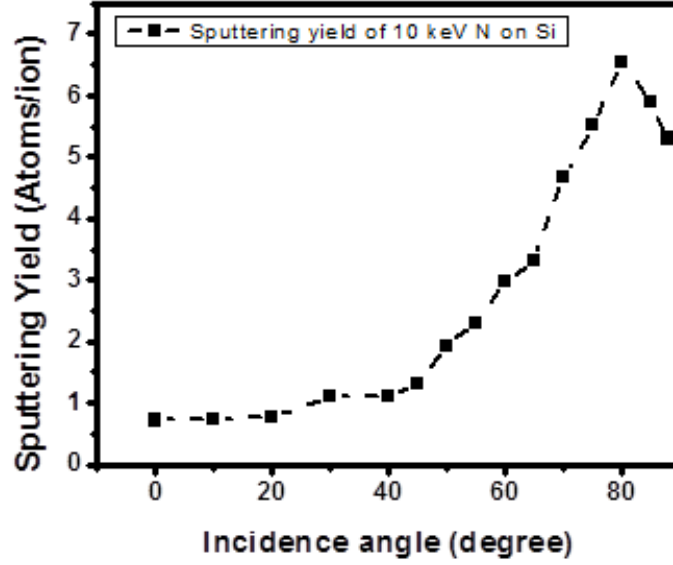


Figure 2.6: Sputtering yield of Si surface by 10 keV N bombardments with ion incidence angle.

Like the energy dependence, the angle dependence of sputtering yield is fitted with an algebraic formula [57] and compared with experimental data. Yamamura et al. [58] gave an empirical formula of sputtering yield as a function of an angle as

$$\frac{Y(E,\theta)}{Y(E,0)} = \frac{e^{f[1-1/\cos\theta]\cos\theta^*}}{\cos^f \theta} \quad (2.8)$$

where f and θ^* are the fitting parameters. The sputtering yield becomes maximum at the angle window 55° - 85° depending on the mass ratio of projectile ion, target, and ion energy. Sigmund [54] also gave formula on sputtering yield for normal incidence as

$$Y(E, \theta) = 0.042 \frac{\alpha_I S_n(E)}{E_{sb}} \quad (2.9)$$

and for oblique incidence

$$Y(E, \theta) = Y(E, 0)(\cos\theta)^{-b} \quad (2.10)$$

Here, b is the function of mass ratio, and the above formulas are valid in the region where the sputtering yield increases with ion energy.

2.4 SRIM and TRIM: Monte Carlo Simulation

SRIM (Stopping and Range of Ions in Matter) is free software for estimating the stopping power and range of ions in any solid material. The calculation is done using quantum mechanical treatment of ion-solid interaction. The statistical algorithms methods are used for the calculation. It is assumed that during the collision, the ion and atoms are bound in a screened Coulomb collision. The binary collision between ion and target atoms is considered in this simulation. SRIM can give the ion range and stopping power of ion in solid for a given ion energy, which are very close to the experimentally observed results. However, SRIM cannot give variation of the ion range with the ion incident angle and also this does not provide the ion distribution in target material, vacancy profile, and sputtering yield information.

TRIM (Transport and Range of Ions in Matter) is more comprehensive program, included in SRIM software, which gives the detailed profile of ions distribution, vacancy profile of target material, sputtering yield of atoms etc. TRIM can calculate the interaction of ion in compound materials up to eight layers. “It can also calculate the 3D distribution of ions and all the kinetic phenomena associated with the ion’s energy loss: target damage, sputtering, ionization, and phonon production” [11]. This software is free and easily available in internet (www.srim.org).

The use of SRIM/TRIM is also very easy. The programs are made so they can be interrupted at any time, and then resumed later.

The calculated ions range, distribution, and vacancy profile from TRIM are not very accurate as expected from experiment, but one can get an idea about the ions distribution, ion range and other parameter from TRIM. It is not only used in materials science but also used in the field of nuclear physics to estimate the ion penetration depth in the target.

2.5 Theory of ion beam induced surface pattern formation

In the previous section, Sigmund's sputtering theory was discussed briefly, but this theory did not explain the formation of nano-pattern on the solid surface by ion bombardment. Using this theory, Bradley and Harper (BH) in 1988 introduced a linear continuum model [5], which explained the periodic pattern formation successfully upto a certain extent. Although the Bradley and Harper (BH) theory was the first breakthrough for an understanding of periodic pattern formation from which new advancement of continuum models came into the scenario, but it had some limitations to explain some experimental observations like the non-zero critical angle for ripple pattern formation, the saturation of ripple amplitude [7]. These inadequacies were partially recovered by initially Cuerno et al. in 1995 [26] by deriving a nonlinear continuum equation of the Kuramoto-Sivashinsky (KS) type and then Makeev et al. [27] by adding some non-linear terms in BH theory, which physically signifies the slope dependence of local erosion yield. The pattern formation is explained fruitfully by linear BH theory upto a particular time after that non-linear terms control the pattern formation. Later on, Carter and Vishnyakov (CV) in 1996 [8] introduced the effect of mass redistribution, which could play an important role in pattern formation [9, 50, 59-68]. Further, Bradley and Hofsass introduced a theory of the effect of ion

implantation on the pattern formation, produced by ion bombardment on solid surfaces [69]. Our group also contributed some crucial observations like the role of initial surface roughness enhances the pattern formation very fast [70], projectile induced chemical change of the target generates the surface instability [41], the role of beam impurity [71]. However, the complete understanding of pattern formation is still under investigation. In these models, a partial differential equation of temporal evolution of height was considered. During the bombardment, the surface is far away from the equilibrium, and many other atomistic effects become effective.

2.5.1 Bradley and Harper model

Bradley and Harper developed the model, based on Sigmund's sputtering theory. When an energetic ion bombards the flat surface, the surface atoms are eroded, and the surface becomes curved. They showed in their theory that the erosion rate of different points on the surface is different. The schematic of erosion at a different point is shown in Fig. 2.7. The trough is eroded faster than the crest because the deposition of energy at point B is greater than that at point B', and the ions hit the point A contributes energy deposition to point B.

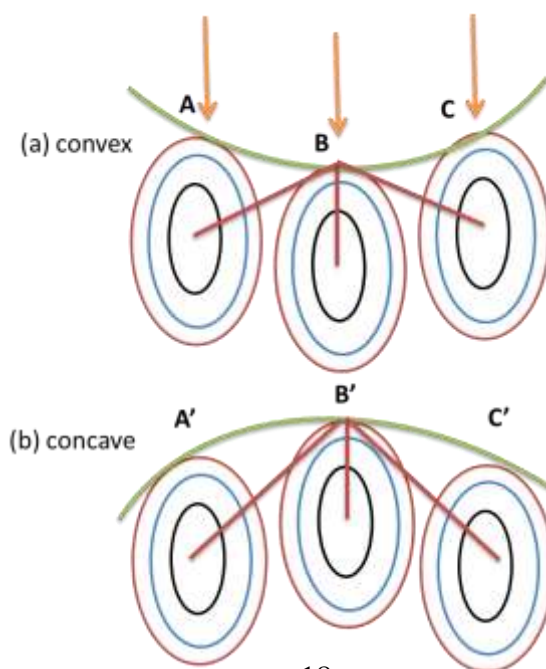


Figure 2.7: Schematic diagram of energy deposition at different points which shows the different erosion rate at points in convex (trough) and concave (crest). The erosion rate is at trough (A,B and C) is higher than crest (A',B' and C').

Now, for a flux of ions, the velocity of erosion at a point A or B can be calculated from the energy deposition (equation 2.4), contributed by all the ions as

$$\vartheta(A) = \Lambda \int \phi(r) F_D(r) \quad (2.11)$$

where $\vartheta(A)$ is the erosion velocity at point A, Λ is a constant as given in equation (2.7). $\phi(r)$ is a local correction of ion flux J, and $F_D(r)$ is the total energy deposited at a point as given in equation 2.4.

In order to explain the pattern formation, Bradley and Harper calculated the integral of equation (2.11) under the assumptions of large radii of curvature R_x and R_y and represented the time evolution of height $h(x, y, t)$ as

$$\frac{\partial h}{\partial t} = -\vartheta(\theta, R_x, R_y) \sqrt{1 + (\nabla h)^2} \quad (2.12)$$

where θ is the direction of the ion beam and surface normal; x and y represent the parallel and perpendicular to the ion beam projection. According to this theory, the pattern is evolved by the competition of the surface roughening via curvature dependent sputtering and surface smoothening via the thermally activated surface diffusion. The linear continuum equation of height, describing the surface pattern evolution, was given by BH [5] as

$$\frac{\partial h}{\partial t} = -\vartheta_0 + \vartheta'_0 \frac{\partial h}{\partial x} + S_x \frac{\partial^2 h}{\partial x^2} + S_y \frac{\partial^2 h}{\partial y^2} - K \nabla^4 h \quad (2.13)$$

Here, ϑ_0 is the “erosion velocity of the flat surface at normal incidence”, and ϑ'_0 is the “erosion velocity of in-plane motion of the surface structure” [5]. However, these two terms do not influence the pattern [27]. K denotes the thermally activated diffusion term. The above equation of height is valid only when the radii of curvature are much larger than the ion range a . S_x and S_y are the curvature dependent coefficients, which mainly control the surface pattern. The pattern will be formed in the direction parallel (x) and perpendicular (y) to the ion beam projection if $S_x < S_y < 0$ and $S_y < S_x < 0$, respectively, i.e., which value is more negative. S_x and S_y depend on the ion beam parameters as

$$S_x(\theta) = \frac{Ja}{N} Y_0(\theta) \left[\frac{A}{B_1} \sin\theta - \frac{B_2}{2B_1} \left(1 + \frac{A^2}{2B_1} \right) \cos\theta - \frac{AC}{B_1^2} \left(3 + \frac{A^2}{B_1} \right) \cos\theta \right] \quad (2.14)$$

$$S_y(\theta) = - \frac{Ja}{N} Y_0(\theta) \left[\frac{\beta^2}{a^2} \left(\frac{B_2}{2} + \frac{AC}{B_1} \right) \cos\theta \right] \quad (2.15)$$

where J is the ion flux, $Y_0(\theta)$ is the angle-dependent sputtering yield and

$$A \equiv a_\alpha^2 \sin\theta, \quad (2.16)$$

$$B_1 \equiv a_\alpha^2 \sin^2\theta + a_\beta^2 \cos^2\theta, \quad (2.17)$$

$$B_2 \equiv a_\alpha^2 \cos\theta \quad (2.18)$$

$$C \equiv \frac{1}{2} (a_\beta^2 - a_\alpha^2) \cos\theta \sin\theta \quad (2.19)$$

$$a_\alpha = \frac{a}{\alpha} \text{ and } a_\beta = \frac{a}{\beta} \quad (2.20)$$

All the parameters can be calculated with the help of SRIM or SDTRimSP. To see the variation of S_x and S_y with ion angle, these two coefficients are plotted for 10 keV N bombardments on Si surface and shown in Figure 2.8.

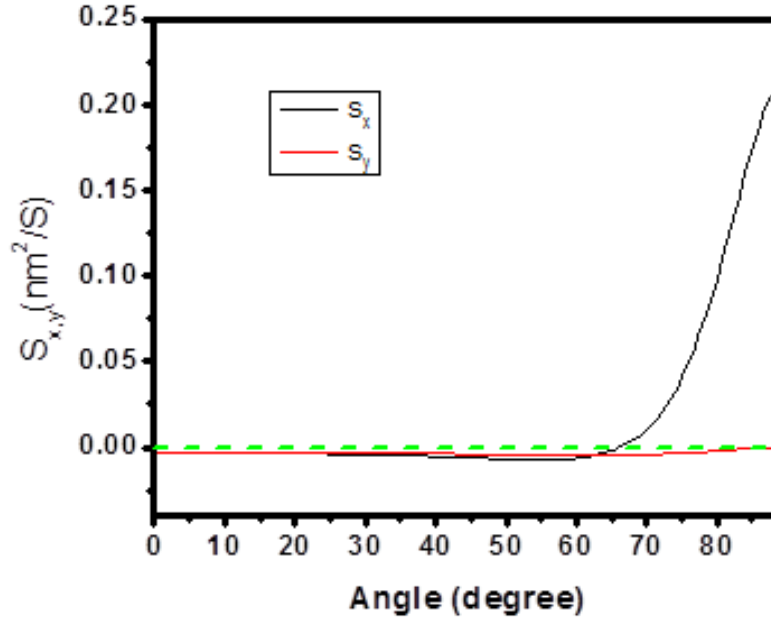


Figure 2.8: Variation of S_x and S_y with ion incidence angle for 10 keV N bombardments on Si.

From the variation of S_x and S_y , it is obvious that both S_x and S_y have the same value at normal incidence, and with increasing angle, the value of S_x and S_y differs. At normal incidence, the pattern is isotropic, but for an oblique incidence, an anisotropic pattern is observed like the ripple pattern. The value of S_x is more negative at 35° - 65° , so the pattern at these angle window will be along the parallel direction of ion beam incidence as observed experimentally [41, 72]. Above the angle 70° , the value of S_x become positive, and S_y is more negative, so one would expect the pattern along perpendicular direction i.e., the pattern is rotated by 90° at grazing ion incidence [73].

To explain the periodic pattern, we need to know the solution of the height equation (2.13), which can be analyzed by Fourier transform. If $h(k_x, k_y, t)$ be the Fourier transform of surface height $h(x, y, t)$, one can write equation (2.13) as

$$\frac{\partial h(k_x, k_y, t)}{\partial t} = [-S_x k_x^2 - S_y k_y^2 - K(k_x^4 + k_y^4)]h(k_x, k_y, t) \quad (2.21)$$

One can get the solution of this equation easily by integrating it,

$$h(k_x, k_y, t) = h(k_x, k_y, 0) \exp[R(k)t] \quad (2.22)$$

where $h(k_x, k_y, 0)$ is the initial amplitude of the Fourier component and $R(k)$ is the growth rate, which control the growth of pattern in a particular direction given by

$$R(k_x, k_y) = -(S_x k_x^2 + S_y k_y^2 + K(k_x^4 + k_y^4)) \quad (2.23)$$

From these equations, the Fourier amplitude will grow exponentially for $R > 0$. Again, the value of K is always positive. So the amplitude will grow depending on the value of the curvature coefficients S_x and S_y . If both values are negative, then R must be positive. R will also be positive if one of them is more negative. The height will grow periodically in that direction which value will be more negative. The value of R will be maximum at $k^* = (\max|S_{x,y}|/2K)^{1/2}$. So the wavelength of the periodic pattern will be

$$\Lambda_{x,y} = 2\pi \sqrt{2K/\max|S_{x,y}|} \quad (2.24)$$

The alignment of ripple wavelength is determined by the larger absolute value of S_x and S_y .

Linear BH theory can successfully explain many experimental observations like ripple pattern formation at oblique incidence, the rotation of ripple pattern at higher angle, and an exponential increase of ripple amplitude at an early time. However, this theory could not explain many observations like

- The ripple coarsening at high fluence.
- Linear increase of ripple wavelength with ion energy.
- Non-zero critical angle for ripple pattern formation.

These deficiencies were overcome after several attempts by adding non-linear terms in the height equation, which will be discussed in the next section.

2.5.2 Non-linear extension of BH theory

(a) Kuramoto-Sivashinsky equation

Cuerno et al. [26, 74] had introduced non-linear terms in linear BH equation to explain the long-time behavior of ripple wavelength, which is called anisotropic Kuramoto-Sivashinsky (KS) equation given as

$$\frac{\partial h}{\partial t} = -\vartheta_0 + \vartheta'_0 \frac{\partial h}{\partial x} + S_x \frac{\partial^2 h}{\partial x^2} + S_y \frac{\partial^2 h}{\partial y^2} + \frac{\lambda_x}{2} \left(\frac{\partial h}{\partial x} \right)^2 + \frac{\lambda_y}{2} \left(\frac{\partial h}{\partial y} \right)^2 - K \nabla^4 h + \eta \quad (2.25)$$

Here, all the terms except fifth and sixth on the right-hand side of equation (2.25) are same as BH equation (2.13). The fifth and sixth terms are due to non-linear effects. The seventh term represents diffusion or viscous flow, and the last term is Gaussian white noise. $\lambda_{x,y}$ are the non-conserved Kardar-Parisi-Zhang (KPZ) nonlinearities [75, 76] and given by

$$\lambda_x = F \frac{c}{2f^4} \left\{ a_\alpha^8 a_\beta^2 s^4 (3 + 2c^2) + 4a_\alpha^6 a_\beta^4 s^2 c^4 - a_\alpha^4 a_\beta^6 c^4 (1 + 2s^2) - f^2 (2a_\alpha^4 s^2 - a_\alpha^2 a_\beta^2 (1 + 2s^2)) - a_\alpha^8 a_\beta^4 s^2 c^2 - f^4 \right\} \quad (2.26)$$

$$\lambda_y = F \frac{c}{2f^2} \{ a_\alpha^4 s^2 + a_\alpha^2 a_\beta^2 c^2 - a_\alpha^4 a_\beta^2 c^2 - f^2 \} \quad (2.27)$$

Park et al. [77] demonstrated that upto a certain time the pattern could be described by the linear theory and after the crossover time the non-linear terms dominate the pattern formation. After the crossover time $t_c \propto \frac{K}{(S_{x,y})^2} \ln \frac{S_{x,y}}{\lambda_{x,y}}$ depending on the sign of the product of non-linear terms λ_x and λ_y , two different scaling regimes are predicted. $\lambda_x \cdot \lambda_y > 0$ indicates an algebraic scaling behaviour similar to the KPZ equation [76], on the other hand, $\lambda_x \cdot \lambda_y < 0$ might correspond isotropic logarithmic scaling [27, 74]. $\lambda_x \cdot \lambda_y < 0$ also predicts the rotation of the ripple by an angle $\theta_c = \tan^{-1} \lambda_{x,y} / \lambda_{y,x}$ [77]. Such rotation of ripple was only observed for high temperature and at very high fluence ($\sim 10^{19}$) [78]. So far, logarithmic scaling behavior has not been observed experimentally, but with increasing angle of ion incidence, one would expect the transition of KPZ scaling to logarithmic scaling [74].

(b) Damped Kuramoto-Sivashinsky Equation

When the KS equation fails to explain some experimental phenomena like the stabilization of ripples or dot after long time bombardment, hexagonal ordering of dot structure, Facsko et al. [79] adopted the isotropic damped KS (dKS) equation for normal incidence ion sputtering. It was also shown that by numerical integration using this equation, dot patterns could exhibit well hexagonal ordering as observed on semiconducting surfaces experimentally [80, 81]. Paniconi

and Elder [82] first used this equation to explain stationary patterns. The dKS equation is nothing but the KS equation (2.25) with an additional damping term $-\chi h$ introduced by Chate et al. [83]. The presence of this additional term decreases the exponential surface height i.e., it can act as a smoothing term and decreases the kinetic roughening.

2.5.3 General continuum equation

The general form of the continuum equation can be obtained from the expansion of equation (2.12). This is given by [27]

$$\begin{aligned} \frac{\partial h}{\partial t} = & -\vartheta_0 + \vartheta'_0 \frac{\partial h}{\partial x} + \sum_{i=x,y} \left\{ -S_i \frac{\partial^2 h}{\partial x^2} + \lambda_i \left(\frac{\partial h}{\partial x} \right)^2 + \Omega_i \frac{\partial^2}{\partial i^2} \frac{\partial}{\partial x} h + \xi_i \frac{\partial h}{\partial x} \frac{\partial^2 h}{\partial i^2} \right\} + \sum_{i,j=x,y} \left\{ -D_{i,j} \frac{\partial^2}{\partial i^2} \frac{\partial^2}{\partial j^2} h \right\} - \\ & K \nabla^4 h + \eta \end{aligned} \quad (2.28)$$

All the terms are discussed in the previous section except Ω and ξ , which are given in the ref. [27] in detail. As the general continuum equation consists of linear and non-linear terms, the effect of these in surface morphology is difficult to predict. However, Makeev et al. [27] predicted the different morphological cases and some features were studied [84], the complete understanding of the non-linear behavior of equation (2.28) is still under investigation.

2.5.4 Role of mass redistribution on ion-induced pattern formation

The ion-induced pattern formation was successfully explained by linear Bradley and Harper theory [5] and its non-linear extensions [25, 27, 76, 77]. However, the BH theory did not support the non-zero critical angle for pattern formation and the flat surface in the angle window

$0^\circ < \theta < 45^\circ$ after ion bombardment. This discrepancy was first overcome by Carter-Vishnyakov (CV) by introducing the collision cascade mass transport and redistribution [8]. This effect was also evidenced by several simulation results and experimental observations [9, 61-63]. Later on, Madi et al. [9] had shown based on CV model that the mass redistribution effect dominates over the BH sputtering effect in the surface instability. Following the CV model, Madi et al. developed the height equation almost same as BH equation [85] given as

$$\frac{\partial h(x,y,t)}{\partial t} = S_x(\theta) \frac{\partial^2 h}{\partial x^2} + S_y(\theta) \frac{\partial^2 h}{\partial y^2} - K \nabla^4 h + \eta(x, t) \quad (2.29)$$

The only difference is in the curvature dependent co-efficient $S_x(\theta)$ and $S_y(\theta)$ which contains the BH erosion term as well as mass redistribution term as

$$S_x(\theta) = S_x^{eros.}(\theta) + S_x^{redis.}(\theta) = \frac{J}{N} a Y_0(\theta) \Gamma_x(\theta) + \frac{J}{N} \delta \cos(2\theta) \cdot f_{corr}(\theta) \quad (2.30)$$

As the y-directional contribution was not considered in the CV model [8], Bobes et al. [66] assumed $S_y(\theta)$ to be only erosion contributed as given in BH theory.

$$S_y(\theta) = \frac{J}{N} a Y_0(\theta) \Gamma_y(\theta) \quad (2.31)$$

Although, Davidovitch et al. [86] included the mass redistributive term by extending the CV model which is given by

$$S_y^{redis.}(\theta) = \frac{J}{N} \delta \cos^2(\theta) \cdot f_{corr}(\theta) \quad (2.32)$$

Here, most terms of equation (2.29-2.32) have been already discussed in the previous section. δ is the average travel distance of recoil atoms which can be calculated from SRIM simulation [50,

68]. $f_{corr}(\theta)$ is the correction factor as given in details in this ref. [66]. $\Gamma_x(\theta)$ and $\Gamma_y(\theta)$ are nothing but the BH curvature dependent terms given by

$$\Gamma_x(\theta) = \left[\frac{A}{B_1} \sin\theta - \frac{B_2}{2B_1} \left(1 + \frac{A^2}{2B_1} \right) \cos\theta - \frac{AC}{B_1^2} \left(3 + \frac{A^2}{B_1} \right) \cos\theta \right] \quad (2.33)$$

$$\Gamma_y(\theta) = \left[\frac{\beta^2}{a^2} \left(\frac{B_2}{2} + \frac{AC}{B_1} \right) \cos\theta \right] \quad (2.34)$$

Many experimental observations have been reported where mass redistribution effect dominated over BH erosion term [9, 50, 66, 68]. The angle-dependent curvature coefficients are shown in Figure (2.9) for 10 keV N ion bombardments on Si surface. Here, the mass redistribution effect is mainly dominating the pattern formation.

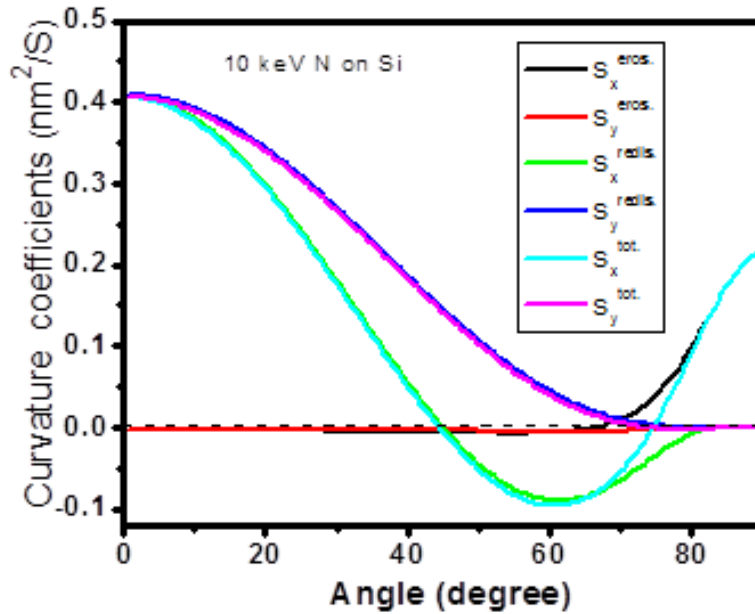


Figure 2.9: Variation of curvature coefficients with incidence angle for 10 keV N bombardments on Si.

2.5.5 Effects of implants and impurities on pattern formation due to other effects like ion implantation, impurity

The effects of ion beam induced erosion and mass redistribution on pattern formation have been discussed in the previous section. However, there are some other effects, which influence the pattern formation. It was shown by Bradley and Hofsass [10] that the effect of implanted ions dominates over erosion and mass redistribution for 5 keV C^+ ion bombardment on amorphous C sample. They gave a theory on it. The idea of this theory is like when non-volatile ions are implanted, it becomes mobile in the surface, and the concentration of the ions increases even after the preferential sputtering. The important effect, which enhances the pattern formation, is the impurity. Ziberi et al. [16, 18, 87] initially detected the pattern formation, induced by unintentional contaminations from different sources. Hofsass and Engler pointed out the effect of contaminations on pattern formation [20, 21]. After that, many researchers experimentally showed the pattern formation by external metal ion incorporation [22, 23, 88, 89]. Bradley gave several theories on the effect of external impurity incorporation on pattern formation [90-93]. However, the effect of beam impurity on pattern formation was not considered by any group. We have recently shown that beam impurity in the mass unanalyzed beam and this impurity induced target chemical change play the major role mainly in low energy ion induced pattern formation [71]. The effect of beam impurity on pattern formation will be discussed in detail in chapter 6.

2.6 Dynamic scaling theory for pattern formation

2.6.1 Dynamic scaling concept

To explain the nano-pattern formation, several continuum models are proposed, but none can describe the experimental observations completely. As an alternative approach, the scaling theory is used to describe the nature of growth of the surface morphology with ion fluence. The idea of scaling theory is that it finds some exponents and from those exponents, the nature of the growth is explained. Depending on the scaling exponents, one can assign the growth system as a particular universality class, which corresponds to a certain continuum model. In recent years, the dynamic scaling behavior of thin film growth by various deposition methods has been widely studied [94-101], but a very few studies on the growth dynamics of nanostructures by ion beam erosion has been investigated [27, 68, 102-104].

The surface evolution during growth or erosion is due to random fluctuations (noises) of heights as well as by local or non-local smoothening/roughening effects on the surface [105]. Statistically, the fluctuation of height having field $h(\vec{l}, t)$ at the position \vec{l} is characterized by the temporal evolution of interface width i.e., rms roughness defined as $W(L, t) = \langle [h(\vec{l}, t) - \langle h(\vec{l}, t) \rangle]^2 \rangle^{1/2}$, where the angular brackets denote averaging over all length scale l within a system size L . According to dynamic scaling theory, surface roughness follows the standard Family–Vicsek (FV) equation [75, 106]; for small length scale ($l \ll \xi$), this increases with system length l following a power law $\sim l^\alpha$, where α is the roughness exponent, but at larger length scale ($l \gg \xi$), W shows saturation and becomes independent of system length l . In the later regime ($l \gg \xi$), W scales with time as t^β , where β is known as the growth exponent. So generally, the scaling behavior of $W(l, t)$ can be written as

$$W(l, t) \propto \begin{cases} l^\alpha & \text{if } l \ll t^{\beta/\alpha} \\ t^\beta & \text{if } l \gg t^{\beta/\alpha} \end{cases} \quad (2.35)$$

Here, ξ signifies the lateral correlation length i.e., the system length up to which the heights are correlated, which again scales with time as $t^{1/z}$, where $1/z = \beta/\alpha$ is called the dynamic exponent. It can be calculated from the width of autocorrelation function $C(l) = \langle h(l)h(0) \rangle$ at which $C(\xi) = C(0)/e$, e is the base of natural logarithm [107].

The important parameter, which is used to investigate the growth process of the surface structure by ion erosion or deposition process, is the height-height correlation function. This is defined as “the mean square of the height difference between two positions separated by a lateral distance l ”, can be expressed as

$$G(l, t) = \langle [h(\vec{l}, t) - h(\vec{0}, t)]^2 \rangle \quad (2.36)$$

The scaling properties of $G(l, t)$ for isotropic surface can be written as

$$G(l, t) \propto \begin{cases} l^{2\alpha} & \text{if } l \ll \xi(t) \\ 2W^2(t) & \text{if } l \gg \xi(t) \end{cases} \quad (2.37)$$

The height-height correlation function increases initially with r and then saturates at ξ . So, at $r \gg \xi$, the asymptotic value of $\sqrt{G(r)/2}$ gives the value of rms roughness W .

Alternatively, another important parameter power spectral density (PSD) or structure factor, which is obtained after the Fourier transform of surface height, is defined in momentum space to study the scaling behavior as

$$PSD(k, t) = S(k, t) = \langle \tilde{h}(k, t) \tilde{h}(-k, t) \rangle \quad (2.38)$$

where $\tilde{h}(k, t)$ denotes the Fourier transform of the surface height $h(l, t)$ and k denotes the spatial frequency. The structure factor also follows Family-Vicsek relation as

$$S(k, t) = k^{-(2\alpha+d)} s(kt^{1/z}) \quad (2.39)$$

with the scaling function,
$$s(u) \propto \begin{cases} \text{const.} & \text{if } u \gg 1, \\ u^{(2\alpha+d)} & \text{if } u \ll 1. \end{cases} \quad (2.40)$$

Here, d is the dimensionality of the surface, i.e. for two-dimensional system $d = 2$ and for one-dimensional system $d = 1$. From the scaling law, one can find the values of scaling exponents α , β , and z from the surface morphological images, and from these values, we can estimate the nature of the growth as well as control the growth.

2.6.2 Scaling theory for anisotropic surfaces

The scaling behavior of anisotropic surfaces is more complex than the isotropic surfaces. The dynamic scaling exponents along different direction say x , y are not same for a growth system. So, the roughness exponents $\alpha_{x,y}$ can be extracted from the height-height correlation function without considering any time dependence. Then the rescaling function along x -direction can be written as [108]

$$G(x, y) \propto b^{\alpha_x} G(b^{-1}x, b^{-\chi_x} y) \quad (2.41)$$

Here, $\chi_x = \frac{\alpha_x}{\alpha_y}$ is the anisotropy exponent indicating the degree of anisotropy in two directions.

Similarly, the rescaling function of height-height correlation function along y -direction is

$$G(x, y) \propto b^{\alpha_y} G(b^{-1\chi_y} x, b^{-1} y) \quad (2.42)$$

with $\chi_y = \frac{1}{\chi_x} = \frac{\alpha_y}{\alpha_x}$. Similarly, the scaling behavior can be applied for the structure factor of one dimensional cut along x and y direction in momentum space. These can be written as [109]

$$S(k_x) \propto k_x^{-(2\tilde{\alpha}_x+2-\chi_x)} \quad (2.43)$$

$$S(k_y) \propto k_y^{-(2\tilde{\alpha}_y+2-\chi_y)} \quad (2.44)$$

where $\tilde{\alpha}_{x,y}$ is two roughness exponents in momentum space can be correlated with the roughness exponents in real space as

$$\tilde{\alpha}_x = \alpha_x - \frac{1-\chi_x}{2} = \alpha_x - \frac{1-\alpha_x/\alpha_y}{2} \quad (2.45)$$

$$\tilde{\alpha}_y = \alpha_y - \frac{1-\chi_y}{2} = \alpha_y - \frac{1-\alpha_y/\alpha_x}{2} \quad (2.46)$$

For isotropic scaling, $\chi_x = \chi_y = 1$, i.e., $\alpha_x = \alpha_y$, $\tilde{\alpha}_x = \alpha_x$ and $\tilde{\alpha}_y = \alpha_y$. Substituting (2.45) and (2.46) into (2.43) and (2.44) we get

$$S(k_x) \propto k_x^{-(2\alpha_x+1)} \quad (2.47)$$

$$S(k_y) \propto k_y^{-(2\alpha_y+1)} \quad (2.48)$$

Thus for $k_{x,y}t^{1/z} \gg 1$, the real space exponents can be calculated from momentum space by one dimensional structure factor. Another exponent, called dynamic exponent, calculated from correlation length, also shows anisotropy along two different directions. The scaling relation along two directions is $\xi_x \propto t^{1/z_x}$ and $\xi_y \propto t^{1/z_y}$. It was shown that for strongly anisotropic scaling, one has to follow the relation $\beta = \frac{\alpha_x}{z_x} = \frac{\alpha_y}{z_y}$ [110].

Chapter 3

Experimental procedures and characterization techniques

The Si(100) and muscovite mica samples were bombarded by keV energy ion beam. The different types of ion beams were extracted from an ECR (Electron Cyclotron Resonance) ion source in the Radioactive Ion Beam Laboratory (RIB Lab) at Variable Energy Cyclotron Centre (VECC), Kolkata, India. The whole experimental system was maintained at high vacuum (better than 10^{-7} mbar). The samples before and after irradiation were characterized by several techniques like Atomic Force Microscopy (AFM) for surface morphology, Transmission Electron Microscopy (TEM) for cross-sectional information of the sample, X-ray Photoelectron Spectroscopy (XPS) for surface chemical composition, X-ray Diffraction (XRD) for structural information, and UV-visible spectrophotometer for optical measurement. This chapter describes the sample preparation methods and characterization techniques.

3.1 Low energy ion beam system for surface and interface modification

The low energy ion beam irradiation method was used to prepare the samples. The schematic of the low energy ion beam experimental set up and photography of experimental set up in the lab are shown in Figure 3.1 and 3.2, respectively. The system consists of (i) an ECR ion source, (ii) accelerating system, (iii) analyzing dipole magnet, and (iv) the target chamber.

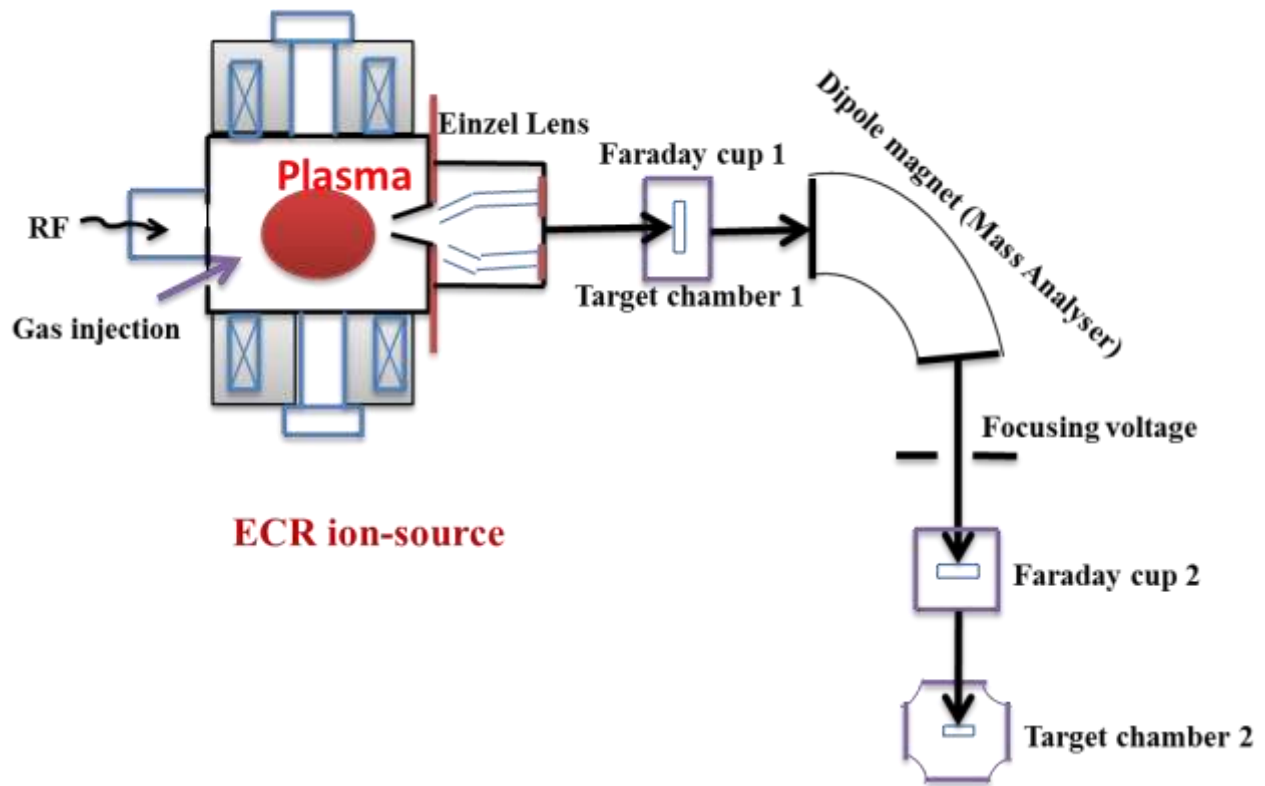


Figure 3.1: Schematic of ECR ion source and low energy ion separator



Figure 3.2: Photography of low energy ion beam experiment set up in VECC Kolkata

(i) ECR ion source

The Electron Cyclotron Resonance (ECR) consists of (a) a plasma chamber under vacuum, (b) solenoid coils and hexapole permanent magnet, (c) microwave source, and (d) gas feeding system. The schematic diagram of 2.4 GHz ECR ion source at VECC Kolkata is shown in Figure 3.3.

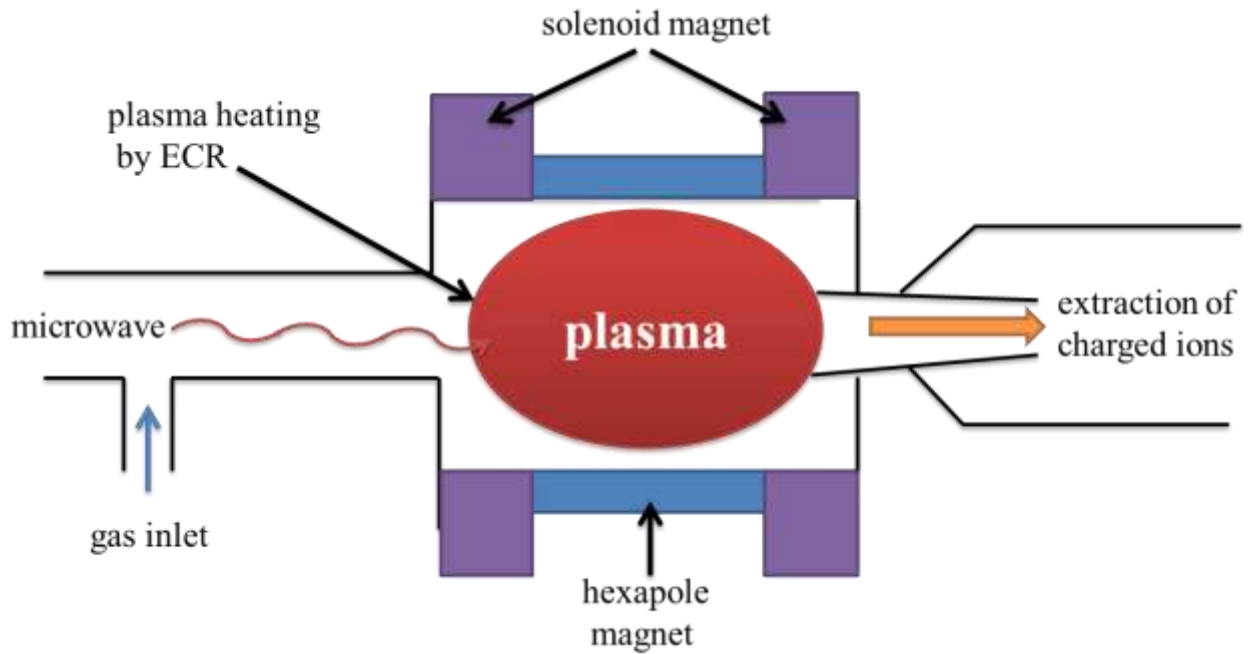


Figure 3.3: Schematic diagram of the ECR ion source.

The solenoid coils provide the axial magnetic field, whereas the hexapole magnets create the permanent radial magnetic field of 1 Tesla. The gas is injected into the ECR plasma chamber to generate the plasma. When the microwave is injected to the plasma chamber, the plasma is generated. The electrons move in a circular orbit around the magnetic field due to the Lorentz force. The frequency of gyration of the electron is $\omega_{ECR} = \frac{eB}{m}$, e is the electronic charge, B is the

magnetic field, and m is the mass of the electron. When the frequency of microwave matches with the electron gyration frequency, the resonance occurs. This resonance condition is called electron cyclotron resonance (ECR) as given below

$$\omega_{RF} = \omega_{ECR} = \frac{eB}{m} \quad (3.1)$$

Due to the resonance, the electrons get heated, and when their energies reach above the ionization potential, they eject the orbital electrons creating the ionized atoms. As a result, the huge amounts of ions with single, double, triple, and so on charge states are created in the plasma chamber. Generally, the density of ions in a plasma chamber can be of the order of 10^{12} particles/cm³ with electron temperature upto few keV [1]. The inner diameter of typical plasma chamber is chosen as $\geq 2\lambda$, where λ is the wavelength of the microwave. The microwave power is generated by a klystron amplifier (2kW), which is transmitted into the ECR ion source by transmission wave guides. The plasma chamber as well as the ECR body is cooled with low conductivity water (LCW) due to the microwave heating.

(ii) Accelerating system

The ions, produced inside the plasma chamber, are extracted at energies ranging from 2 keV to 30 keV. The plasma chamber is kept at a floating high voltage, whereas the extraction electrode is grounded. A plasma electrode is also placed in the beam extraction end of the ECR plasma chamber. There is a potential difference between the plasma electrode and ground extraction electrode. Due to this potential difference, the ion beam is accelerated. An Einzel lens is placed after the extraction electrode for focusing and transporting the beam towards the analyzing bending magnet.

(iii) Analyzing dipole magnet

The analyzing dipole magnet is a very important part as it gives pure mass analyzed beam after filtration. The analyzed beam is extracted by the selection of A/q ratio, where A is the mass number of ion, and q is the charge state of the ion. This analyzing magnet can also be used as isotope separation. The mass spectrum of ions on the target chamber is shown in Figure 3.4.

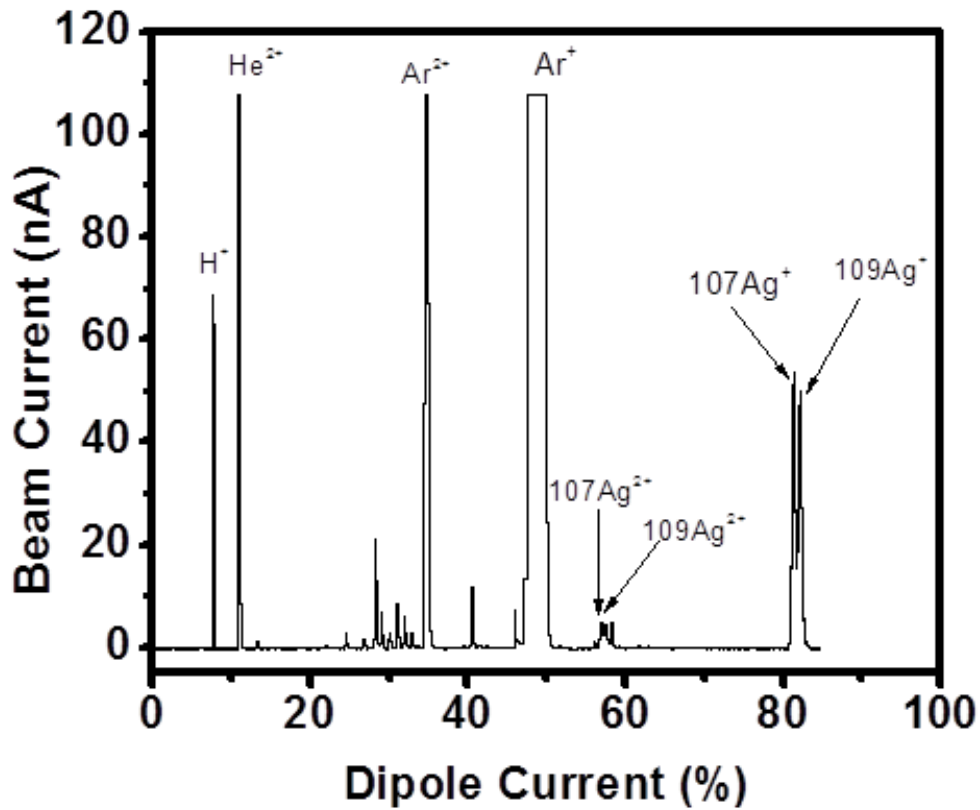


Figure 3.4: Mass spectrum of ions on target chamber by 6 keV extraction voltage from ECR ion source showing different ions extracted from ECR ion source.

The mass spectrum was taken in the region of the magnetic field where Ag beam was extracted and shown in Figure 3.5. This shows the well separation of ^{107}Ag and ^{109}Ag isotope.

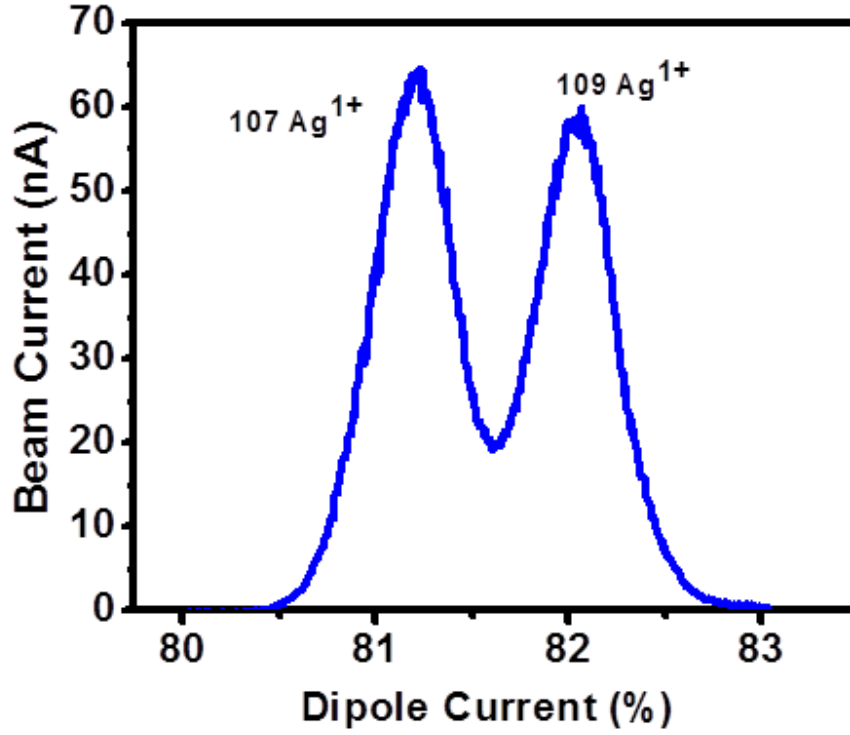


Figure 3.5: Mass spectrum of ions on target chamber 6 keV extraction voltage from ECR to show Ag isotope separation.

(iv) Target chamber

The target chamber is connected with the beam line, and it is placed just after the Faraday cup 2 as shown in Figure 3.1. The target is maintained at a high vacuum with pressure $\sim 10^{-8}$ mbar. Four samples can be mounted at a time, and by adjusting the feedthrough, all the samples are irradiated without breaking the vacuum. The samples are placed on a small aluminum block of different angles. Each sample is surrounded by a cylindrical cup, which is given a negative bias to suppress the secondary electrons. A front plate covers all the cylinders, and 8 mm hole in the front plate is kept to pass the beam into the sample. The schematic of this arrangement is shown in Figure 3.6.

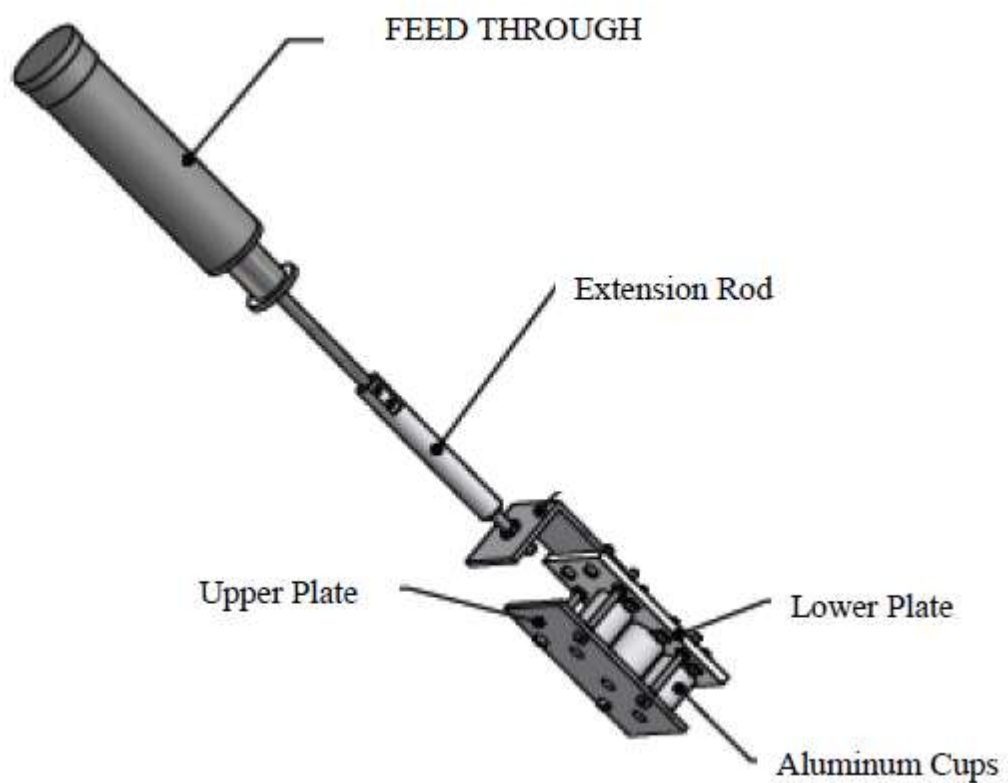


Figure 3.6: Sample holder for ion beam irradiation experiment.

The target, cylinders, and front plate are electrically isolated. The target current is measured by a current integrator from Danfysik (model A554).

3.2 Characterization techniques

In this thesis, the Atomic Force Microscopy (AFM) technique was used mostly for the surface morphology. Also, the X-ray Photoelectron Spectroscopy (XPS), Transmission Electron Microscopy (TEM), X-ray Diffraction (XRD), and UV-Visible Spectrophotometer were used for characterization purpose. The detailed techniques are discussed in this chapter.

3.2.1 Atomic Force Microscopy (AFM)

The Atomic Force Microscopy (AFM) is basically a family of scanning probe microscopy (SPM) techniques, which came after the invention of scanning tunneling microscope (STM) in early 1980. In this method, a sharp probe (tip) is used to scan over the sample for taking the morphology. The tip is used as a cantilever, which is basically of silicon or silicon nitride having a radius of curvature \sim nm. When the tip is taken close to the surface, the forces between tip and surface follow the Hooke's law $F = -kx$, which leads to the deflection of the cantilever. Here, F is the force, k is the force constant, and x is the cantilever deflection. The range of force constant lies usually from 0.01 to 1.0 N/m, which leads to the force in the range from nN to μ N. The force distance curve is shown in Figure 3.7, which explains the several types of interaction with the cantilever and sample surface. When the tip is kept a far distance from the sample, no adhesion force acts between them, but when the tip is close to the sample, there acts attractive force as shown in the right of the curve. At a certain distance, the tip touches the sample when the adhesion force is much larger than the force due to cantilever. In this region, the repulsive force generally balances the cantilever to its position.

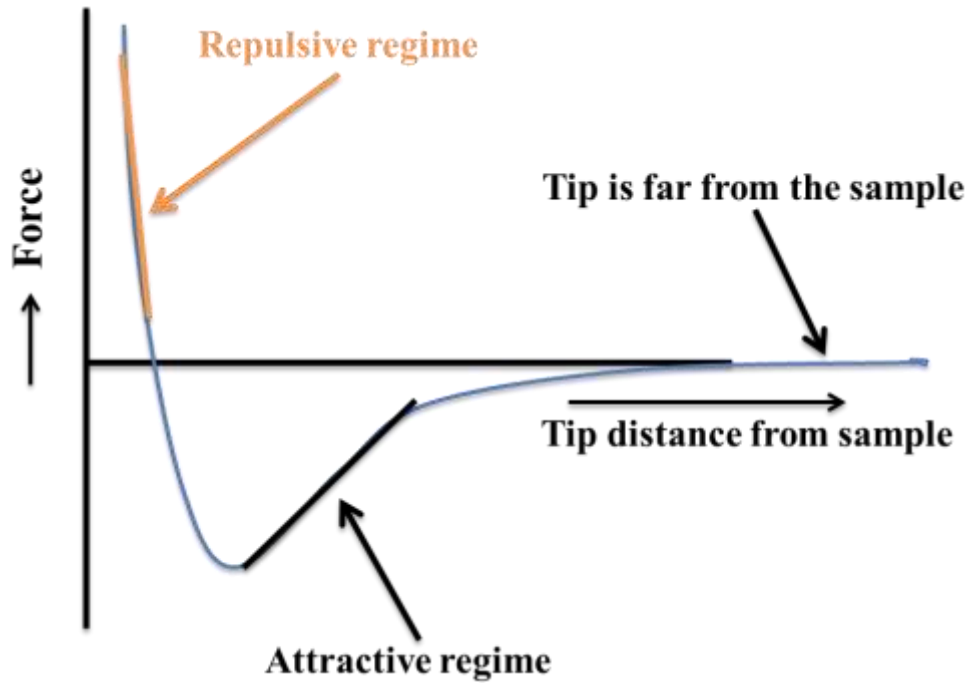


Figure 3.7: Force distance curve of AFM operation.

The AFM consists of a cantilever, mirror, position sensitive photodetector, piezoelectric scanner, and computer. The schematic diagram of it is shown in Figure 3.8. When the tip scans over the sample surface, it takes the fluctuation of height profile by position sensitive photodetector and feedback loop. The piezoelectric scanner converts the mechanical change to the electrical signal and shows the surface topography as well as height profile on the computer screen. The AFM is mainly operated in three modes, the first one is contact AFM in which the tip-surface separation is less than 0.5 nm, the second is tapping mode in which the tip-surface separation is 0.5-2 nm, and the third one is non-contact mode in which the separation is 0.1-10 nm.

Atomic Force Microscopy (AFM) : General Components and Their Functions

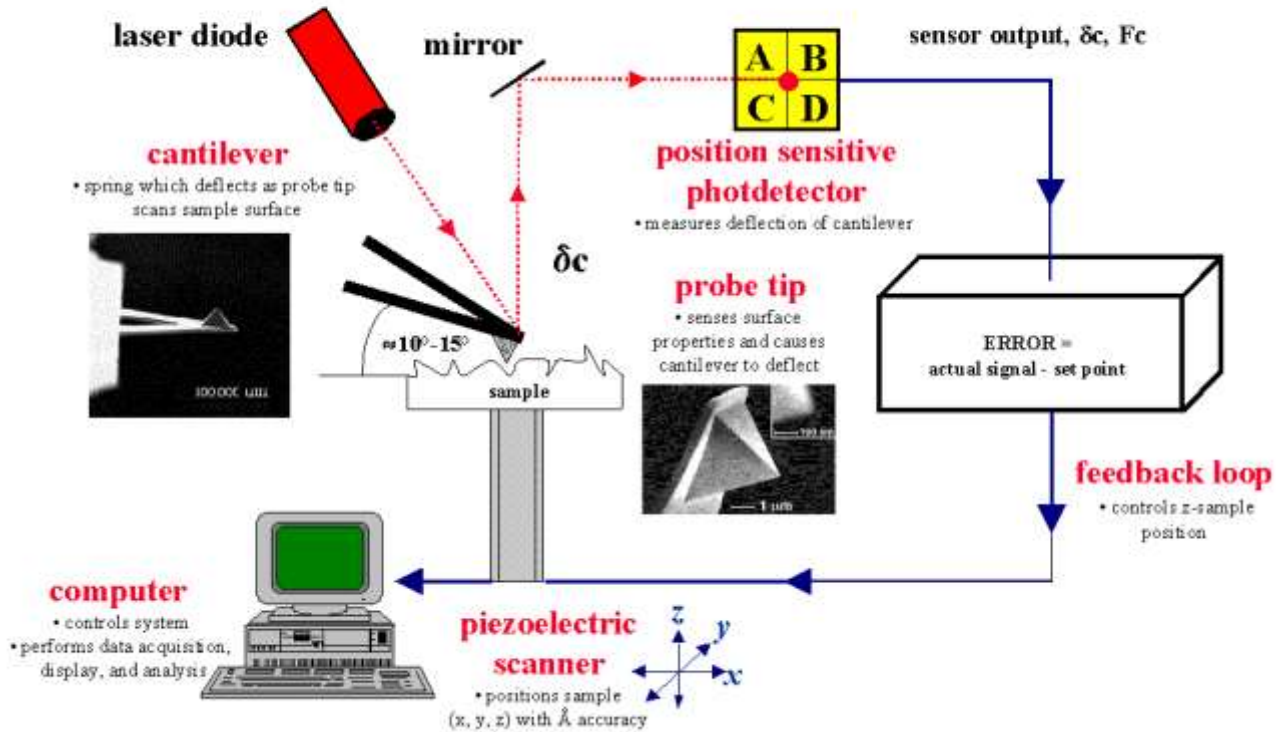


Figure 3.8: Schematic diagram of the working principle of AFM.

Contact mode AFM

In this mode, the tip makes soft contact with the sample surface. When the tip surface separation is of the order of few angstroms, it experiences repulsive van der Waals force. In contact mode, the tip scans the surface by keeping a constant distance from the surface (using the feedback loop) by vertically moving the scanner at each (x,y) data point to maintain a “setpoint” deflection, and the variations in tip-sample interaction force reveal the atomic scale topography

of the surface. This mode is suitable for rough solid samples. The main disadvantage of this mode is that it may damage soft samples as the tip remains in very close proximity to the sample surface.

Tapping mode AFM

This mode was developed to get high-resolution topography without inducing any frictional forces between tip and surface. In this mode, the tip oscillates up and down the surface at or near its resonance frequency. When the tip approaches close to the surface, several forces like “van der Waals forces”, dipole-dipole interactions, electrostatic forces, etc., act on the cantilever, which leads to decrease in the amplitude of the oscillation. A feedback loop maintains the constant separation between tip and sample. As a result, the image is obtained by scanning the surface. This method allows to get high resolution and damage free imaging of soft and delicate biological samples. However, this mode encounters difficulties for liquid samples.

Non-contact mode AFM

This mode is basically used to image the fluid sample. In this mode, the tip operates in the non-repulsive region of the force vs. distance curve [Fig. 3.7]. During the scanning, the tip is not in contact with the sample, but it oscillates above the adsorbed fluid layer on the surface at a frequency larger than its resonance frequency. Hence, the sensitivity is increased compared to the tapping mode AFM, but the resolution of images seems to be poorer. This significant drawback can be removed in ultra-high vacuum (UHV), where Non-contact mode AFM gives the best imaging of the sample surface.

Details of AFM in the present experiments

In the present experiment, the nanoscope Multi-Mode V has been used which consists of major components microscope, xyz scanner, controller, and computer as shown in Figure 3.8. The position sensitive detector provides different information with combining four elements of the quad photodiode, and these four elements combine to form the SUM signal. The scanner crystals X-Y axes produce a raster type scan in which the horizontal axis is referred to as fast axis scan, and the vertical axis is referred to as slow axis scan. A Nanoscope V controller controls the whole experimental system.

3.2.2 X-ray Photoelectron Spectroscopy (XPS)

X-ray photoelectron spectroscopy (XPS) is a very powerful tool to characterize the surface chemical composition. The mechanism of XPS is mainly based on the photoelectric effect. This technique is widely used to investigate the elemental composition, the empirical formula of a material, contamination on the surface, and chemical states of elements. It can give the information from the top surface to 10 nm depth surface. The XPS spectra are obtained after irradiating the sample surface by energetic X-ray beam and hitting the core electrons, which results in the ejection of that electron. The kinetic energy of that electron is measured by electron energy analyzer to get the binding energy (B.E.) of the photoelectron as

$$B.E. = h\nu - K.E. - W \quad (3.2)$$

where h is the Planck constant, ν is the frequency of the photoelectron, K.E. is the kinetic energy of the photoelectron, and W is the work function. The schematic diagram of XPS is shown in Figure 3.9.

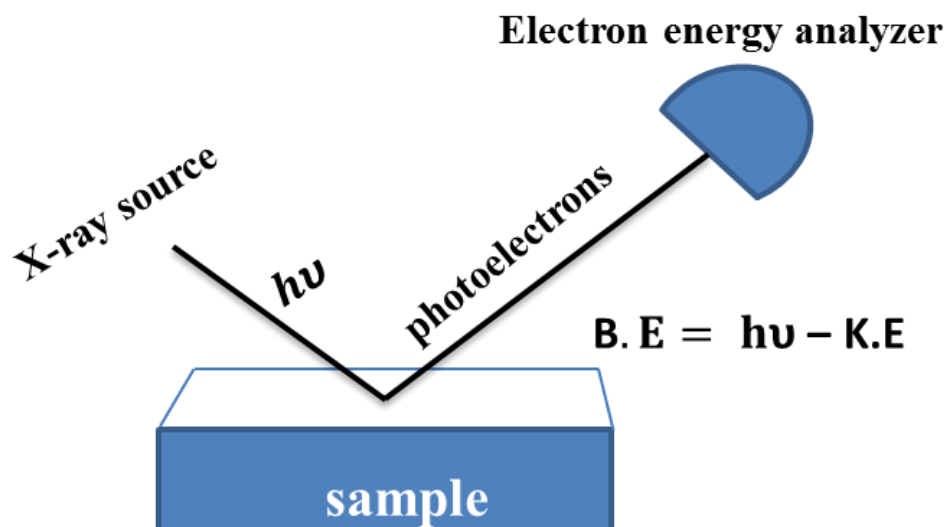


Figure 3.9: Schematic diagram of the working principle of XPS.

The different parameters like elements in the sample, the chemical change of the sample are determined from the peak intensities and peak positions of different elements in the XPS spectra. The stoichiometry of chemical compound is also predicted from the peak fitting of high-resolution XPS spectra. The % of atomic concentration can be calculated by determining the area of each peak and considering the sensitivity factor. In the present experiment, an Omicron Multi-probe (Omicron Nano Technology, UK) was used for XPS. A monochromatic Al K_{α} source of X-ray was used to provide photon energy, and the hemispherical analyzer was used to calculate the kinetic energy of the photoelectrons. The whole system was maintained in high vacuum ($\sim 10^{-10}$ mbar).

3.2.3 Transmission Electron Microscopy (TEM)

Transmission electron microscopy (TEM) is a very important technique to get the atomic level images of a specimen. The image is formed by passing an electron beam perpendicularly through ultrathin sample. The basic principle is same as that of light microscope, but the resolution of

TEM is thousands times better than light microscope as the wavelength of electron (0.05 \AA) is much lower than usual visible light ($0.5 \text{ }\mu\text{m}$). So, this can give the image in atomic resolution. When the electrons are transmitted into the specimen, it interacts with the surface and the magnified and focused images are formed on a fluorescent screen or on a CCD camera. The schematic diagram of TEM is shown in Figure 3.10. The major parts of TEM are electron source or gun, electromagnetic lens system, sample holder, and imaging system. The source of electrons consists of a cathode and anode, which can produce upto 200-300 keV energy. The electrons are focused in a parallel beam by a condenser lens. The condenser lens is mainly a pair of electromagnetic lens. The first condenser lens fixes the spot size, and the second lens changes the size of the spot on the sample. A condenser aperture is also attached beneath the second condenser lens which is a thin disk of metal with small circular aperture. The beam from the aperture strikes the sample which lies in the plane of objective lens. The objective lens focuses the transmitted electrons from the sample into an image. Finally, the electron beams fall on phosphor screen or charge coupled device (CCD) camera, which can be magnified on the viewing screen by the first and second intermediate lens and the projector lens assembly.

The main important task for getting good images of a sample is the preparation of the sample. For this, the specimen is made so thin that major portion of electron beam can pass through the sample. The penetration power of electron beam depends on the energy of the incident electron and elemental composition of the sample. Generally, the sample is thinned below 100 nm for TEM and below 50 nm for high-resolution TEM.

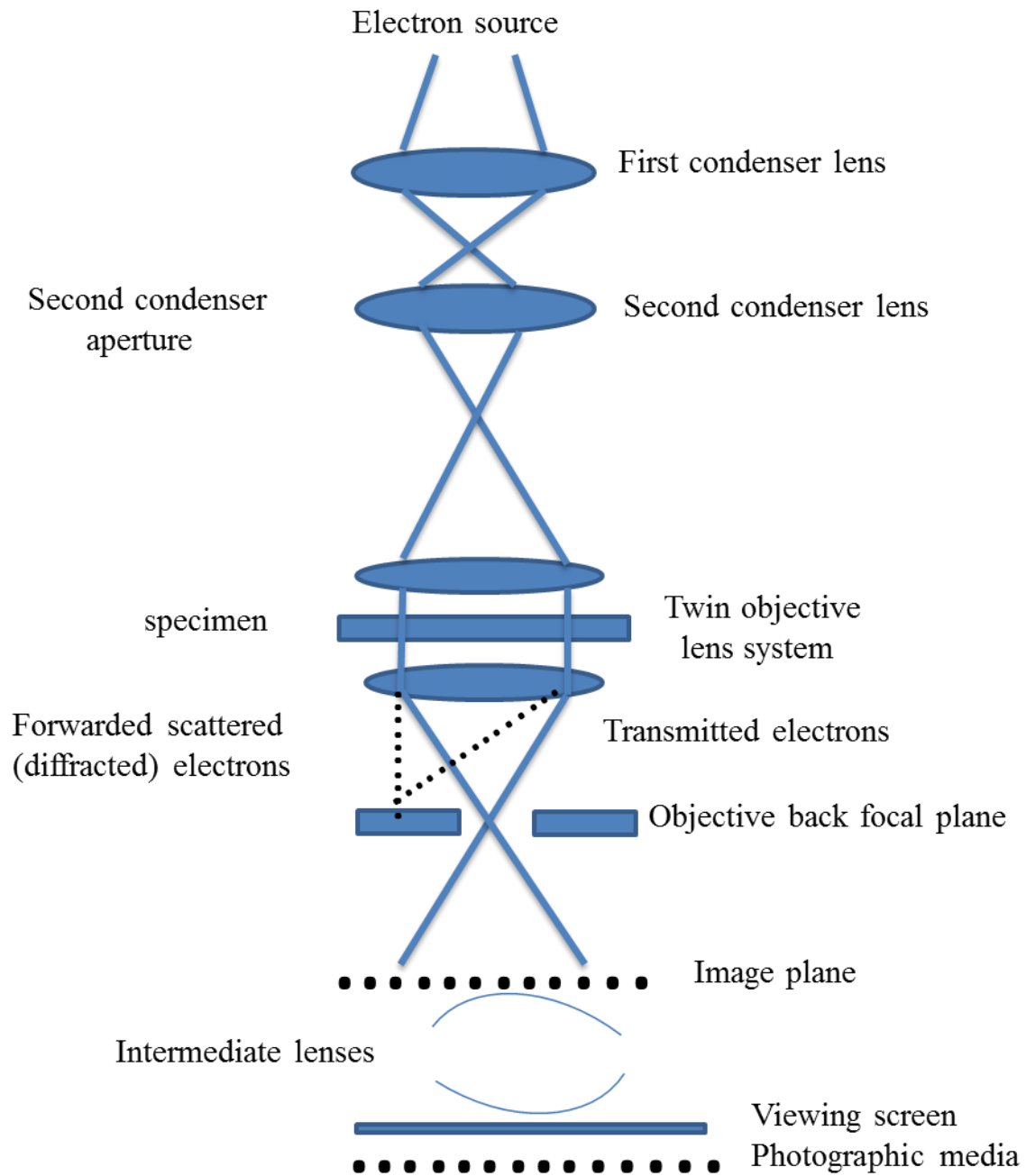


Figure 3.10: Schematic diagram of TEM

The electrons during passing through the sample can produce backscattered or elastically scattered electrons, inelastically scattered electrons, X-rays, Auger electrons or light etc. Also, the electrons transmitted through the sample can be divided into two categories, one is scattered

i.e., diffracted, and another is unscattered i.e., transmitted beam. The transmitted electrons do not interact with the surface and are proportional to the thickness of the sample. On the other hand, the elastically scattered electrons are diffracted by atoms and produce the diffraction patterns, which follow the Bragg's law. These patterns can give atomic spacing between two crystal planes.

In this thesis work, TEM, HRTEM including Electron Energy Loss Spectroscopy (EELS) and Energy Dispersive X-ray spectroscopy (EDX) investigations are performed using a FEI, Tecnai G2F30, S-Twin microscope operating at 300 kV with Gatan Imaging Filter (model 963) and EDAX detector (EDAX Inc.), respectively. The Cross-sectional TEM (XTEM) specimens are prepared using the standard method of mechanical grinding and dimpling with final thinning using a precision-ion- polishing system (PIPS, Gatan, and Pleasanton, CA).

3.2.4 X-ray Diffraction (XRD)

When the wavelength of an X-ray is of the order of the inter-atomic distance in the crystal, the x-rays are diffracted, called X-ray diffraction. This is due to a certain phase relation between two or more waves. If a wave is incident on crystal planes with separation d , the path difference between the waves, scattered from two consecutive planes, will be $2d\sin\theta$, θ being the incident angle. The scattered rays are completely in phase with each other if their path difference is an integral number n of wavelengths i.e., $2d\sin\theta = n\lambda$, λ is the wavelength of x-ray. When the angle of incidence with the surface is $\sim 0.5^\circ$, the near surface information can be acquired, which is called Grazing Incidence X-ray Diffraction (GIXRD). It is very useful for ion beam implanted samples. In the present case, a Bruker D 8 Advance X-ray diffractometer using Cu K_α radiation has been used to characterize the phase of the buried implanted layer.

3.2.5 Ultraviolet-Visible Spectroscopy

Ultraviolet-visible spectroscopy is the absorption or reflection spectroscopy in the ultraviolet-visible range. When the light in the UV/Visible range (210 – 900 nm) is incident on any sample, the electronic transitions between two energy levels takes place for electromagnetic radiation in the spectrum. The molecules in the sample basically absorb ultraviolet radiation, and the electrons in the molecule undergo a transition from lower to higher energy level. However, the whole energy is not absorbed by the molecule, some part is absorbed and other is utilized for the transition from lower to higher energy level. A spectrometer is used to record the percentage of absorption by a sample at a different wavelength, and the plot of absorbance vs. wavelength gives the absorption spectrum. UV/Vis spectroscopy is generally used in chemistry, biological macromolecules. This is commonly carried out in solutions, but the works in solids are also studied. In this thesis, the spectrum was taken in reflectance mode by PerkinElmer Lambda 750 UV/VIS spectrometer in the wavelength range 190–800 nm.

Chapter 4

Surface and near surface modification of Si by ion beam irradiation for photovoltaic and de-wetting applications

This chapter first describes the synthesis of nano-pattern and buried plasmon active layer formation on Si surface for photovoltaic application. Then, the growth of nano ripple pattern formation by N^+ ion bombardment at different energies on Si surfaces is discussed. Also, the optical study of N implanted Si surfaces and tuning hydrophobicity with the ion beam parameters for N bombarded Si surfaces are deliberated here.

Related publications

1. **D. Bhowmik**, S. Bhattacharjee, D. Lavanyakumar, V. Naik, B. Satpati, and P. Karmakar, “Synthesis of nano-patterned and Nickel Silicide embedded amorphous Si thin layer by ion implantation for higher efficiency solar devices”, **Applied Surface Science** **422**, 11 (2017).
2. **D. Bhowmik**, P. Karmakar, “Energy dependent ripple growth on Si (100) by N^+ ion beam irradiation Energy dependent ripple growth on Si (100) by N^+ ion beam irradiation”, **AIP Conference Proceedings** **1832**, 080019 (2017).
3. **Dipak Bhowmik**, and Prasanta Karmakar, “Enhancement of optical absorption of Si (100) surfaces by low energy N^+ ion beam irradiation” **AIP Conference Proceedings** **1953**, 100071 (2018).

4.1 Synthesis of nano-patterned and plasmon active buried thin layer by ion implantation for higher efficiency solar devices

4.1.1 Introduction

Surface patterning, as well as metallic nanostructures incorporation in a semiconducting material, has attracted much attention because of its potential application in plasmonics, solar energy harvesting, storage devices, and nanoelectronics [111]. The presence of plasmon active metal nanostructures in amorphous Si enhances the photocatalytic and photovoltaic properties of semiconductor [112, 113]. The surface texturing or patterning on a semiconductor is also another way of increasing light absorption efficiency. The pattern on the surface increases the surface absorption area and simultaneously reduces the reflection of light, hence increases light trapping ability [114, 115].

For solar energy harvesting, c-Si or a-Si is not good absorber of light in the visible solar spectrum [113]. However, it is still the best selection for solar devices because it is abundant, non-toxic, cheap, and its processing technology is well known. Specifically, thin film a-Si solar cell technology is more attractive to make very cheap and flexible solar harvesting device. Therefore, an innovative cost effective and minimum step processing approach is essential to increase the efficiency of a-Si based photovoltaic devices. Previous initiatives involve increasing the surface area [115] and incorporation of plasmon active particle [113]. For wafer based Si cells, 2-10 micron depth trenches are drawn for more light trapping [113], but for thin film solar cells, this much trench is not possible, whereas nano-metre scale regular texturing by lithographic technique on a large area is not cost effective. The surface texturing done by chemical etching [114] generates random rough surface and also incorporates undesirable

chemical contamination. Plasmon active metal ion implantation promised potential improvement of photovoltaic [116] and photocatalytic [117] behavior. Metal incorporation by simple deposition is a common practice, however multi-step processing, as well as high-temperature annealing, is required [118] in this process. Therefore, surface texturing and metal incorporation by such multi-step process can be expensive and complicated. The KeV energy broad ion bombardment is a powerful technique to pattern a large surface area as well as implants metal atoms at a specific depth with a controlled concentration [41, 119] .

Here, we will discuss an ion beam based approach where the nanopatterning and plasmon active metal incorporation have been performed simultaneously by a single step low energy ion implantation on Si. We have observed rim type surface pattern and buried nickel silicide layer formation by 10 keV Ni⁺ ions implantation on Si (100) surface at normal incidence. Amorphization of the c-Si substrate is advantageous for the present study where this system becomes equivalent to thin film a-Si based solar cells. Crater surrounded by rim type regular surface pattern formation due to Ni⁺ ion impact is explained as well as the system is cross-sectionally probed by TEM and verified with SRIM calculation. The enhancement of light absorption by patterned and nickel silicide embedded Si is presented here.

4.1.2 Experimental

The commercially available polished Si (100) samples were cleaned and degreased with trichloroethylene in an ultrasonic bath and then washed with methanol and distilled water. The samples were bombarded with 10 keV Ni⁺ at the normal incident with a fluence of 1×10^{17} ions/cm². The angle of ion incidence has been considered as the angle of ion beam with the surface normal throughout the thesis. The ion beam was extracted from the 2.4 GHz ECR ion

source of the Radioactive Ion Beam Facility at Variable Energy Cyclotron Centre Kolkata. During the experiment, the target chamber pressure was 3×10^{-7} mbar. The surface morphologies of the Si(100) samples before and after the implantation were examined in air using Bruker Atomic Force Microscopy (AFM), Multi-Mode V at VECC, Kolkata.

Cross-sectional TEM (XTEM) specimen was prepared using the standard method of mechanical grinding and dimpling with final thinning using a precision-ion- polishing system (PIPS, Gatan, and Pleasanton, CA). The ion polishing was carried out at 3.0 keV followed by 1.2 keV cleaning process at SINP, Kolkata. TEM including Electron Energy Loss Spectroscopy (EELS) and Energy Dispersive X-ray spectroscopy (EDX) investigations were performed using a FEI, Tecnai G² F30, S-Twin microscope operating at 300 kV with Gatan Imaging Filter (model 963) and EDAX detector (EDAX Inc.), respectively, attachments also at SINP, Kolkata.

Grazing incidence X-ray diffraction (GIXRD) profiles from Ni implanted Si samples have been recorded at grazing incident angle of 0.5° by a Bruker D 8 Advance X-ray diffractometer using Cu K α radiation. Optical measurements are performed by a Perkin Elmer Lambda 750 UV/VIS spectrometer in the wavelength range 190-800 nm.

4.1.3 Results and discussions

Figure 4.1 shows the AFM images of bare and Nickel ion bombarded Si surfaces. The AFM image of bare Si (100) is shown in Figure 4.1 (a). The measured rms roughness of the bare sample is 0.11 nm. Figure 4.1(b) shows the topography after 10 keV Ni⁺ ion bombardment at fluence of 1×10^{17} ions/cm². Craters surrounded by rims are observed on the surface, and the surface roughness increases to 0.78 nm. The line profiles of the structures are also shown, and

the average crater diameter varies from 105 nm to 115 nm. The nuclear stopping power of 10 keV Ni on Si (100) surface, calculated from SRIM, is 82 eV/ Å⁰.

High density energy deposition of Ni ions changes the initially flat Si surface by removing a volume of material at the impact point and also rearranges the target atoms around the depression. With continuous bombardment, the combined effects of individual ion impact develop the rim pattern on the surface. Kalyanasundaram et al. [62] demonstrated the effect of 500 eV Ar⁺ ion bombardment on Si at normal incidence and determined the change of local surface height by molecular dynamic simulation. Bradley and Harper predicted that the low energy ion induced erosion leads to linear instability for all ion incident angle followed by a structure formation on the surface [5]. Khang et al. [120] included the nonlinear terms and explained the hole or mound formation on the surface due to ion bombardment at normal incidence. Nevertheless, if only sputtering removal is considered, the decrease of height (hole) formation is expected, but the observed rim formation could not be explained. Davidovitch et al. [86] demonstrated that surface height change is not due to purely erosive, but mass redistribution is very much important. The effect of sputtering and mass redistribution leads to create reduced and increased height, or crater and rim, respectively [62]. However, the crater function model without the consideration of local curvature could not explain the structure formation properly at normal incidence [121]. Recently, Harrison and Bradley [122] have showed that the incorporation of curvature in crater function model is essential to describe the instability of the surface and hence pattern formation. The observed rim structure formation can be explained properly by curvature dependent crater function theory [122]. The impact of individual ion generates the craters on the flat surface and modifies the local height profile. For long time ion bombardment, the changes of local surface height for individual ion impact are superimposed,

and a final pattern is formed on the surface. The crater surrounded by a rim structures as shown in Figure 4.1(b) is the cumulative effect of total ions fluence (1×10^{17} ions/cm²). Such pattern on the surface increases the possibilities of multiple scattering and trapping of incident light on the surface, thus, enhances the absorption of light.

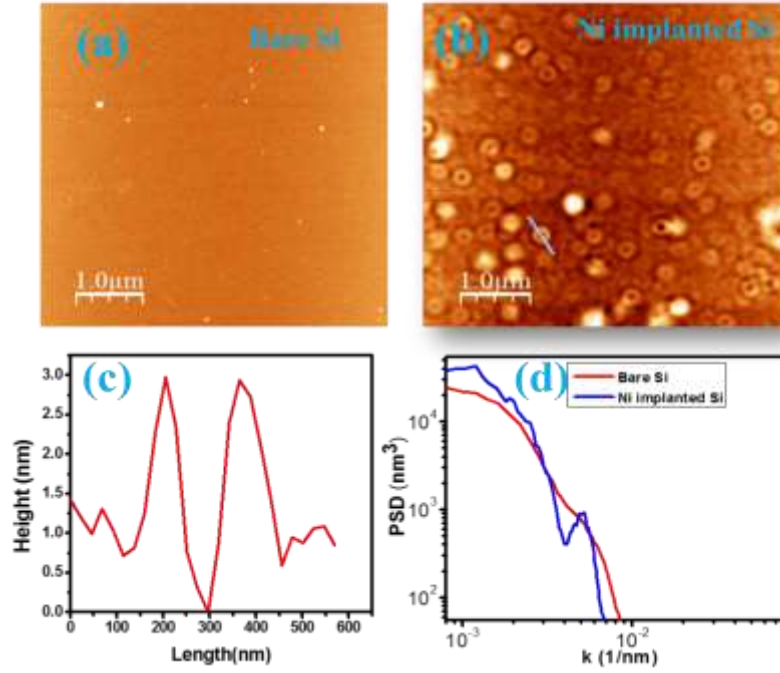


Figure 4.1: AFM topography of (a) bare Si(100) surface, (b) 10 keV Ni⁺ (fluence 1×10^{17}) bombarded Si(100) surface showing rim surrounded crater structure, (c) line profile along the marked line on (b), (d) The Power Spectral Density profiles of the bare and the irradiated Si, calculated from AFM data of (a) and (b).

Power Spectral Density (PSD) function represents the amplitude of roughness of a surface as a function of the spatial frequency. The inverse of the wavelength of a surface feature is the spatial frequency. The PSD function expresses periodic surface features in reciprocal space. The PSD spectra of the Si (100) surfaces before and after the irradiation, obtained from the AFM data, are shown in Figure 4.1(d). No peak is observed for smooth bare Si surface,

whereas a peak at k value $0.00508497 \text{ nm}^{-1}$, corresponding to surface pattern wavelength 1235.01 nm, is observed. This represents the periodic rim patterns of wavelength 1235 nm due to the Nickel ion bombardment on Si (100) surface.

The collision and consequent implantation details are calculated by SRIM [11] and experimentally investigated by Cross-sectional Transmission Electron Microscope (XTEM). When energetic ions are bombarded on a solid surface, the solid surface loses its crystalline property as well as the vacancies are created in the solid. The primary Ni ions stop at a distance and form a buried layer below the Si surface. SRIM distribution profile of the implanted Ni^+ ions and the Si vacancy generation for 10 keV Ni^+ ions bombardment on Si surface at normal incidence is shown in Figures 4.2 (a) and (b), respectively. The FWHM of the implanted Ni ions distribution is 13 nm (Fig. 4.2 (a)). SRIM calculation found about 279 Si vacancies per Ni projectile ion impact. The Si vacancy profile is shown in Fig. 4.2 (b) where an estimation of amorphous Si layer including the buried silicide layer is about 25 nm.

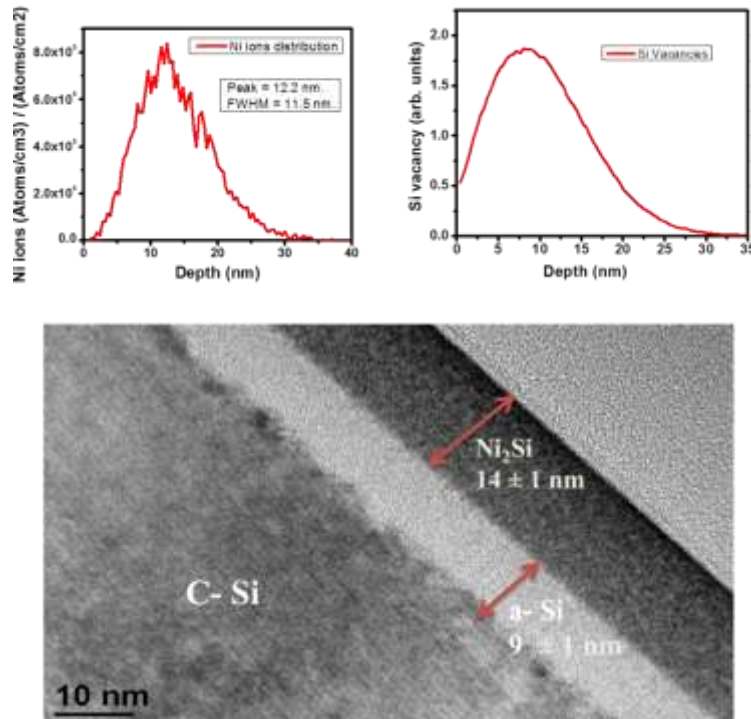


Figure 4.2: Distribution profile of (a) implanted Ni atoms and (b) Si vacancy due to 10 keV Ni ion bombardment on Si at normal incidence (TRIM simulation); (c) Cross-sectional TEM view of 10 keV Ni⁺ ion implanted Si(100).

Cross-Sectional Transmission Electron Microscopy (XTEM) image of the 10 keV Ni⁺ ion implanted Si is shown in Figure 4.2 (c). It indicates that the buried layer of Ni is formed below the Si surface, and Si (100) surface has lost its crystalline nature due to the ion bombardment. The Nickel atoms are implanted near the surface, and a layer of width about 14 ± 1 nm is formed, which are consistent with the SRIM calculation. The amorphous layer including the buried layer is observed about 23 ± 2 nm. The implanted Ni atoms in the Si matrix are mapped by the drift corrected energy dispersive X-ray (EDX) spectroscopy, and the images are shown in Figure 4.3. Figure 4.3 (a) is a cross-sectional scanning TEM (STEM) high angle annular dark-field (HAADF) image. STEM-HAADF, Si-K, Ni-K, and overlay map of Si and Ni, generated from area 1 as shown in Fig. 4.3 (a), are presented in Fig. 4.3 (b). X-ray line profile along line 2 as shown in Fig. 4.3 (a) is shown in Fig. 4.3 (c).

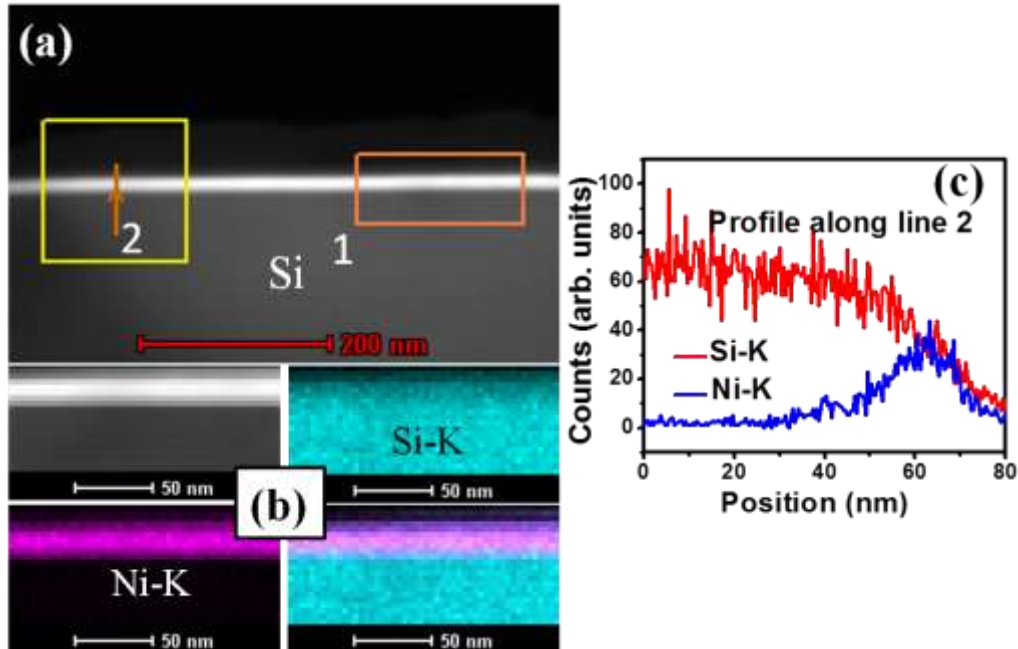


Figure 4.3: (a) cross-sectional scanning TEM (STEM) high angle annular dark-field (HAADF) image, (b) STEM-HAADF, Si-K, Ni-K and overlay map of Si and Ni, generated from area 1 of (a), (c) Si–K and Ni-K X-ray line profiles along the line 2 of (a).

The EDX measurement of implanted Ni atoms distribution could not give chemical nature of implanted Ni within the Si matrix. Spatially resolved Electron Energy Loss Spectroscopy measurements are taken at the marked positions of Ni implanted Si substrate (Figure 4.4). Low-loss (Plasmon) spectra at the marked position of Figure 4.4 (a) are shown in Figure 4.4 (b). Position 1 is the crystalline Si, position 2 is at the boundary, and position 3 is in the middle of the buried layer. The plasmon peak at 16.8 eV represents the crystalline Si. Plasmon peak for position 2 is also observed at 16.8 eV, however the width of the line is broadened, which indicates that the zone 2 is Si, but got amorphized. Plasmon peak for the middle of the implanted buried layer (position 3) is shifted and appears at 22 eV. It indicates that the buried layer is a Ni_2Si . Verleysen et al. [123] observed the plasmon peak at 19.7, 20.4, and 21.8 for NiSi_2 , NiSi , and Ni_2Si , respectively. The plasmon energy loss peak arises due to the energy loss of the transmitted electrons at each scattering event by creation of plasmon. The plasmon loss peak depends on the valence electron and dielectric properties of the specimen [124]. In the present experiment, the shift of Si plasmon loss peak from 16.8 to 22 eV confirms the formation of Ni_2Si . Ni-L_{2,3} core-loss peak (855 eV for pure Ni) is also monitored at the position of the Ni implanted Si sample (point 4 of Fig 4.4(a)). The core-loss spectrum is shown in Figure 4.4 (c) which confirms the presence of Ni in the buried layer and ensuring silicidation.

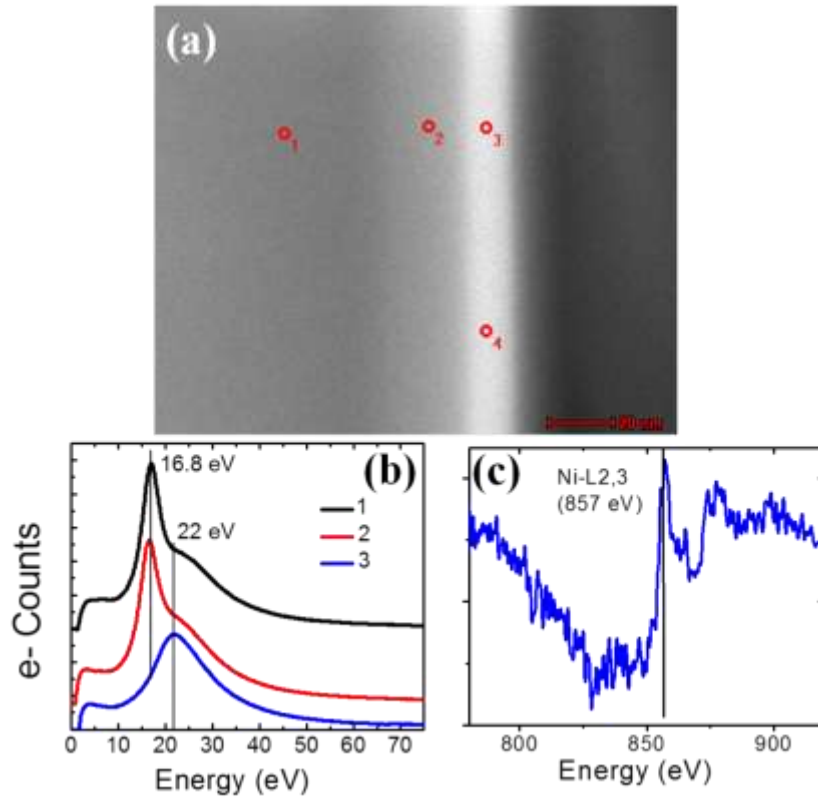


Figure 4.4: Cross-sectional STEM-HAADF and EELS spectra showing Nickel silicide formation during 10 keV Ni^+ ion bombardment on Si (a) Cross sectional STEM-HAADF image for ion fluence of 1×10^{17} ions/cm², (b) Low-loss spectra at t positions 1, 2, 3 of (a), (c) Core-loss spectra at Ni-L2,3-edge at position 4 of (a).

To confirm the Ni_2Si formation by ion implantation, Grazing Incidence X-ray Diffraction (GIXRD) pattern of the 10 keV Ni^+ implanted Si sample is obtained. The results of GIXRD measurements are shown in Figure 4.5. A weak peak of Ni_2Si (200) is observed, but no other phases are noticed. The presence of Ni_2Si phase is consistent with the EELS measurement. Dasgupta et al. [125] reported the presence of different phases of Nickel silicides when nanowire arrays were fabricated by thermal decomposition of silane on Ni foil and transferred on the glass slides for low background X-ray diffraction measurements. Priyadarshini et al. [126] found a weak peak of Ni_2Si (002) for magnetron sputtered deposited Ni film on Si substrate. In the present

case, both EELS and GIXRD measurement indicate the Ni_2Si layer formation due to 10 keV Ni ion implantation on Si(100).

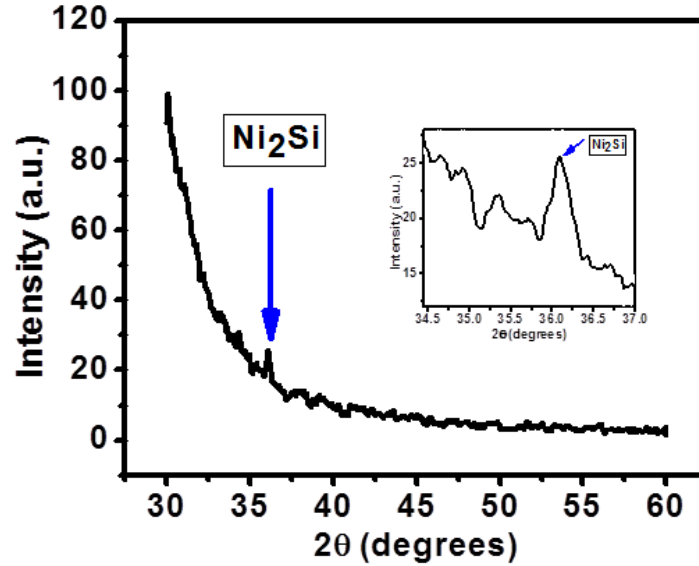


Figure 4.5: GIXRD spectra of Ni implanted Si samples.

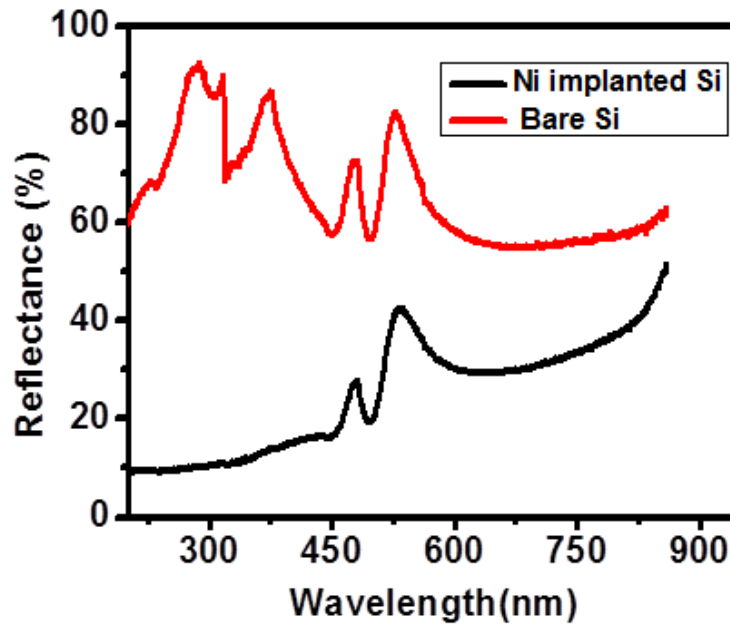


Figure 4.6: Reflectance data showing a decrease in reflectance from bare Si, to Ni implanted Si.

It is reported that metal silicide, in particular, nickel silicide is thermally and electrically stable and good absorber of solar light [118, 125, 127]. It is also demonstrated that the photo absorption is remarkably enhanced in the visible and infrared range for the NiSi_2 embedded a-Si compared to a-Si [118, 128]. Further, the enhancement is maximum when the embedded nanoclusters form a continuous layer. Catchpole et al. [113] showed further that the particle shape is a critical parameter for plasmon enhanced light trapping, cylindrical and hemispherical particles are much more efficient than spherical particles.

To measure the absorption of light by this nanopatterned and Nickel silicide embedded Si, we took the reflectance spectra of bare Si and 10 keV Ni ion-bombarded Si samples. The reflectance data is shown in Figure 4.6. The bare Si is highly reflective with a reflectance from 60 to 90% in the wavelength range of 200 to 800 nm. The reflectance is reduced to 9 to 40% in the same wavelength range for Ni implanted patterned Si sample. The absorption of light is maximum (93%) in the wavelength range 200 to 450 nm. The enhancement in this zone may be due to plasmonic absorption by Ni_2Si layer. Recently, similar enhancement is reported for Nickel Silicide nanoparticles in amorphous Si [128]. Dasgupta et al. reported fabrication of single crystalline, high conductivity Ni_xSi nanowires on Ni foil for antireflecting bottom electrode for photovoltaics. It is also reported that addition of plasmon active Ni_xSi enhances the absorption ability of a-Si [118, 128]. Plasmon induced resonance energy transfer and direct electron transfer from plasmon to a semiconductor can absorb the solar photon beyond the bandgap energy of the semiconductor, thus, expand the solar spectrum available for energy harvesting. Li et al. [116] demonstrated the energy flow between Ag nanocluster and Substrates by Electron Energy Loss Spectroscopy.

The present study shows that the addition of buried Ni₂Si layer can be used as good anti reflecting electrode as well as an intermediary between solar light and semiconductor for plasmon induced resonance energy transfer and direct electron transfer from plasmon to Si.

4.1.4 Conclusion

The controlled incorporation of plasmon active buried layer adds an intermediary between solar light and Si, thereby, opening a new way of increasing solar energy conversion by Si solar cell. Low energy nickel ion implantation forms such controlled buried layer and simultaneously modifies the surface with a regular pattern, which aids to absorb and trap more light. The cumulative effects of crater structure formation and plasmon active buried layer formation lead to increase the higher optical absorption in the visible range. However, the surface morphology (crater formation) is less effective than buried layer for higher optical absorption in this case. Another advantage of the present technique is that the Nickel silicide is formed just by ion implantation, whereas annealing at 500° C and 800° C is required to form silicide in the case of deposition of Si and Ni [118]. However, ion implantation induced damage may deteriorate the performance of actual solar cells; therefore, annealing may be required for curing the surface damage and better performance. For instance, the details of solar energy trap and transfer to Si via the buried layer are unknown. The present study opens up a new way of research and development on ion beam based minimum step low-cost solar device development and investigation. We have performed the experiments with crystalline Si; however it becomes amorphous at the very beginning of ion bombardment. Same experimental results are expected if one starts the experiment with a-Si.

4.2 Ripple pattern formation on Si by N⁺ ion bombardment, optical and wettability study of the patterned surfaces

4.2.1 Introduction

Low-energy ion beam sputtering (IBS) is a very important technique to fabricate nanoscale periodic patterns on a large area solid surface. Such types of periodic structures are very useful in the field of thin film growth, plasmonics, nanoscale magnetism, and catalyst [1-3]. Nano pattern formation on Si surface is already reported for very low energy (0.5 -2 keV) inert ion bombardment [129]. The study of ripple formation on Si by Nitrogen like reactive ion bombardment is interesting in the energy range of 5-12 keV because of the mass analyzed pure beam as well as higher sputtering yield compared to very low energy [41].

Besides the pattern formation on Si surface by ion beam irradiation, the study of the ion modified Si surface for the photovoltaic purpose is very important. Recently, we have reported that the optical absorption efficiency is increased in the metal ion implanted Si surface due to the formation of plasmon active nickel silicide layer [42]. Similarly, it is also reported that the presence of amorphous silicon nitride in solar cell increases the photovoltaic efficiency [130]. Silicon nitride top layer is used as anti-reflecting coating (ARC) in industrial silicon solar cells and third generation solar cells [130]. The main advantage of making ARC and textured surface is that it reduces the reflection of light on the front surface of silicon solar cell as well as increases the photocurrent [130-132]. Usually, ARC and surface texturing are achieved on Si surface by multi step processing [130-135]. Recently, it has been shown that the controlled silicon nitride could also be formed by low energy nitrogen ion implantation on Si surface [41].

Another important useful application of pattern formation is the tuning of wettability. Wettability is a very important surface property of materials, particularly for the interaction of the surface and biological substrates [136]. It can be controlled by changing surface chemical composition, surface texturing and engineering. The untreated smooth Si surface has the tendency to adsorb water i.e., hydrophilic in nature. So, the transformation of hydrophilic Si surface to hydrophobic surface is important because the hydrophobic Si surface, which can be used as a device, is safe from water and self-cleaning its surface. Therefore, the interest in tailoring the wettability in a control way is highly demanding. To control the hydrophobicity, the surface texturing is also important. Although there are several methods to control the hydrophobicity [137], the ion bombardment technique has more advantage due to its precise control in surface texturing and surface chemical change by varying ion beam parameters [24, 138-140]. The hydrophobicity is generally measured in terms of contact angle of water droplets on the surface. It is defined as “the angle θ made with three phase lines, solid, liquid, and vapor”. The contact angle is directly related to the surface energy [141], if the surface energy decreases, the contact angle increases and vice versa [24, 142]. It is also dependent on the surface chemical composition, which can easily be controlled by ion bombardment [24, 140, 143]. According to Wenzel [144], the contact angle is related to the roughness of the surface. It was observed that not only the surface roughness but also the patterned surface and wavelength of the pattern influence the wettability of the surface [139, 145]. Theoretically, the effect of surface morphology on wettability was also reported many years ago [146]. So, the experimental investigation of contact angle due to ion-induced patterned surface is very important due to its potential application in chip devices, solar cell, etc. [146-149]. A very few works were reported on the wettability study due to ion beam induced patterned Si surfaces (60 keV and 200 keV)

[138, 139] and mica surfaces (500 eV) [24, 142]. So far, in our knowledge, no study has been initiated on medium energy (10 keV) ion-induced hydrophobicity tailoring on Si surfaces, although we have recently reported the hydrophobicity study on mica surfaces by 12 keV Ar and N bombardment [140].

Here, we will discuss about the pattern formation on Si surface by N bombardment at different ion energy, and we will show that the wavelength and roughness of the ripple structure depend on the shape and size of the collision cascade. The ripple wavelength is proportional to the horizontal width of the collision cascade, whereas the roughness is proportional to the ion penetration depth. Also, we have investigated optical measurement for N bombarded patterned surfaces and observed that the optical absorption increases for patterned surface compared to the pristine Si. The interesting study is the tuning of hydrophobicity on Si surfaces by varying ion energy (5-12 keV). It has been observed that Ar bombardment cannot produce any surface pattern as well as the surface chemical composition is not changed, whereas N bombardment forms anisotropic ripple pattern and the surface chemical composition changes by forming silicon nitride. Also, the surface rms roughness increases slightly in case of Ar bombarded Si surfaces, but the rms roughness increases drastically for N bombarded surfaces. Due to textured periodic wavelike pattern formation and chemical modification, the water contact angle increases for all the N bombarded Si surfaces, and the hydrophilic Si surfaces transform to hydrophobic surfaces, whereas the contact angle of Ar bombarded Si surface does not increase.

4.2.2 Experimental

The commercially available polished and cleaned Si (100) samples were bombarded with 5 keV to 12 keV N⁺ and Ar⁺ ion beams at a constant fluence of 7×10^{17} ions/cm² at oblique angle 60°.

The other measurement details of surface morphology and UV-Visible spectrophotometer are already discussed in the previous section.

The sessile drop method used to calculate contact angle measurements were performed by a standard contact angle goniometer (ramé-hart model 250, USA) with DROPImage Advanced v2.4 software. We measured the contact angles of each samples at least on three different spots. During measurements, the room temperature and relative humidity were 27°C and 46%, respectively. The XPS of pristine and Ar & N bombarded Si surfaces have been measured using an Omicron Multi-probe (Omicron Nano Technology, UK) ultrahigh vacuum (UHV) system (base pressure $\sim 5.0 \times 10^{-10}$ mbar). A monochromatic Al K α source is used to provide photons of energy 1486.6 eV for XPS measurement.

4.2.3 Results and discussions

(a) Ripple pattern formation on Si by N⁺ ion beam

Figure 4.7 shows the morphologies of 5-12 keV N⁺ ion-irradiated Si (100) surfaces. The ripple wavevectors are oriented along the ion beam direction i.e., the parallel type of ripple patterns have been formed for oblique angle (60°) N⁺ ion bombardment. The power spectral density (PSD) with spatial frequency (k) along the projection of ion beam direction is shown in Figure 4.8. The ripple wavelengths for different energies are calculated from the peaks of PSD graph. This type of periodic pattern formation can be explained by well-established Bradley and Harper theory of ion sputtering [5]. To form periodic pattern on a solid surface, the necessary condition is the generation of surface instability. For N bombarded Si surfaces, the silicon nitride is formed at the interface of ion bombardment due to the reactivity of N ion. The chemically formed

inhomogeneous surface generates the instability due to the unequal sputtering of Si and its nitride [41].

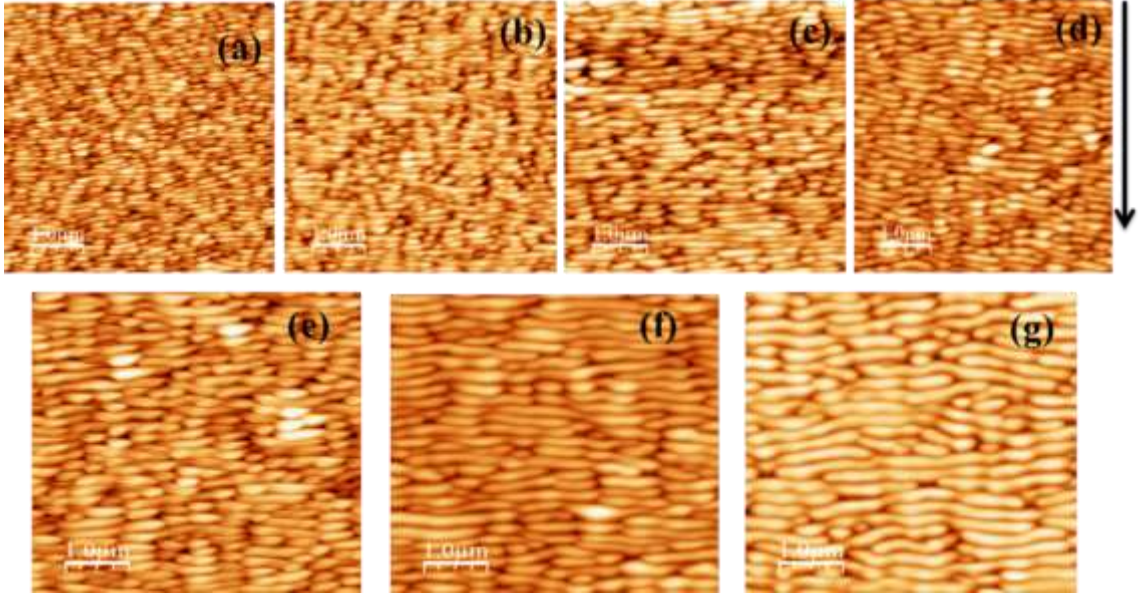


Figure 4.7: AFM images of (a) 5 keV, (b) 6 keV, (c) 7 keV, (d) 8 keV, (e) 9 keV, (f) 10 keV and (g) 12 keV N⁺ bombarded Si surfaces at incidence angle 60° with ion fluence 7×10^{17} ions/cm². The arrow in the right corner indicates the ion beam direction.

The rms roughness (\sim vertical dimension) of the ripple structures are calculated from the AFM images using WSxM freeware [12]. We have also calculated the N⁺ ion penetration depth and horizontal width of collision cascade i.e., the lateral straggling in Si target for the energy 5-12 keV using SRIM [11].

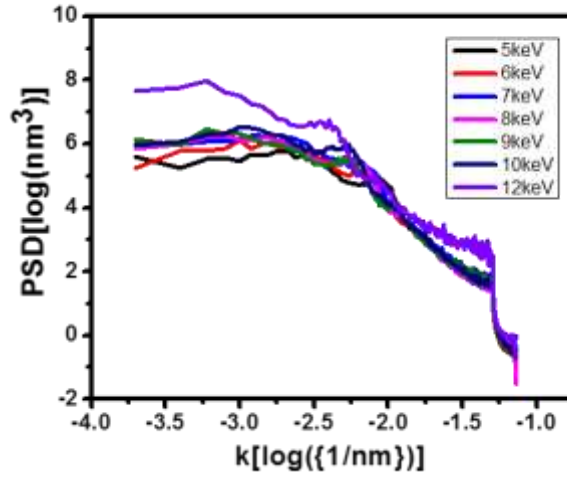


Figure 4.8: The power spectral density (PSD) function for all the ion energies with wavevector (k) along the projection of ion beam direction.

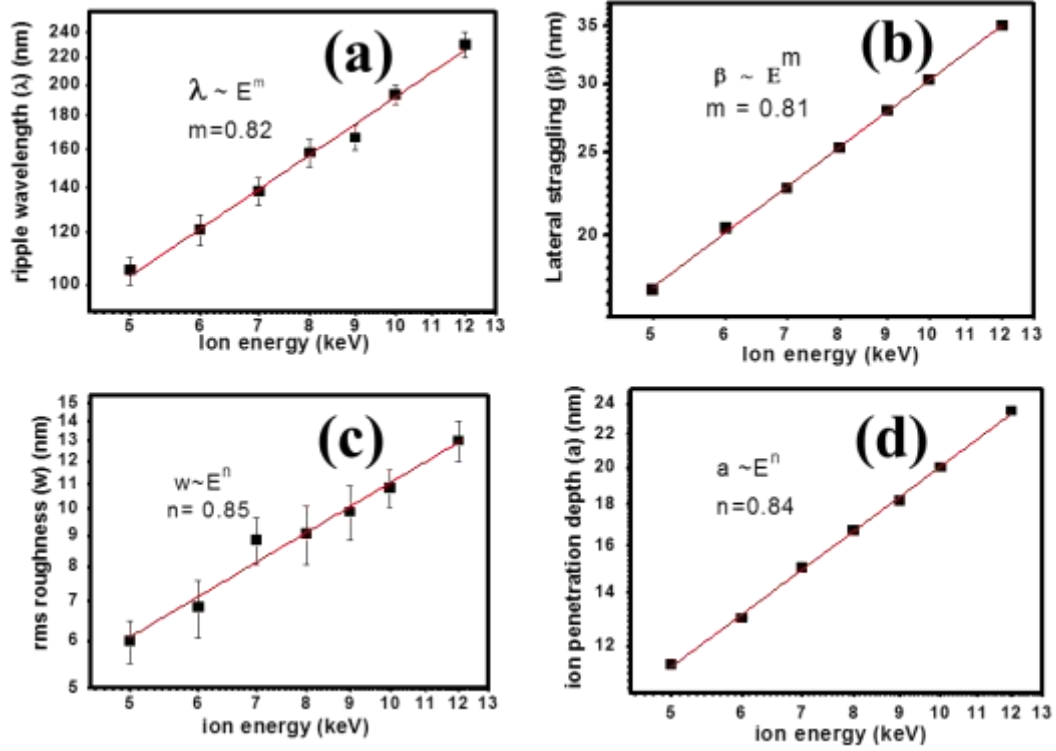


Figure 4.9: Variation of (a) ripple wavelength (λ), (b) lateral straggling (β), (c) rms roughness (w) of the surface and (d) ion penetration depth (a) with ion energy (E).

Figure 4.9 shows the variation of ripple wavelength (λ), lateral straggling of the collision cascade (β) of N^+ ion in Si, rms roughness (w), and ion penetration depth (a) with ion energy (E). It is found that the ripple wavelength and surface roughness increase almost linearly with ion energy (Fig. 4.9). The wavelength of the ripple is increasing with ion energy with coarsening exponent $m = 0.82$. A linear fit to the experimental wavelength vs. energy shows the scaling behavior as $\lambda \sim E^m$ with $m = 0.82$. The fitting of horizontal width of collision cascade (β) with energy yields $m = 0.81$. B. Khang et al. [120] reported that the wavelength of the developed periodic patterns would be proportional to the horizontal width of the collision cascade (β). Our experimental data is consistent with this prediction. In case of roughness vs. energy fitting, we get the relation $W \sim E^n$ with $n = 0.85$. The plot of ion penetration depth with energy gives the power $n = 0.84$. Thus, the increase of rms roughness (vertical dimension of the ripple) is linearly proportional to the ion penetration depth. So the ripple wavelength and rms roughness of the surface increase with ion energy. Also, the theoretically calculated lateral straggling and ion penetration depth of the collision cascade are directly correlated with experimentally observed ripple wavelength and surface rms roughness. This study will help the theoretical understanding of pattern formation by energetic ion bombardment.

(b) Optical study of N bombarded Si surface

The N^+ bombardment on Si surface leads to form the silicon nitride on the surface due to the reactivity of N atoms. The formation of nitride was confirmed by Electron Energy Loss Spectroscopy and X-ray photoelectron spectroscopy [41, 150]. We will also show the silicon nitride formation by N bombardment in the next section.

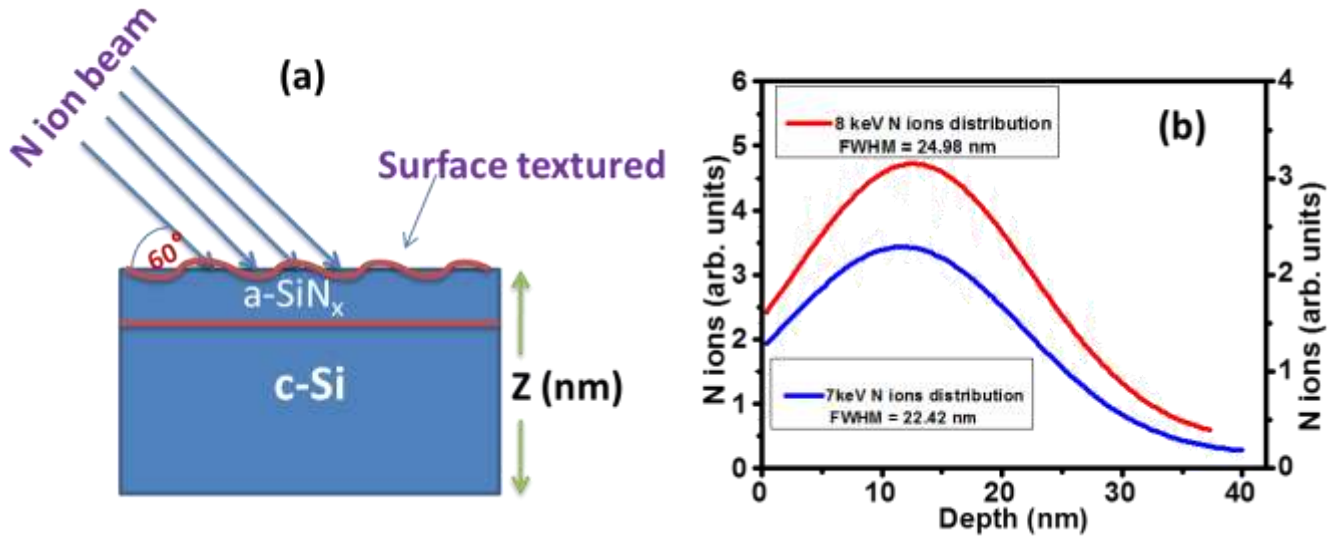


Figure 4.10: (a) Schematic of N^+ ion beam implantation on Si surface and (b) 7 keV, 8 keV N^+ ions distribution in Si calculated from TRIM simulation.

Figure 4.10 shows the schematic diagram of ion beam implantation and the distribution of implanted ions. Figure 4.10 (a) depicts the schematic of energetic ions (7 and 8 keV) bombarding at oblique angle 60° on Si surface. Figure 4.10 (b) presents the distribution of implanted N^+ ions in the Si with depth. It is observed that the average penetration depth is 14 nm, 16 nm, and average width is 23 nm, 25 nm for ion energy 7 keV, 8 keV, respectively. The implanted Nitrogen atoms react with the Si and form a silicon nitride layer of thickness equivalent to the ion penetration depth. Many researchers made the amorphous silicon nitride films by deposition, which is used as antireflective coating (ARC), thereby it increases the photocurrent and hence its photovoltaic efficiency [130-133]. To make textured amorphous Si surface, we have used ion beam implantation. Also, the effective surface area increases for the textured and roughed surface. The ripple patterned Si surface is a suitable for textured and roughed surface. The AFM images of pristine or bare Si and 8 keV N bombarded Si surfaces are

shown in Figure 4.11. The effective surface area after ion implantation is increased $\sim 5\%$ compared to the bare Si.

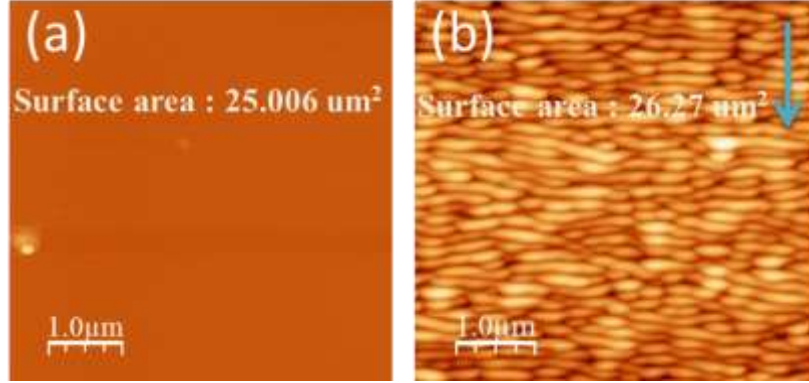


Figure 4.11: AFM images of (a) pristine or Bare Si (100) and (b) 8 keV N bombarded Si surface showing the increase in surface area.

To study the optical absorption of N implanted nano ripple patterned Si surfaces, we measured the reflectance of bare Si, 7 keV, and 8 keV N bombarded Si surfaces in the wavelength range 200 nm to 850 nm by UV visible spectrophotometer. The reflectance data of bare Si and N bombarded Si are shown in Figure 4.12. The variation of absorbance of N implanted Si surfaces and bare Si is discussed for different wavelength values. For the wavelength 200 nm, the absorbance of bare Si is 15%, whereas for 7 keV and 8 keV N^+ ions implanted Si surface, the absorbance increases to 60% and 80 %, respectively. For the wavelength 400 nm the absorbance of bare Si is 35%, whereas for 7 keV and 8 keV N^+ ions implanted Si surfaces, the absorbance increases to 75% and 88%. The absorbance of bare Si, 7 keV and 8 keV N implanted Si is 62%, 84% and 90% for wavelength 600 nm, and for wavelength 800 nm, these values are 74%, 87% and 92%, respectively.

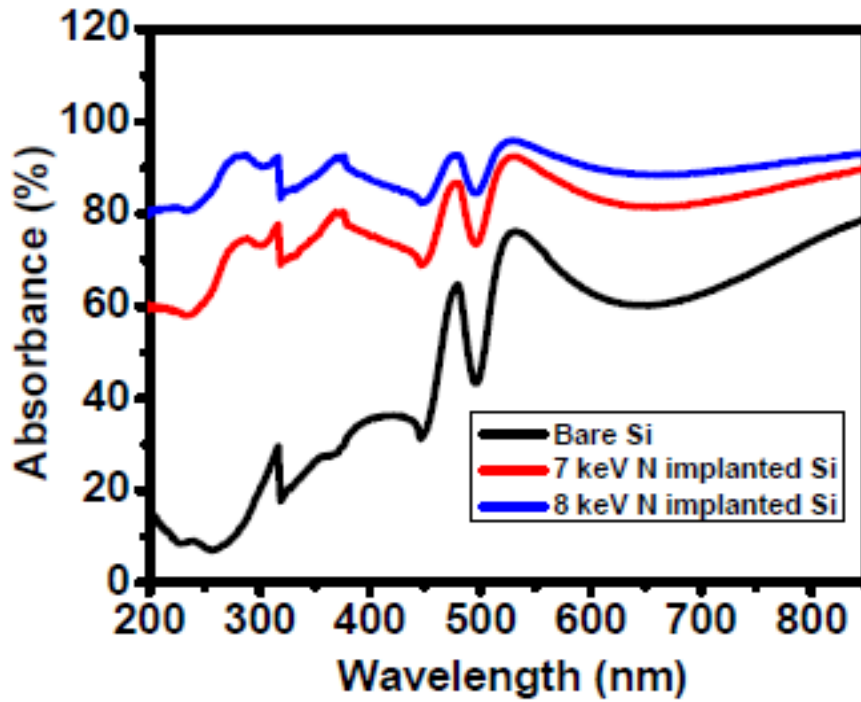


Figure 4.12: Absorption data of bare Si and 7 keV, 8 keV N bombarded Si samples showing an increase in absorption from bare Si, to N implanted Si. In the experiment the reflectance was measured. As the Si sample is opaque, no light was transmitted through it. The absorption is calculated by subtracting the reflected light from the incident light.

From the variation of absorbance, we can conclude that the optical absorption is increased from bare Si to N implanted Si surfaces. The increase in optical absorption means the decrease in optical reflection. Thus, the N implanted Si surfaces can be used as ARC due to its low reflectivity. Similar reduction of reflectivity for glass/ZnO substrate with SiN_x and without SiN_x layer was reported where the reflectivity was decreased by 1.6 % for glass/ZnO substrate in the presence of SiN_x layer in the wavelength range 400 – 800 nm [132]. In the present case, the enhancement of optical absorption of ion bombarded Si surfaces may be due to the presence of silicon nitride ARC and nano textured surface. The increase of light absorption can also be explained in terms of surface roughness. For the bare Si surface, the rms roughness is 0.11 [42], which is atomically flat, but for N bombarded Si surface, the rms roughness varies 6 nm to 12

nm for the energy 5 – 12 keV. The flat surface reflects the light more than it absorbs on the surface, whereas for the highly roughed surface, the light is trapped and gets multiple reflection, so the reflection is less than that of atomically flat surface.

The enhancement of light absorption efficiency on Si surfaces by a single step ion beam irradiation has been studied here. This type of study helps us to develop highly absorptive surface, which is essential for photovoltaic devices and microelectronics. Another advantage of the present study is that the optical band gap can be controlled by the ion beam parameters, and the implanted Si surface can be used as antireflective coating (ARC), which is useful for solar cell.

(c) Tuning of hydrophobicity of Si surfaces by low energy ion beam induced nanopatterning

The tuning of hydrophobicity is studied for two types of ion bombardment, one is chemically active N^+ ion which forms well defined ripple pattern (Figure 4.7) on Si surface, and another is inert Ar^+ ion, which cannot form well defined ripple pattern. The AFM images for 5, 8 and 10 keV Ar bombarded Si surfaces at oblique ion incidence 60° with the surface normal with ion fluence 7×10^{17} ions/cm² are shown in Figure 4.13, which illustrates the absence of any well-defined pattern formation. The absence of pattern formation on Si surface by Ar^+ ion bombardment at this ion energy i.e., 5-12 keV in the present case was also observed earlier [40, 41, 151].

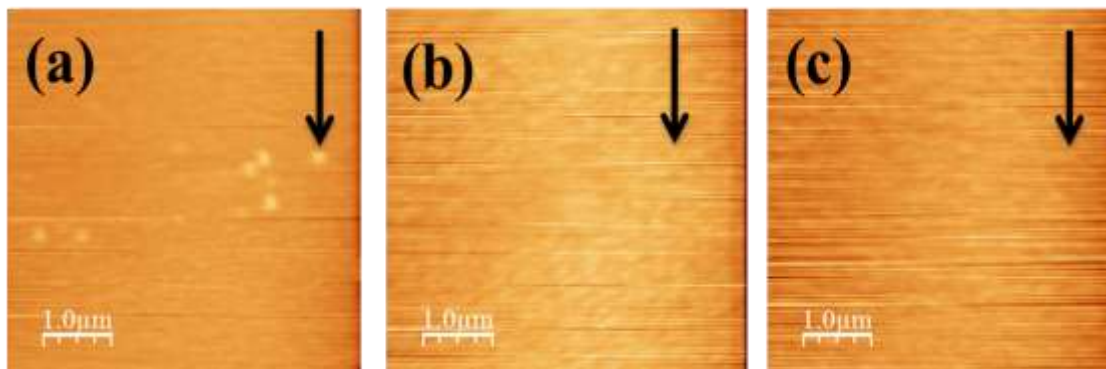


Figure 4.13: AFM images of (a) 5, (b) 8 and (c) 10 keV Ar bombarded Si surfaces at an oblique ion incidence 60° with the surface normal with ion fluence 7×10^{17} ions/cm². The arrow in the right corner of each AFM image indicates the ion beam direction.

Wettability of the surface is measured in terms of contact angle with water droplet. Figure 4.14 (a) shows the schematic diagram of the water contact angle on a patterned surface. The images of water droplets on pristine Si, 5 keV Ar bombarded, and 5 keV N bombarded Si surfaces are shown in Figures 4.14 (b-d). The contact angle has been found to be 74° for pristine Si i.e., hydrophilic surface. Garg et al. also reported the contact angle of pristine Si surface close to 75° [138]. The Ar bombarded Si surfaces also show contact angle $< 75^\circ$, whereas the N bombarded Si surfaces show the contact angle $> 90^\circ$, which suggests the transformation of a hydrophilic to hydrophobic surface. The contact angle for all the samples was recorded after 10 minutes when it was stabilized. The stabilization of contact angle with time is shown in Figure 4.15 (a) for 10 keV N bombarded Si surface. Figure 4.15 (b) shows the contact angle and rms roughness vs. incident ion energy (5 – 12 keV Ar). The contact angle remains almost same as pristine Si surface, and rms roughness increases very slowly with ion energy. In case of N bombarded Si surface, both the contact angle and rms roughness increase with ion energy as shown in Figure 4.15 (c).

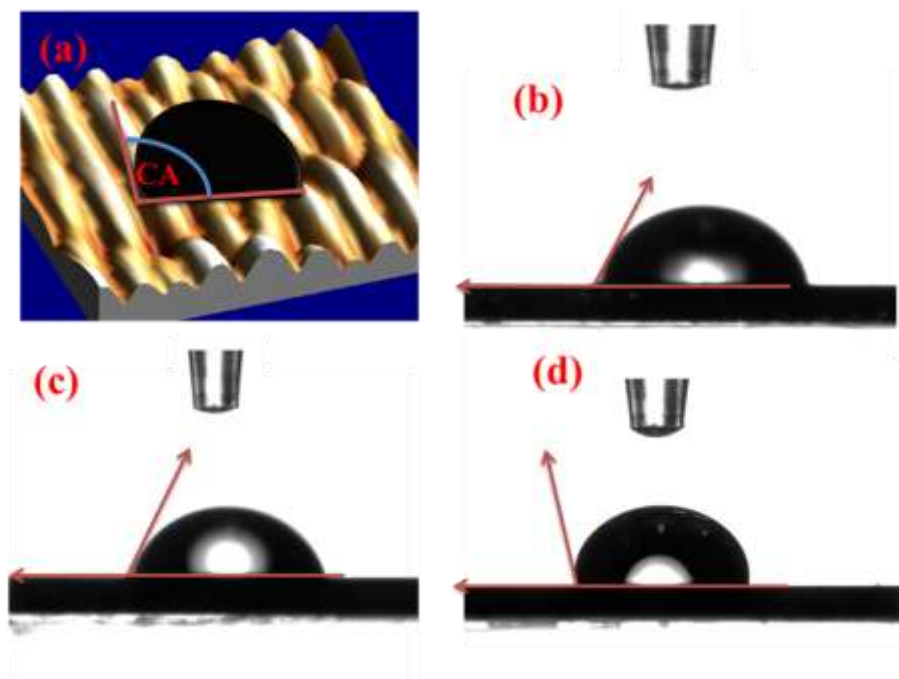


Figure 4.14: (a) Schematic diagram of water droplet on rippled Si surface. The water droplet on (b) pristine Si, (c) 5 keV Ar bombarded and (d) 5 keV N bombarded Si surface showing the contact angle

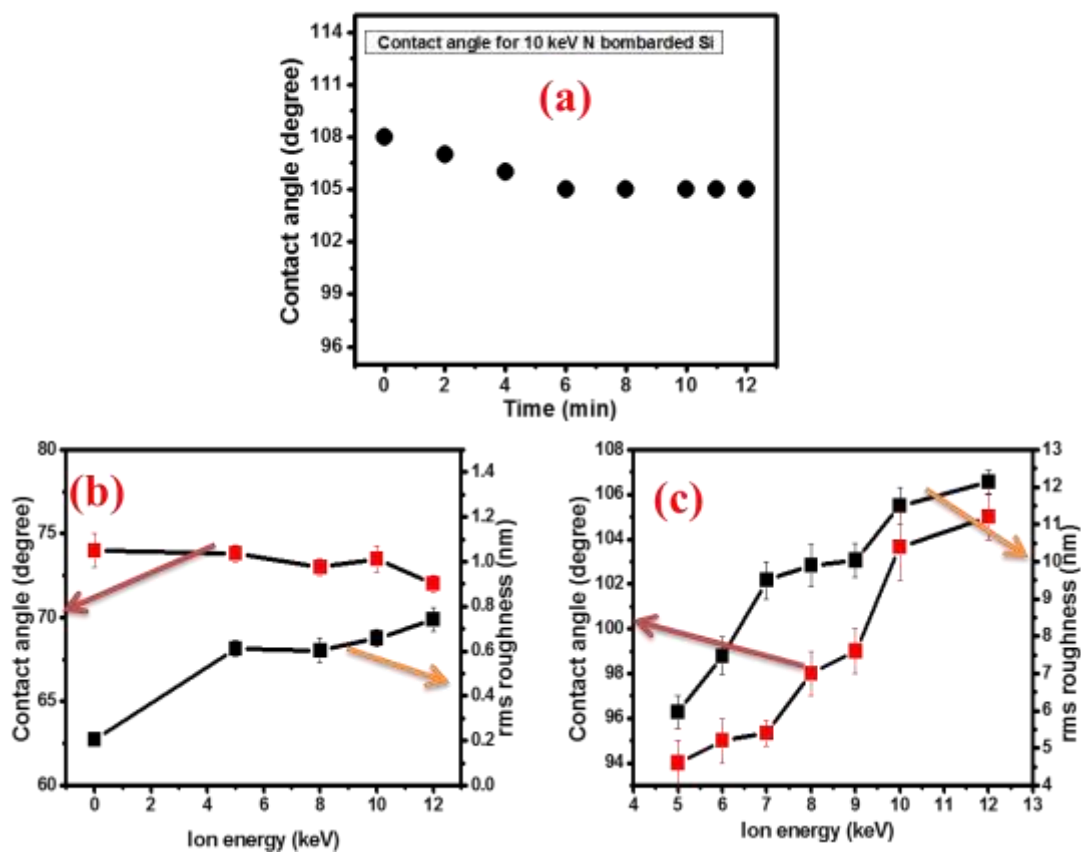


Figure 4.15: (a) Contact angle of 10 keV N bombarded Si surfaces with time. (b) Contact angle and rms roughness of pristine Si and Ar bombarded Si surfaces. (c) Contact angle and rms roughness of N bombarded Si surfaces with ion energy.

The contact angle of a surface depends on the surface energy [152]. If the surface energy of a surface decreases then the water contact angle on the surface increases [24, 138, 140]. Wenzel introduced the effects of roughness on contact angle and gave a formula as

$$\cos \theta_R = r \cos \theta_F$$

where r is called as roughness factor defined as the ratio of average area to the projected area. θ_R and θ_F are the contact angle of water droplet with rough surface and flat surface, respectively. The value of r is always greater than 1 for rough surface, so for $\theta_F > 90^\circ$, θ_R increases, but for $\theta_F < 90^\circ$, it decreases. So, according to the Wenzel, with increasing surface roughness, the hydrophobic surface will be more hydrophobic and hydrophilic surface will be more hydrophilic. This equation cannot explain the transition of hydrophilic to a hydrophobic surface. The N bombarded Si surfaces follow the Wenzel equation as with increasing roughness with ion energy, the contact angle also increases. For Ar bombarded Si surfaces, the contact angle decreases slightly with ion energy as the contact angle for 5 keV Ar bombarded surface is less than 90° . Although the decrease of contact angle is very small as well as the rms roughness also increases slightly as shown in Fig. 4.15 (b). Garg et al. reported the increase of contact angle by 60 keV Ar^+ ion bombardment on Si surface [138]. They explained the increase of contact angle on the basis of surface amorphization after ion bombardment. The amorphization leads to decrease of surface energy and hence increase its contact angle, but it was also shown that contact angle of Si surfaces reduced due to 200 keV Ar^+ ion bombardment [139]. In this ion energy (200 keV), the

surface can be totally amorphized and decrease the surface energy, hence contact angle should increase after ion bombardment. So, the amorphization is not the only parameter to explain the increase of contact angle, the surface chemistry and surface roughness are also important parameters for tailoring the contact angle.

The contact angle can be correlated with the ion beam parameters. The wavelength of ripple pattern for N bombarded Si surfaces increases with ion energy as shown in the previous section (Fig 4.9 a). So, the contact angle also increases with ripple wavelength. We have previously shown (Fig. 4.9) that the ripple wavelength and rms roughness increase linearly with the horizontal width of the collision cascade and ion penetration depth i.e., vertical dimension of collision cascade, respectively. So, the contact angle can be correlated to the theoretically calculated horizontal width of collision and ion penetration depth, and contact angle increases with both horizontal width of collision and penetration depth, as contact angle increases with ion energy. This was also previously observed that wavelength of the pattern surface has a great influence on wettability [139, 145]. The roughness of the surface pattern also play a vital role on hydrophobicity [153], textured and rough surface are water repellent like plant surfaces (lotus leaves). It was also shown that Si surface shows superhydrophobic when rough and pattern are formed on it [145].

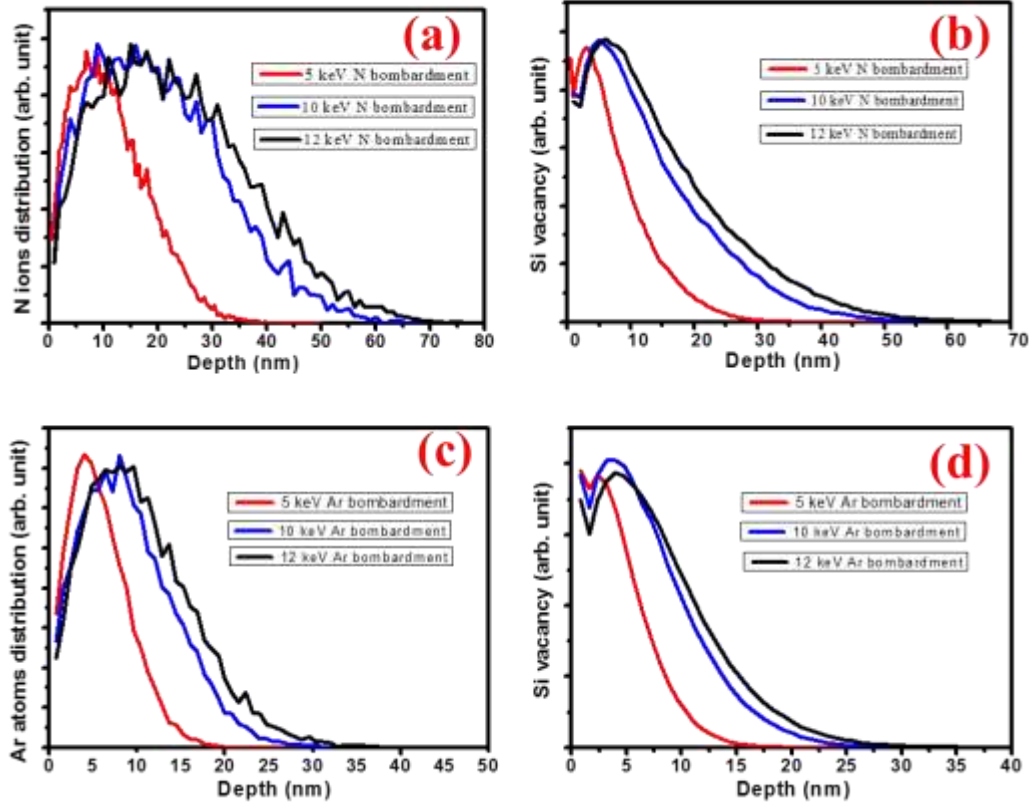


Figure 4.16: TRIM calculation of (a) N atoms distribution in Si for different energy, (b) Si vacancy for N bombardment, (c) Ar atoms distribution in Si and (d) Si vacancy for Ar bombardment at an incidence angle 60° with different ion energy.

As Wenzel equation cannot explain the transition from hydrophilic to hydrophobic surface, we have investigated the details of interface and chemical composition to explain this transition. We have calculated TRIM [11] simulation to know the penetration depth and vacancy creation, which are shown in Figure 4.16. The distribution of 5, 10, and 12 keV N and Ar atoms on Si as well as vacancy of Si due to ion bombardment are shown in Figures 4.16 (a-d). It is clear from Figures that N ions penetrate more depth than Ar ions; also the N ions create more Si vacancies. However, this will not affect the contact angle, as it is a near surface phenomenon. The TRIM estimation is consistent with previously done cross-sectional Transmission Electron Microscopy

(TEM) measurement for 12 keV Ar and N bombardment on Si surfaces at ion fluence 7×10^{17} ions/cm² [41]. The cross sectional view of 12 keV Ar and N bombarded Si surfaces is shown in Figure 4.17. The wave like nature of the surface is also reflected from cross sectional TEM image for N bombarded Si surface, and for Ar bombarded Si surface, no such pattern is formed. From TEM images, we can see that both the surfaces become amorphous at this ion energy.

We have performed XPS measurements to investigate the change of surface chemistry due to ion bombardment. The high-resolution XPS of Si 2p spectra for pristine Si as well as 10 keV Ar & N bombarded Si surfaces are shown in Figure 4.18. The XPS of pristine Si and Ar bombarded Si (Figs. 4.18 a & b) surfaces show Si peak and native oxide peak which is absorbed from environment, but N bombardment changes its chemical nature by forming silicon nitride (Si₃N₄) as shown in Figure 4.18 (c). The Ar bombarded Si surface shows no chemical alteration as clear from Figure 4.18 (b). Si 2p peaks for pristine and Ar bombarded Si are best fitted by two peaks, one elemental Si and another SiO₂. Si 2p peak for N bombarded surface can be best fitted by two Lorentzian- Gaussian peaks, one elemental Si (B.E $\sim 99.4 \pm 0.2$ eV) and another Si₃N₄ (B.E ~ 101.6 eV). From this Figure, we observe the decrease of elemental Si intensity for N bombardment compared to pristine Si, and Si₃N₄ peak intensity is high, which indicates most of the Si reacts with N ions to create nitride. Our group also previously reported the Si₃N₄ formation due to N ion bombardment on Si by XPS [150] and Electron Energy Loss Spectroscopy (EELS) measurement [41]. However, the silicon nitride is hydrophilic [154-156], but in the present case, all the N bombarded Si surfaces show hydrophobic nature. This may be due to the surface texturing, anisotropic ripple pattern, chemical modification, and also high rms roughness.

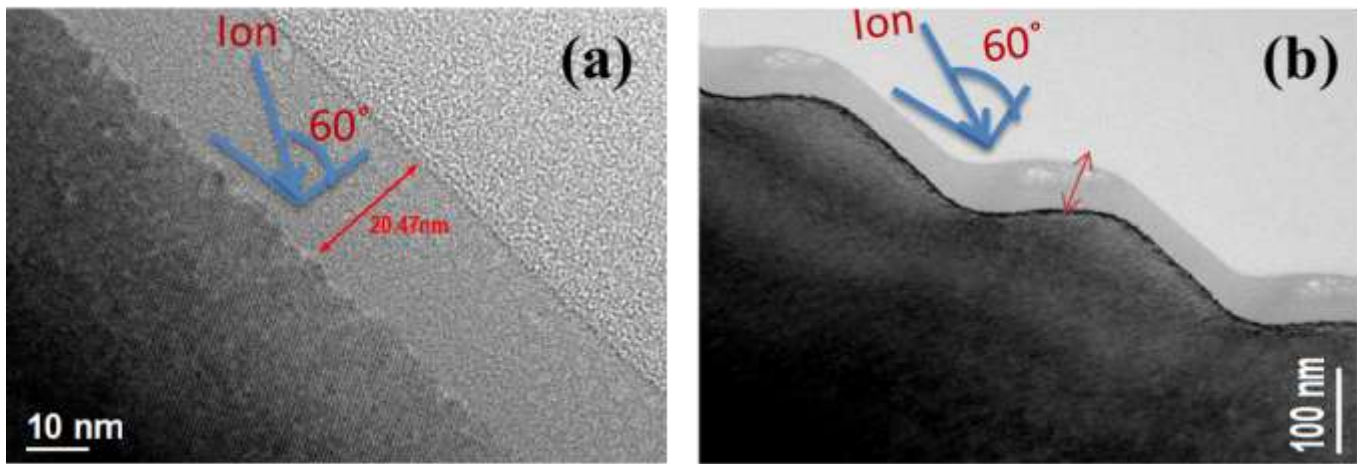


Figure 4.17: Cross sectional TEM view of (a) 12 keV Ar and (b) 12 keV N bombarded Si surface with ion fluence 7×10^{17} ions/cm² at an incidence angle 60° with the surface normal. [41]

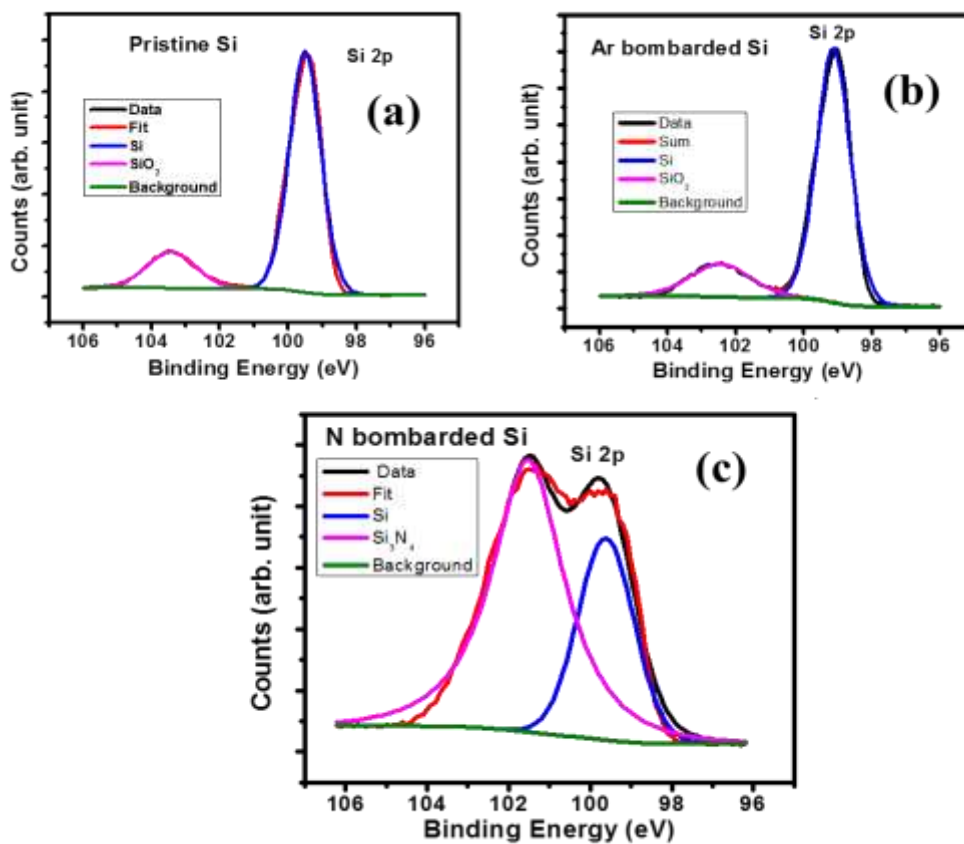


Figure 4.18: Si 2p high resolution XPS spectra for (a) pristine Si, (b) 10 keV Ar bombarded Si surface and (c) 10 keV N bombarded showing Si₃N₄ formation.

We have also calculated the surface area of N and Ar bombarded Si surfaces and found that the surface area increases 5-8% for N bombarded surfaces, whereas for Ar bombarded surfaces, negligible increase of surface area is observed. As the surface energy depends on the surface area, the increase of surface area leads to decrease in surface energy; as a result the contact angle of N bombarded surfaces increase. The XPS results show that the oxide layer exists on both the pristine and Ar bombarded Si surfaces, but for N bombardment, the oxide layer is sputtered away and Si_3N_4 is formed. It was observed that the contact angle of Si increases after the removal of oxide layer from Si surface [155]. Interestingly, we have formed silicon nitride on Si surface by energetic ion bombardment, and the concentration of N is very less compared to other conventional deposition methods. So, the hydrophilic nature of Si_3N_4 has not influenced much on contact angle in case of N bombarded Si surfaces. Previously, we observed hydrophobic surface of mica [140] where the Si_3N_4 was also formed on the surface [143]. Silicon nitride is a very useful material like it can be used as a good anti-reflective coating (ARC) as the light absorption increases on its surface [39]. It has many other applications also like it can be used as an interfacial surface between cells and large-scale integration devices, ion-sensitive field-effect transistor technology [157]. So, the hydrophobic behavior of N bombarded Si surfaces, where Si_3N_4 presents, is very important for the technological application.

4.2.4 Conclusion

In summary, we have studied the ripple pattern formation on Si surfaces by 5-12 keV N^+ ion bombardment. The theoretically calculated lateral straggling and ion penetration depth of the collision cascade are proportional to the experimentally observed ripple wavelength and surface rms roughness for N bombarded surfaces. The enhancement of optical absorption for N bombarded Si surfaces is also observed due to the silicon nitride ARC formation and increase of

surface area. This type of surface is useful in nanoelectronic devices and solar cell device. We have also studied the pattern formation on Si surfaces by inert Ar^+ ion bombardment and observed the absence of any pattern formation. We have modified the Si surface both physically and chemically by forming well periodic anisotropic ripple pattern and silicon nitride layer by reactive N^+ ion bombardment, whereas it is slightly physically modified by inert Ar^+ bombardment.

Due to the periodic ripple pattern formation and high rms roughness, the water contact angles of N bombarded Si surfaces increase with incident ion energy. However, the water contact angle does not vary so much compared to pristine Si surface in case of Ar bombardment. The contact angle variation with ion energy follows the Wenzel equation for both Ar & N bombarded Si surfaces. The contact angles of N bombarded Si surfaces are well tuned and correlated with ripple wavelength, theoretically horizontal and vertical dimension of collision cascade. In this way, one can tailor the hydrophobicity of Si surface by reactive ion bombardment.

Chapter 5

The modifications of muscovite mica surface by low energy ion bombardment

This chapter mainly describes the ripple pattern formation on muscovite mica like multielemental surface. The periodic pattern formation mechanism has been described in terms of existing continuum models as well as dynamic scaling theory. Mica $[\text{KAl}_2(\text{Si}_3\text{Al})\text{O}_{10}(\text{OH})_2]$ being a multielemental surface, its chemical composition can be well tuned by energetic ion bombardment. The detailed surface chemical composition and several compounds formation after two types of ion bombardment, one inert Ar^+ and another reactive N^+ ion, are discussed. Also, the transformation of super hydrophilic mica surface to hydrophobic surface is presented here.

Related publications

1. **Dipak Bhowmik**, Prasanta Karmakar, “Physicochemical variation of mica surface by low energy ion beam irradiation” **Nuclear Inst, and Methods in Physics Research B** 422 (2018) 41–46.
2. **Dipak Bhowmik**, Debasree Chowdhury and Prasanta Karmakar, “Dynamic scaling behavior of mica ripples produced by low energy Ar^+ ion erosion” **Surface Science** 679 (2019) 86.
3. **Dipak Bhowmik** and Prasanta Karmakar, “Tailoring and investigation of surface chemical nature of virgin and ion beam modified mica surface” **Surf. Interface Anal.** 51 (2019), 667–673.

5.1 Dynamic scaling behavior of mica ripples produced by low energy Ar⁺ ion erosion

Muscovite mica is a naturally available having important property with good conductor of heat but a poor conductor of electricity, it also possess high-dielectric properties. There are mainly four types of mica (1) Muscovite, (2) Phlogopile, (3) Biotile, and (4) synthetic. The natural mica minerals (1-3) are readily available and inexpensive. We chose muscovite mica because it is transparent, flexible and thin sheet can be formed from it. This type of structure is also important due to its layered structures consisting of negatively charged alumino-silicate sheets that are bound to alternating layers of K⁺ ions [24, 158] . The most important property of mica is that it can be easily cleaved to get an atomically flat surface which is very suitable substrate for the study of ion beam irradiation as well as biological substrate. Mica is used as a substrate in scanning probe microscopy, biotechnology, and materials science [60, 159-163]. Recently, the use of mica in bio-science has been increased enormously for its easily available atomically flat smooth surface.

The presence of regular nano-pattern with controlled hydrophilic properties is highly desired for various applications from supported lipid bilayer membrane, thin film deposition, to synthesis of organic functional materials [164, 165]. The virgin mica is hydrophilic in nature [24]. The change of hydrophilic nature of mica surface is very important for the study of interactions between surface, bio membrane, and proteins [166, 167]. Although the research work on muscovite mica is limited, the study on mica crystals is a great interest for more than two decades by heavy ion irradiation [168]. F. Thibaudau et al. [168] observed the formation of latent tracks in mica surface induced by swift Kr⁺ ions. The nanoscale hillocks formation by

highly charged ion on mica attracted more attention [169]. Recently, very low energy (eV) ion beam induced nano patterning and hydrophobic nature of mica surface have been reported [24, 34]. Buzio et al. [170] also showed the ripple structure of the mica surface by 1.04 keV Ar⁺ ion sputtering at an incidence angle of 35°.

Low energy ion sputtering is well known as a single step process for nanopatterning on a large area surface. By varying ion incidence angle [171], ion, and target combination [34, 42, 80], different types of patterns like dot, rim/crater, ripple etc. can be formed on a wide range of materials. To explain the nano-pattern formation, several continuum models are proposed, but none can describe the experimental observations completely. As an alternative approach, we have used the scaling theory to describe the nature of growth of the surface morphology with ion fluence. In this approach, the surface roughness is measured as a function of time and system size. From the variation of roughness and other functions, the exponents are calculated to describe the growth of the surface. In recent years, the dynamic scaling behavior of thin film growth by various deposition methods has been widely studied [95, 97, 99]. Also, the growth dynamics of Si nanostructures by ion beam erosion has been investigated [2, 103], but a very few study has been initiated for ion beam induced pattern formation on mica surface [34, 170, 172, 173]. Thus, the detailed study of the growth of interface dynamics of mica surface due to ion beam erosion will explore better understanding of pattern evolution mechanism, which in one hand will make further advancement of the theoretical models on ion beam induced pattern formation phenomena on compound material surfaces, and in other hand will enrich the control on ion erosion technique of pattern formation process.

Here, we have studied the morphological growth of ripple pattern on mica surface by 12 keV Ar⁺ and N⁺ ion bombardment at oblique angle incident 60° for various ion fluences. The

surface morphologies of ion sputtered samples have been investigated by atomic force microscopy (AFM). A detailed analysis of the dynamic scaling exponents as well as the curvature dependent coefficients has been done in the context of dynamic scaling theory and discussed within the framework of theoretical models related with Ion Beam Sputtering (IBS) induced pattern formation process.

Freshly cleaved mica sheet of approximate size $1\text{ cm} \times 1\text{ cm}$ were irradiated by 12 keV Ar^+ ions at oblique angle incidence 60° with respect to surface normal. The irradiation was done in VECC by ECR ion source, the details of which have already discussed in the previous chapters. The morphologies of the irradiated mica samples were investigated using Bruker Atomic Force Microscopy (AFM), Multi-Mode V, in-house surface characterization facility of VECC, Kolkata. The surface rms roughness, lateral correlation length, ripple wavelength, and other statistical information of the surfaces were extracted from the AFM images using WSxM freeware (version 5.0 Develop 4.1) [12]. We have taken AFM images of a sample at least at four positions. The average values of surface rms roughness, correlation length, and ripple wavelength are calculated from these AFM images. The error bars in the plots indicate the standard deviation of the average value.

The curvature dependent erosive co-efficients, mass redistribution, and ion implantation contributed terms for 12 keV Ar^+ ion-bombarded mica surfaces at 60° have been computed using TRIM estimation [11]. The ion beam parameters, i.e., the average ion penetration depth (a_{impl}) = 24.8 nm, longitudinal width of the implanting ion distribution (σ_{impl}) = 10.2 nm, and lateral width of the implanting ion distribution (μ_{impl}) = 7.9 nm for ion implantation contribution as well as a_{sputt} = 16 nm, σ_{sputt} = 11.6 nm, μ_{sputt} = 5 nm for sputtering contribution from

distribution of recoils atoms in curvature dependent coefficients are calculated using TRIM and used to compute the curvature dependent coefficients. Considering the constituent elements and their stoichiometric ratio in mica, the sputtering yield has been calculated from TRIM. The average travel distance (δ) of recoil atoms for calculating the mass redistribution contribution is estimated by $\delta = N_D(d_R - d_V)$ [66], where N_D is the total number of displacement per ion and d_R (d_V) denotes the mean depth of recoils (vacancies). Both N_D and d_R (d_V) are calculated from TRIM.

Figures 5.1 (a)-(h) show a series of AFM images of virgin mica and 12 keV Ar^+ ion-bombarded mica surfaces for ion fluences ranges from 2×10^{17} to 1×10^{18} ions.cm⁻². From AFM morphology, it is observed that the virgin mica is flat with very low roughness ~ 0.7 nm. After the bombardment, the one-dimensional patterns with alternate descending and ascending step, called ripples, are formed. Similar ripple pattern formation on mica surface by lower energy (500 eV) Ar^+ ion bombardment was also reported earlier [34]. The inset of the AFM images is the Fast Fourier Transform (FFT) images, which show that the ripple wavevector is oriented parallel to the ion beam direction. The surface does not show any periodic pattern up to fluence 2×10^{17} ions.cm⁻² and above which the patterns are observed, which can be considered as a threshold fluence of ripple formation for 12 keV Ar^+ ion and mica combination at incident angle 60° . The evolution of ripples due to energetic ion bombardment has been explained by various continuum models [5, 6, 8, 26, 27, 54, 63, 64, 77, 174-176]. The first idea was introduced by Bradley and Harper in 1988 [5], well-known as linear BH theory, where the generation of ion beam induced surface instability relies on the competition process between surface roughening via surface geometry and incident angle dependent sputter erosion and surface smoothing via thermally activated surface self-diffusion. During simultaneous play of smoothing and roughening

processes, a Fourier mode whose amplitude most rapidly grows over the other wavelengths finally dominates ripple morphology on the surface.

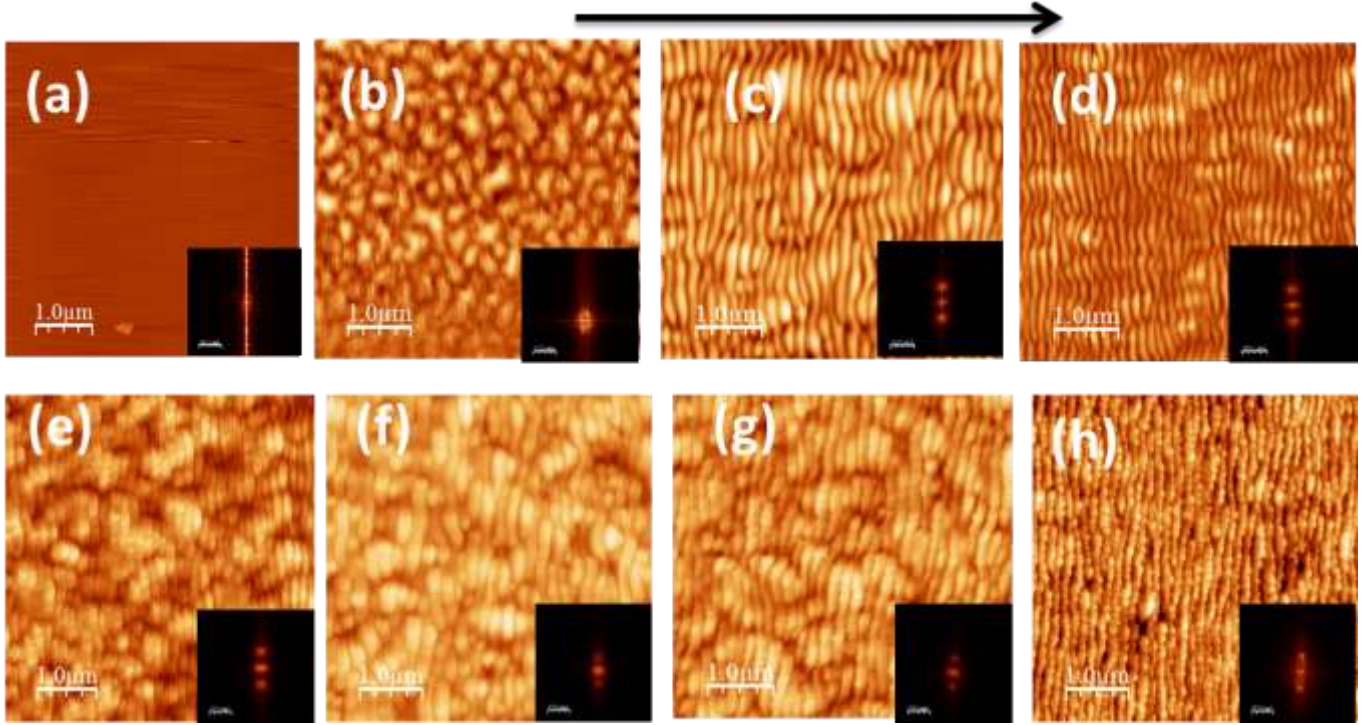


Figure 5.1: AFM morphologies of (a) virgin mica, 12 kV Ar⁺ bombarded mica surfaces with ion fluences (b) 2×10^{17} , (c) 3×10^{17} , (d) 5×10^{17} , (e) 6×10^{17} , (f) 8×10^{17} , (g) 9×10^{17} , and (h) 1×10^{18} ions.cm⁻² at 60° with the surface normal. The FFTs ($50 \mu\text{m}^{-1} \times 50 \mu\text{m}^{-1}$) are shown in the corner of each AFM images. The arrow indicates the ion beam direction.

The ripple patterns are formed on the ion bombarded surface due to the generation of surface instabilities [8, 27, 41]. The instabilities are generated during ion bombardment due to initial perturbation on the surface [70], presence of contamination [20], unequal sputtering [41], redistribution of surface atoms [8, 174], and local curvature dependent sputtering [5]. In the present case, mica [KAl₂(Si₃Al)O₁₀(OH)₂] is a multi-elemental compound. When the ion beams

are bombarded on crystalline mica, it loses its crystalline property as well as sputters the different elements of mica at different rate; the sputtering of all the surface elements generates the additional roughening instability. BH theory successfully explains the evolution of ripples at oblique ion incidences, their orthogonal rotation after a certain incident angle, the exponential increase of ripple amplitude, and constant ripple wavelength for initial increase of ion sputtering time etc. Although, this theory falls short to explain phenomena, especially observed for long sputtering time like saturation of ripple amplitude, ripple coarsening etc. These inadequacies have been recovered by Makeev et al. [27] by adding some non-linear terms in BH theory, which physically signify the slope dependence of local erosion yield. BH theory also fails to predict one of the most observed experimental phenomena [7] i.e., non-zero critical angle (θ_c) for pattern formation, since it predicts pattern formation for arbitrary incident angles including normal incidence. Thus, an effort to find critical angle (θ_c) of pattern formation for present experimental condition is worthy to understand the ripple formation mechanism as its non-zero value overrides the description of BH theory. For this purpose, we have performed the irradiation at other incident angles i.e., 30°, 40°, and 50° also. Although, we found the initiation of ripple pattern formation started from 50° (AFM image of this sample is not shown), but well-defined periodic ripples evolved around 60°. So, the critical angle (θ_c) of ripple pattern formation for present experimental condition, i.e., 12 keV Ar⁺ ion irradiation on mica surface is found non-zero and can be considered around 50°.

The occurrence of smooth or flat surface below the critical angle of pattern formation was first explained by Carter and Vishnyakov [8]. Here, the projection of flux, contributed by the remaining atoms on surface displaced by the collision cascade, along the ion beam direction is considered to generate a curvature-dependent smoothing term. The wave number dependence of

which is found similar to the roughening term in the BH theory but in stabilizing manner, and therefore accounts smooth surface at near-normal incidence of ion irradiation. This mass redistribution phenomenon is reported later, experimentally by Madi et al. [174] and theoretically via molecular-dynamics simulations by Norris et al. [63] as dominant mechanism for the evolution of smooth surfaces at near normal incidences as well as also for parallel mode ripple pattern formation at low energy (~ 1 keV) ion regime. Recently, this is also found relevant for the subsequent rotated mode ripple formation at far grazing incidences [73]. In another recent report by Garcia et al. [50], this mass-redistribution effect is described as surface confined viscous flow (in mesoscopic scale) driven by ion-beam induced residual stress [64, 65, 177, 178] and is found again as major process behind pattern formation mechanism even in MeV ion range, reinforced by the ion-implantation effect rather than curvature dependent ion erosion. Their developed continuum model considers the effects of sputtering, mass redistribution, and ion implantation where the parameters are estimated under a binary-collision approximation. Binary collision mostly happens when the stopping power is ruled by the elastic contributions. This dominance is generally observed for the pattern formation by low-energy (\sim keV) ion bombardment and is true in the present case also. Thus, considering the continuum model given by Garcia et al. [50], the temporal evolution of height field $h(\vec{x}, \vec{y}, t)$ on substrate surface due to ion irradiation can be numerically approximated by the linear equation as

$$\frac{1}{J} \frac{\partial h}{\partial t} = C_{11} \frac{\partial^2 h}{\partial x^2} + C_{22} \frac{\partial^2 h}{\partial y^2} - \kappa \nabla^4 h \quad (5.1)$$

where J denotes ion flux, and K accounts the co-efficient for surface relaxation contribution such as thermally activated surface diffusion (TSD) [5], ion-enhanced viscous flow (IVF) [177, 179, 180] etc. From the literature, one can find the expressions of C_{11} and C_{22} details of which are

discussed later on. During oblique incidence ion irradiation ($\theta > \theta_c$), irrespective of the smoothing mechanism, the ripple alignment along the direction, x or y i.e., parallel or perpendicular to the ion beam direction, is determined by the coefficient C_{11} or C_{22} , which being negative has a larger absolute value [7, 102].

To have insight into the ripple formation mechanism, we now analyse the two coefficients C_{11} and C_{22} in detail [50], which relay the physical processes responsible for the pattern formation and can be expressed as

$$C_{ii} = C_{ii}^{\text{sputt}} + C_{ii}^{\text{CV}} + C_{ii}^{\text{impl}}, \quad i = 1, 2. \quad (5.2)$$

where the terms on the right-hand side of equation (2) correspond to sputtering [122, 181], mass redistribution [8, 66, 73, 174, 181], and ion implantation[93], respectively. To have an approximate quantitative idea [50], one can estimate $C_{ii}^{\text{sputt}} \approx Y_0 \Omega a_{\text{sputt}}$ [122, 181], $C_{ii}^{\text{CV}} \approx \Omega \delta$ [66, 174], and $C_{ii}^{\text{impl}} \approx \Omega \sigma_{\text{impl}} \mu_{\text{impl}} a_{\text{impl}}^{-1}$ [93] for present irradiation condition at normal incidence, where Y_0 is the average sputtering yield of a flat surface at normal incidence, Ω is the substrate atomic volume, a_{sputt} (a_{impl}) is the average depth for energy deposition (implantation), σ_{impl} (μ_{impl}) is the corresponding longitudinal (lateral) straggling length, and δ is the average travel distance of the recoil atoms. All the terms are estimated by TRIM calculation for the present experimental condition i.e., 12 keV Ar^+ ion irradiation on mica. The detailed values of all the terms, calculated from TRIM, have been discussed in the beginning of this section. We obtain the values of different contribution as $C_{ii}^{\text{sputt}} \approx 0.21 \text{ nm}^4$, $C_{ii}^{\text{CV}} \approx 0.576 \text{ nm}^4$, and $C_{ii}^{\text{impl}} \approx 0.048 \text{ nm}^4$ where one can clearly find the contribution of implantation is negligible. We have calculated C_{ii}^{sputt} , C_{ii}^{CV} , and C_{ii} for whole range of ion incidence angle, and plotted in Figures 5.2 (a) & (b). The negative value of C_{11} is found to be contributed by

C_{11}^{CV} , which signifies that the formation of parallel mode ripple pattern for present case of 12 keV ion bombardment is dominated by mass redistribution rather than ion erosion. The appearance of the critical angle (θ_c) of pattern formation is around 43° , which is close to our experimentally observed value 50° . Also, the observation of the appearance of x -direction ripples at 60° for all the ion fluences in our case indicates that $-C_{11}$ should dominate over than $-C_{22}$ at that particular incidence angle. This scenario i.e., the evolution of parallel mode ripples at oblique incidence on mica surface is found consistent with previous reports [170]. Metya et al. [34] observed parallel mode ripples by 500 eV Ar^+ ion irradiation on mica in the angle window $47\text{-}70^\circ$, whereas Buzio et al. [170] found it at an incidence angle of 35° by 1.04 keV Ar^+ ion sputtering. A comparison table about all work done on mica ripple is shown in Table 5.1.

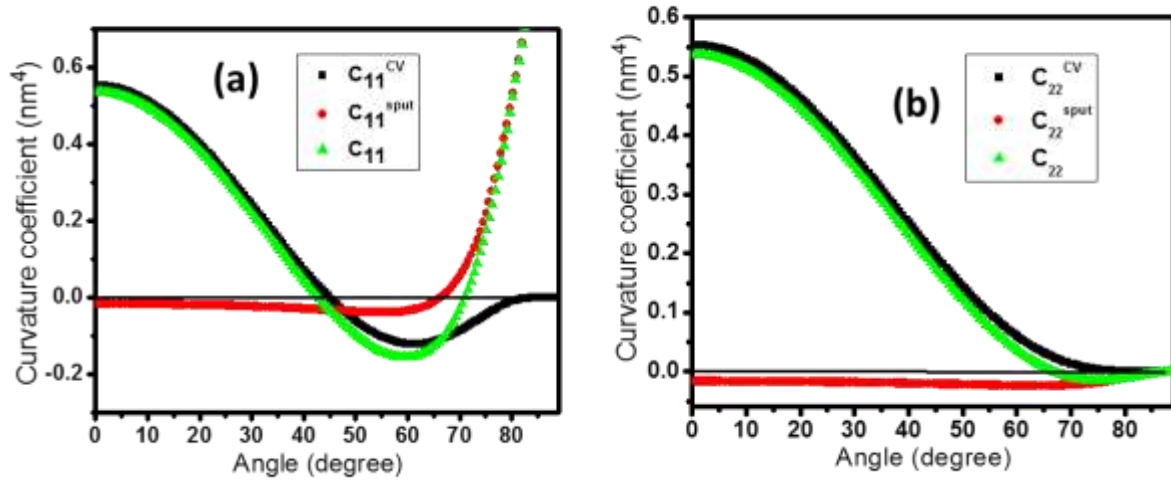


Figure 5.2: Dependence of (a) C_{11} and (b) C_{22} in Eq. (5.2) with ion incidence angle, using the parameters calculated from TRIM.

Table 5.1: Parallel mode ripple pattern on mica for different energy

Ion species	Angle of incidence (degree)	RMS roughness (nm)	Ripple wavelength (nm)	Ref.
25 eV Ar ⁺	40° – 70°	0.32 – 8.28	58.76 – 60.35	[173]
50 eV Ar ⁺	40° – 70°	1.22 – 5.08	32.84 – 59.17	[173]
100 eV Ar ⁺	40° – 70°	0.19 – 5.26	39.56 – 42.12	[173]
500 eV Ar ⁺	50° - 70°	0.1 – 1	25 – 35	[34]
1.04 keV Ar ⁺	35°	0.5 - 1.5	40 – 140	[170]
12 keV Ar ⁺	60°	7.06 – 12.58	120 – 165	present result

For deeper understanding of the dynamics of ripple formation in this energy regime (12 keV), the quantitative information of amplitude and wavelength is useful. The wavelengths (Λ) of the observed ripples are estimated from the position of first peak of their corresponding one-dimensional power spectral density measurements. The variation of wavelengths (Λ) with ion fluence is shown in Figure 5.3. For initial ion fluences up to 6×10^{17} ions.cm⁻², Λ is found to increase very slowly from 120 nm to 130 nm, and after that it shows a rapid coarsening with the exponent $n = 0.43 \pm 0.04$. The observed fluence independence of wavelength up to fluence 6×10^{17} ions.cm⁻² agrees with the linear behavior, whereas coarsening at sufficiently high fluence could be explained by the nonlinear behavior as described by Garcia et al. [175].

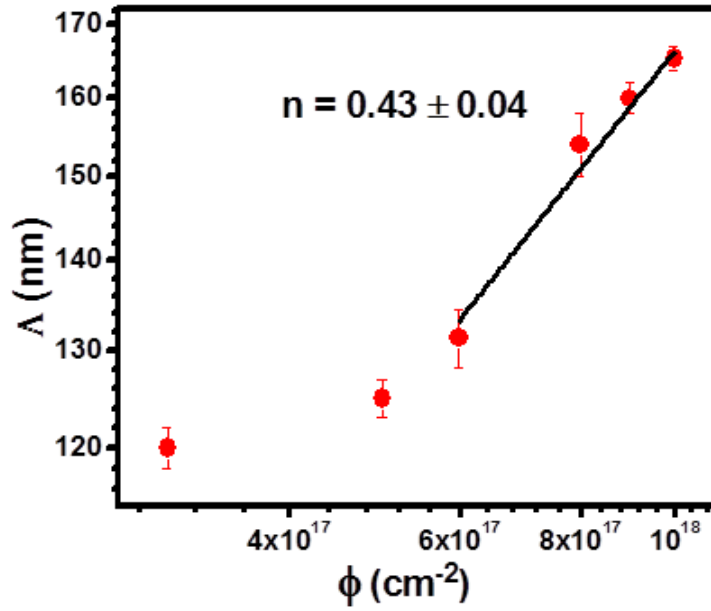


Figure 5.3: Log – log variation of ripple wavelength with ion fluence showing ripple coarsening at high fluence.

In order to get details of dynamic scaling behavior of ripple growth by ion beam induced erosion process, the rms roughness (W) and correlation length along the ripple wave vector direction (ξ_x) and perpendicular to the ripple wave vector (ξ_y) are extracted from the corresponding AFM images and are plotted in Figures 5.4 (a), (b), and (c), respectively. With the increase of ion fluence, the surface roughness is found to increase (Figure 5.4 a) with the growth exponent $\beta = 0.51 \pm 0.04$. This value of growth exponent is found nearly similar to the previously reported β value of the ripple growth on silica by 800 eV Ar^+ ion incidence at 60° [182]. The increasing nature of roughness with fluence indicates the roughening behavior of ripples. On the other hand, the correlation length along ripple wave vector direction shows monotonic increase with the dynamic exponent $(1/z_x) = 0.42 \pm 0.07$, which indicates the lateral growth of the ripple along the wave vector direction with ion fluence. Again, Figure 5.4 (c) shows the increase of perpendicular correlation length (ξ_y) with the dynamic exponent $(1/z_y) = 0.34 \pm 0.09$ with increase of ion fluence.

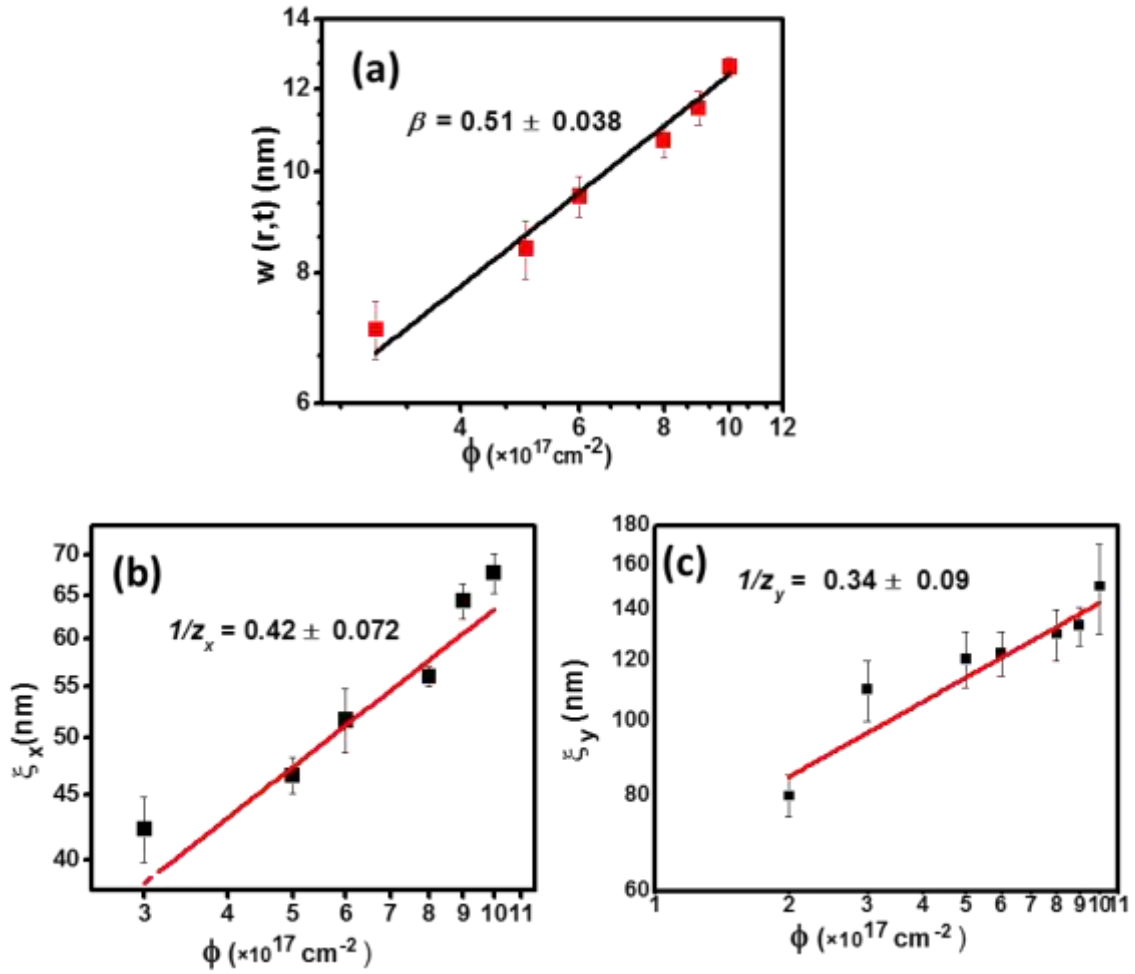


Figure 5.4: Variation of (a) interface width (rms roughness) with ion fluence, (b) correlation length along the ripple wave vector direction and (c) correlation length perpendicular to the ripple wave vector direction with ion fluence.

However, this increase is little slower than that of lateral correlation length. From the roughness variation (Figure 5.4a), it is clear that the morphology has not saturated even after high fluence. To quantify the competition between lateral and vertical growth, we have plotted W versus ξ_x for all the fluences, which is shown in Figure 5.5. From the scaling laws of W and ξ_x with fluence [110], one can easily derive the relation $W \sim \xi_x^\gamma$, where $\gamma = \beta/(1/z_x) = \alpha_x$. The value of γ is calculated from the linear fit of Figure 5.5, which is 1.22 ± 0.09 and found nearly equal to α_x (1.25) within error bar as found from the power spectral density. The observed value of $\gamma > 1$ indicates the faster vertical growth than its lateral growth i.e., surface roughening is dominating

the surface smoothening during the ion bombardment. Similar faster vertical growth was observed during the growth of cobalt phthalocyanine (CoPc) thin films on Si (001) surfaces with deposition time [100].

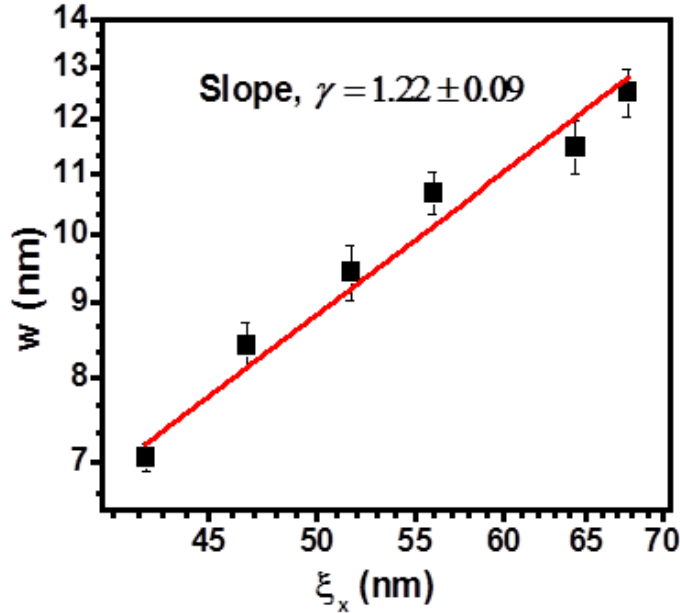


Figure 5.5: Log – log variation of interface width (W) with lateral correlation length (ξ_x).

In order to explore the further scaling behavior of the present system, the PSD functions for different ion fluences are calculated in the direction parallel $S_x(k_x)$ and normal $S_y(k_y)$ to the ion beam projection and are plotted in Figures 5.6 (a) and 5.6 (b), respectively. The structure factors $S_x(k_x)$ along the ion beam direction as shown in Figure 5.6 (a) show a peak in the curve at the spatial frequency k_x^* corresponding to the wavelength Λ of the ripple pattern about which we discussed earlier. For the large value of k_x i.e., $k_x \gg k_x^*$, all the curves tend to coincide and show power-law behavior $S(k_x) = k_x^{-(2\alpha_x+1)}$ with same slope $m_x = 3.5 \pm 0.42$. The peaks are shifted towards the lower k_x value with increasing fluence due to the ripple coarsening. For the case of structure factor $S_y(k_y)$ normal to the ion beam direction, the curves also coincide at larger value of k_y with slope value $m_y = 3.56 \pm 0.2$.

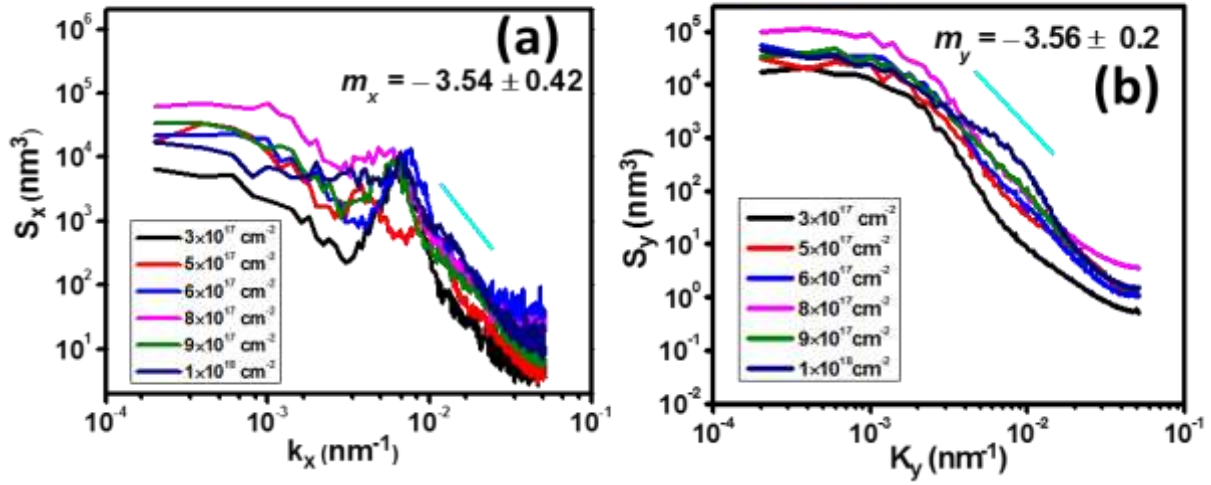


Figure 5.6: Structure factors $S_{x,y}(k_{x,y})$ in the direction (a) parallel and (b) normal to the ion beam for mica at different fluences.

The rescaled structure factors $S(k,t)k^{(2\alpha+1)}$ versus $kt^{1/z}$ for the different fluences are plotted as shown in Figures 5.7 (a) and 5.7 (b). All the curves collapse in a single line, and the average slope of the collapsed structure curves for low $k_{x,y}$ is found equal to $m_x = 3.5 \pm 0.18$ and $m_y = 3.4 \pm 0.16$ for the structure factor in the direction parallel and normal to the ion beam projection, respectively. From these slope, we find the roughness exponent along parallel and normal direction of ion beam, which are $\alpha_x = 1.25 \pm 0.09$ and $\alpha_y = 1.20 \pm 0.08$. Comparable result of roughness exponent was reported in the case of 16.7 keV O_2^+ bombardments at 60° on Si (100) surface [183]. A slight rounding of the structure factor for very high fluence (1×10^{18} ions.cm⁻²) is observed. This might be due to the non-saturation morphology [2]. Vivo et al. [110] introduced a term called degree of anisotropy ζ determined from the ratio of two roughness exponents α_x and α_y . In our case, ζ is found marginally greater than 1, which indicates the weak anisotropy of ripples. We have calculated the values of $\frac{\alpha_x}{z_x}$ and $\frac{\alpha_y}{z_y}$, which are found to be 0.52 and 0.40. Incidentally, these ratios are close to the β value 0.51 within the error limit obtained

from ion fluence vs. rms roughness plot (Fig. 5.4 (a)). This again proves the consistency of $z = \frac{\alpha}{\beta}$ relation.

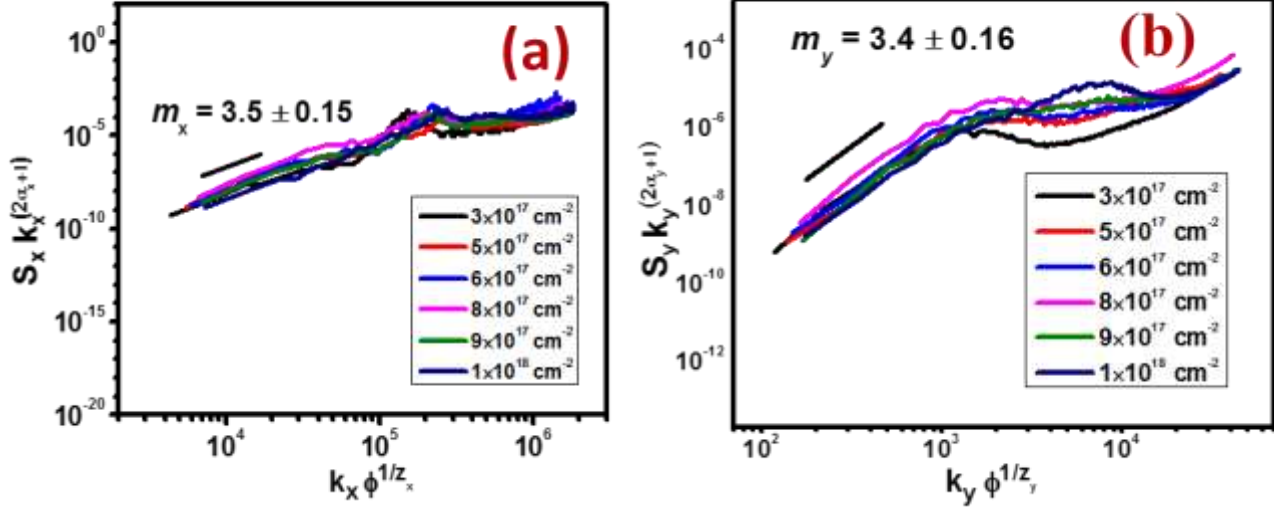


Figure 5.7: Collapsed structure factor curves using the values of z_x and z_y calculated from the slope of Figure 5.4 (b) & (c) in the direction (a) parallel and (b) normal to the ion beam for mica at different fluences.

To observe the pattern formation on mica by relatively lighter ion, we have bombarded the mica surfaces by 12 keV N^+ ion beam at the same oblique angle of incidence (60°) for three different fluences. The regular ripple patterns are observed (shown in Figure 5.8). The variation of rms roughness and ripple wavelength with ion fluences are also shown in Figures 5.8(d) and 5.8(e), respectively. Both the rms roughness and ripple wavelength increase with the ion fluences.

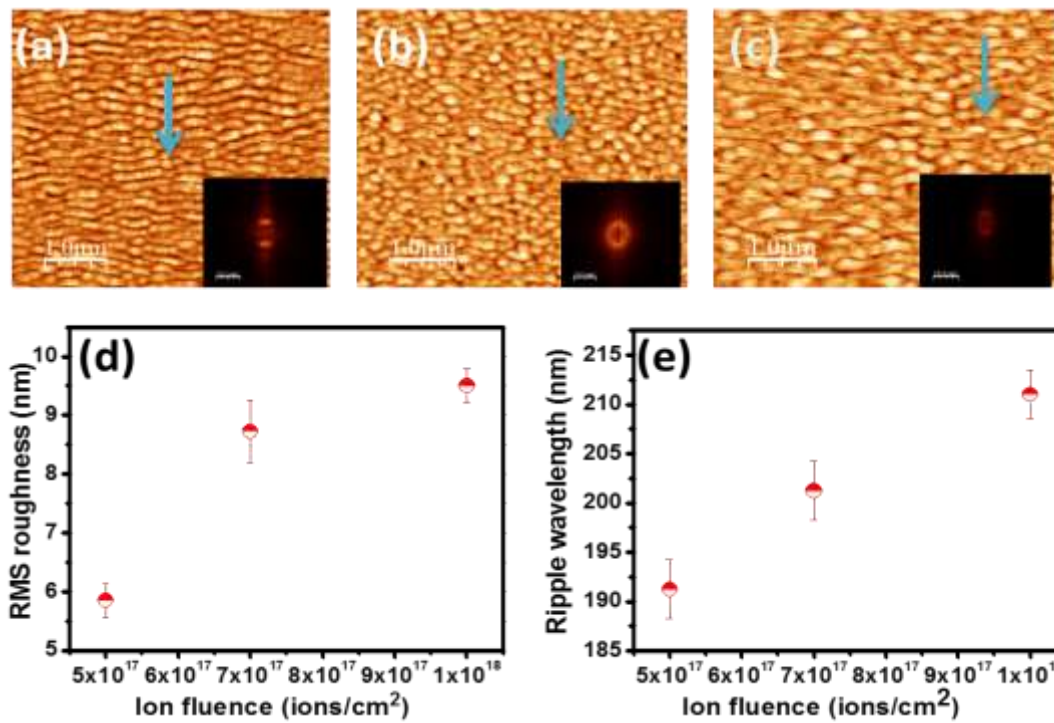


Figure 5.8: AFM images of oblique incidence 12 keV N^+ irradiated mica surfaces with fluence (a) 5×10^{17} , (b) 7×10^{17} , (c) 1×10^{18} ions. cm^{-2} . Variation of (d) roughness and (e) wavelength with ion fluence. The FFTs ($50 \mu m^{-1} \times 50 \mu m^{-1}$) are shown in the corner of each AFM images. The arrows indicate ion beam direction.

It is observed for both Ar and N bombardment that at higher fluence (Figs. 5.1 h and 5.8 b,c), the continuous ripples are broken and formed a pattern, which is a combination of dot and ripple. The preferential sputtering of mica like compound target leads to the enrichment of elements having lower sputtering yield. Our XPS measurement (Fig. 5.9), which is shown in the next section, illustrates the enrichment of Si and Al compared to K and O. Such ripple breaking at higher fluence may be due to higher enrichment of those elements. Instead of ripple, nanodot formation on oblique ion sputtered InP surface was reported earlier [184]. Further, relatively higher enrichment of Si is observed for nitrogen bombardment compared to argon. Therefore, we found breaking of ripple structure at earlier fluence for nitrogen bombardment (Fig 5.8), compared to Ar (Fig 5.1).

In conclusion, we have investigated morphological evolution of mica ripples during oblique incidence Ar^+ and N^+ ion sputtering for various ion fluences. Well-ordered parallel mode anisotropic ripples are observed above certain ion fluence. With continuous ion bombardment, the ripple wavelength and rms roughness increase with ion fluence. The formation mechanism of ripples on mica like compound surface is explained by recently advanced continuum models of ion beam sputtering, and the evolution dynamics is discussed in the context of dynamic scaling exponents. The competition between lateral and vertical growth of the ripples has also been highlighted, which will aid to produce wavelength and amplitude selected ripple structures on mica. TRIM estimation via the continuum model equation (5.1) demonstrates the competition among the curvature dependent sputtering, mass redistribution, and ion implantation. The evolution of ripples for ion fluence range is found to determine by mass redistribution effect rather than curvature dependent ion erosion instead of having apparently high sputter erosion of materials due to ion irradiation with energy 12 keV. The energy range for the present case also motivates for the future work on mica like other insulating substrate.

5.2 Hydrophobicity study and change of chemical nature on ion bombarded mica surfaces

In the previous section, we have discussed about the ripple pattern formation on mica surface by 12 keV Ar and N bombardment. In this section we will discuss about the chemical change of mica surface and the wettability due to ion bombardment. The surface chemical composition is investigated in terms of X-ray photoelectron Spectroscopy (XPS). The XPS of virgin and irradiated mica samples have been measured using an Omicron Multi-probe (Omicron Nano Technology, UK) ultrahigh vacuum (UHV) system (base pressure $\sim 5.0 \times 10^{-10}$ mbar). A

monochromatic Al K_{α} source is used to provide photons of energy 1486.6 eV for XPS measurement. The hydrophobicity is measured by water contact angle.

Figure 5.9 shows the schematic of crystalline mica structure, XPS spectra of virgin, 12 keV Ar^{+} , and N^{+} bombarded mica surfaces for ion fluence of 5×10^{17} ions/cm². The chemical composition of mica is $[KAl_2(Si_3Al)O_{10}(OH)_2]$. The X-ray photoelectron spectra (XPS) of cleaved virgin mica show the presence of all the elements (Fig. 5.9 b). Buzio [170] et al. and Bhattacharyya et al. [185] also showed the presence of all the elements on the virgin mica surface. Mica being a multilayered and multi-elemental compound, the chemical composition of mica is immensely changed due to keV ion bombardment. To observe the effect of post bombardment by lighter ions (N^{+}) and heavier ions (Ar^{+}), the XPS spectra of mica surface after the 12 keV Ar^{+} and N^{+} ion bombardment are recorded and also shown in Figure 5.9 (b). Different elements of the mica surface are eroded at different sputtering rate during the ion bombardment. The surface concentrations of all elements at atomic % for virgin as well as 12 keV N and Ar bombarded mica surfaces are shown in Figure 5.9 (c). We have calculated the sputtering yield of different elements of mica surface by the Monte Carlo code Transport of Ions in Matter (TRIM) considering the actual stoichiometric ratio of the elements (Figure 5.10). It is found that the sputtering yield of K, Si, and Al are almost same, whereas it is higher for O. It is found (Figure 5.9) that K is decreased to 1% from 5% for both N^{+} and Ar^{+} ion bombardment. This is because K atoms are arranged on the top of the surface of a freshly cleaved surface as well as stoichiometric ratio of K is minimum (1:21) (Figure 5.9 a). Metya et al. [34] also showed the large depletion of K even for low energy (500 eV) Ar^{+} ion bombardment on mica surface. Keller et al. [24] showed substantial erosion of K for only 25 eV Ar^{+} ion bombardment. In the present case, most of the K atoms from the upper surface are sputtered away due to higher energy (12 keV) ion

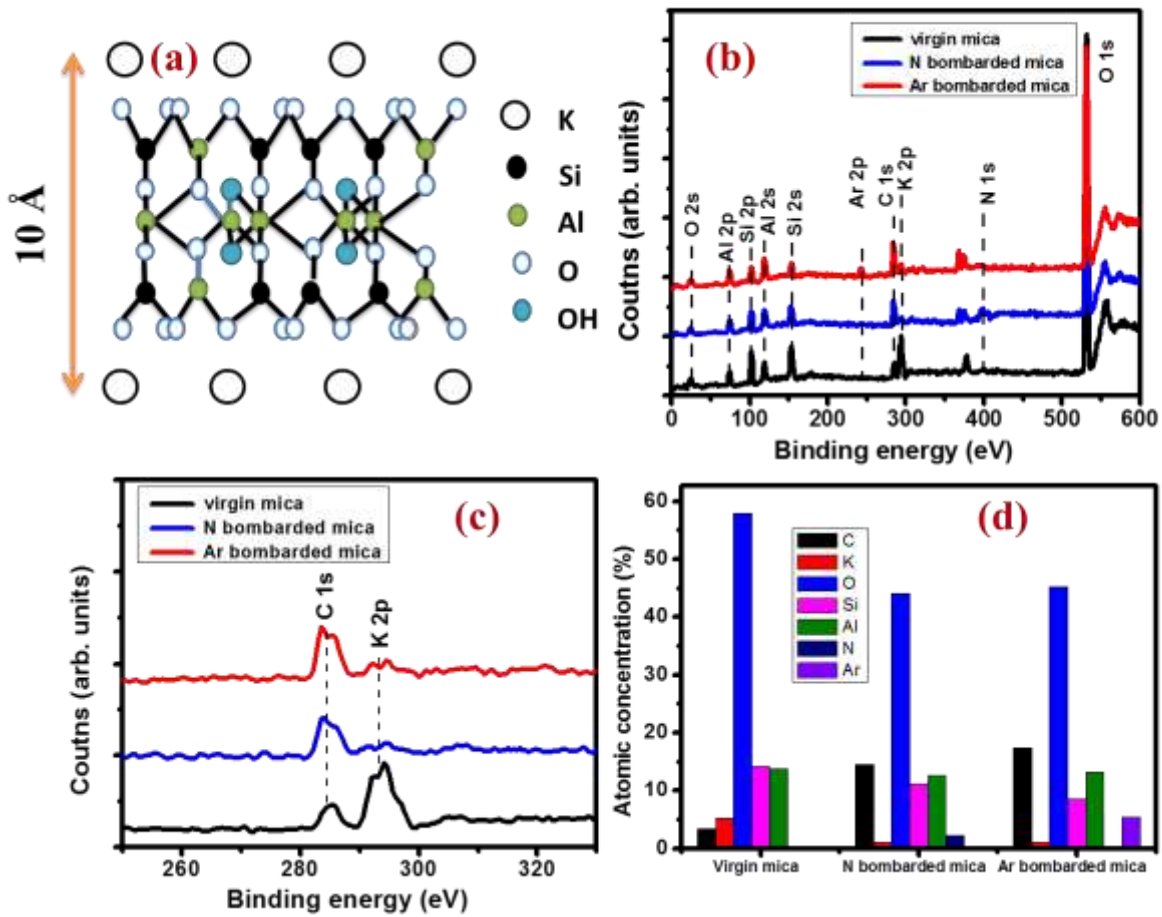


Figure 5.9: (a) Schematic diagram of crystalline mica. (b) X-ray Photoelectron Spectra (XPS) of virgin, 12 KeV N^+ and Ar^+ bombarded mica for ion fluence 5×10^{17} ions/cm². (c) XPS survey scan in C and K region. (d) Relative atomic concentrations in atomic percent (%) determined from XPS survey scan (Fig. 5.9b).

bombardment. The sputtering yield of Al and Si is almost same as of K (Figure 5.10), however because of higher stoichiometric ratio (3:21) in mica, relatively stronger peaks of both Al and Si are observed in the XPS spectra after 12 keV Ar^+ or N^+ ion bombardment (Figure 5.9). Although the sputtering of O is maximum, relatively intense O peak is observed for both the cases because of highest stoichiometry (12:21) of oxygen in mica. We observe a weak C peak (~3%) in virgin mica surface, whereas it is increased to 15 % and 18 % after N and Ar bombardment and subsequent air exposure, respectively. Increase of C peak in ion bombarded mica surface was

also observed before [24, 34, 170, 185]. This may be due to the large depletion of outermost K and consequent enhancement of C adsorption centers by the reactive aluminosilicate. This results in an adsorption of large amounts of hydrocarbons (HCs) from the environment. Similar enhanced reactivity and adsorption of HCs were also shown for sub-eV ion bombardment [24]. In case of Ar^+ bombardment, the Ar peak is observed in XPS spectra (Figure 5.9 b). This indicates that the Ar atoms are being trapped in the mica surface. Similarly, N peak is also observed for N^+ bombarded mica, but the peak intensity is less because of deeper implantation of lighter N ion in the mica.

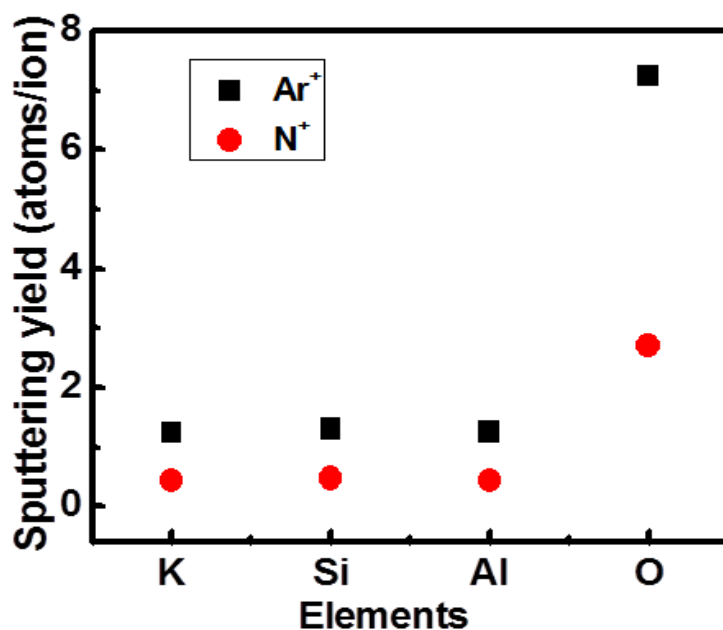


Figure 5.10: Sputtering yield calculation (TRIM) of different elements of mica for 12 keV Ar^+ and N^+ ions bombardment at oblique angle (60°).

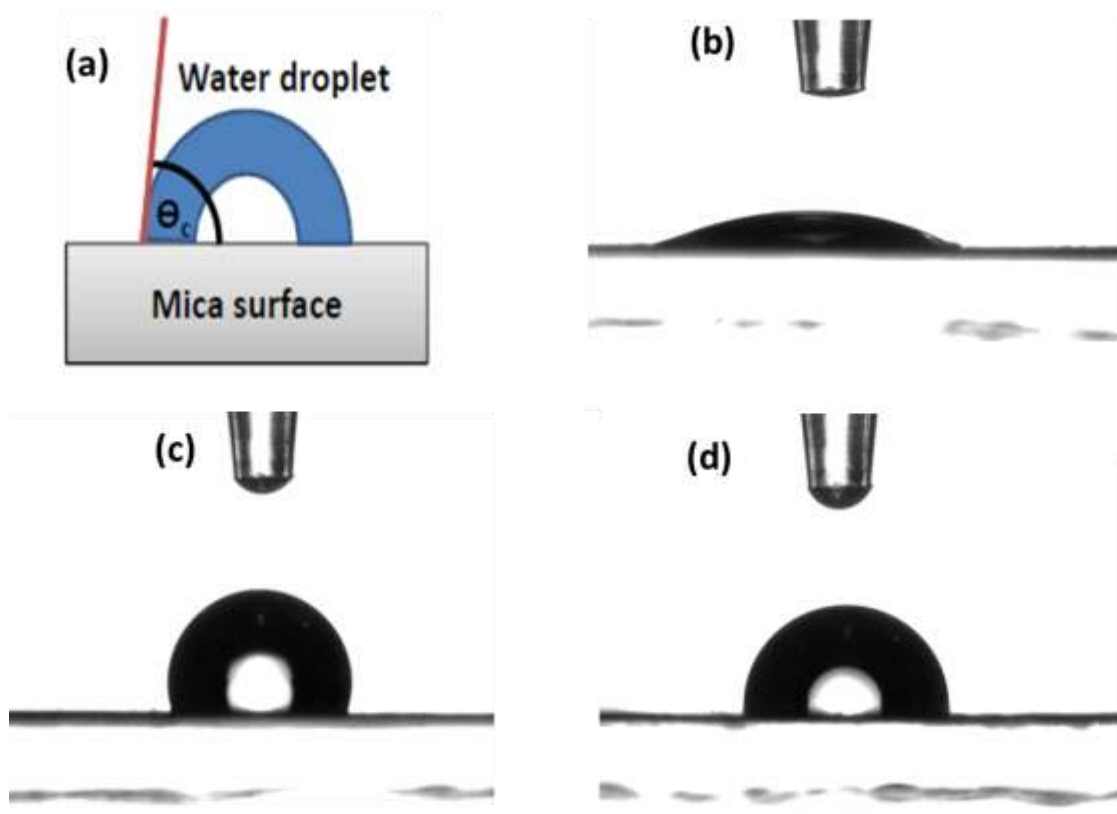


Figure 5.11: (a) Schematic diagram of contact angle measurement. Droplets of water on (b) virgin mica surface, (c) 12 keV Ar^+ irradiated mica with fluence 3×10^{17} ions/cm² and (d) 12 keV N^+ irradiated mica surface with fluence 1×10^{18} ions/cm².

Ion bombardment induced physicochemical changes modify the wetting properties of mica surface. Figure 5.11 shows the contact angle measurements of virgin and ion beam modified mica surfaces. The schematic diagram of contact angle measurement is shown in Figure 5.11 (a). The images of the water droplets on virgin, Ar^+ and N^+ ions bombarded mica surfaces are shown in the Figures 5.11 (b), (c), and (d), respectively

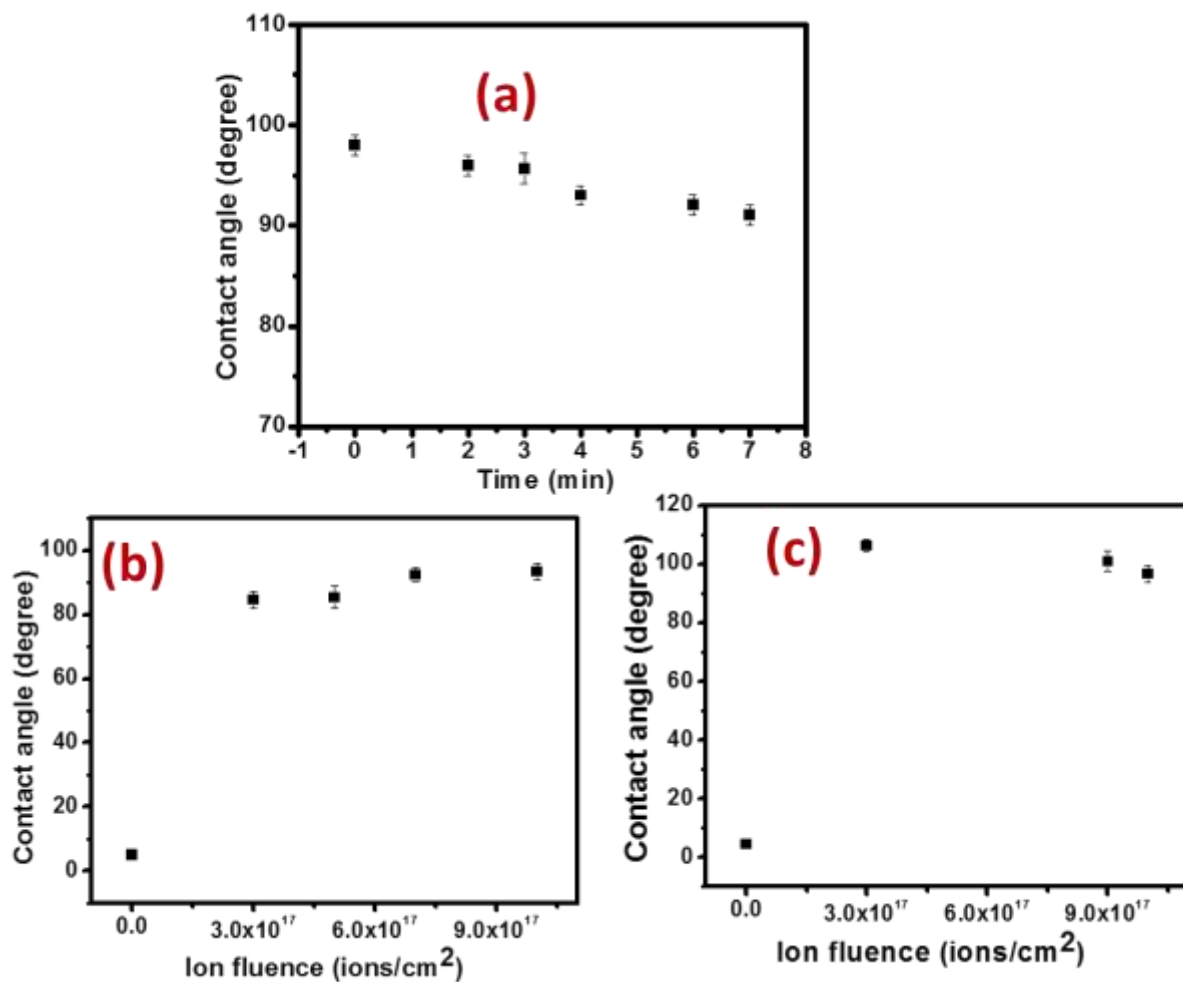


Figure 5.12: (a) Contact angle measurement with time for 12 keV Ar^+ bombarded mica surface (fluence 9×10^{17} ions/cm²). Contact angle variation with ion fluence for (b) 12 keV N^+ bombarded and (c) 12 keV Ar^+ bombarded mica surfaces.

The contact angle for each surface has been recorded after the stabilization of the water droplet. It is shown in Figure 5.12 (a) that the surface and droplet contact angle is stabilized approximately after 5 minutes. The variation of contact angle with ion fluence for 12 keV N^+ and Ar^+ ion irradiated mica surfaces are shown in Figure 5.12 (b) and (c), respectively. The hydrophilic virgin mica shows the contact angle $\sim 5^\circ$. It is found that the contact angle increases significantly at the initial stage of ion (N^+ or Ar^+) bombardment. The contact angle jumps to 82°

for N^+ ions at fluence of 5×10^{17} ions/cm². For continuous ion bombardment, the contact angle increases slowly up to 91° (Figure 5.12 b). In case of Ar^+ ion bombardment, the contact angle reaches to 104° at the lowest ion fluence (3×10^{17} ions/cm²) and then slowly decreases to 94° with the increase of ion fluence.

N^+ and Ar^+ ion bombardment induced hydrophilic to hydrophobic change of mica surface is due to the chemical as well as physical change. The chemistry of the mica surface is modified due to the different sputtering rate of the elements on the surface. Consequently, the physical structure is also changed on the surface. With continuous ion bombardment, the ripple like structure is formed on the surface. It was shown that the surface roughness of the microstructure has a great influence on hydrophobicity [153], textured and rough surface shows water repelling behavior like plant surfaces (lotus leaves). However, ion beam induced nano scale morphological change is less effective than the surface chemical change to alter the wetting properties of mica surface. In a crystalline bulk mica (Figure 5.9 a), negatively charged alumino silicate layers are interconnected by positively charged K^+ ions. During cleaving alumino silicate layers are separated due to weak ionic bonding via K^+ ions. The negative charge of the aluminosilicate layer is due to the replacement of one of four Si^{4+} by a Al^{3+} ions. The layer of K is shared by two cleaved surface, therefore, cleaved surface is expected to be covered by half mono layers of K, which compensate the negative charge of the aluminosilicate layer [186]. However, K^+ ions are weakly bound and are also not ordered in a specific structure. The depletion and dis-orderness of K^+ ions on the surface become the decisive parameter for absorption of carbogeous gas from the atmosphere and thereby wetting properties of the surface. Any depletion of K^+ ions makes the underlying aluminosilicate layer charged and centers for C adsorption from the atmosphere to form hydrocarbon (HC) layer by reacting carbonaceous gases (CO , CO_2) with water [187,

188]. The C adsorption on the mica surface leads to decrease the surface energy [1], and thereby increases the contact angle with water droplet. 12 keV N^+ or Ar^+ ion bombardment on mica removes most of the K atoms at very initial stage (minimum ion fluence) of ion bombardment as well as amorphise the mica surface. Therefore, mica surface with depleted K top layer becomes drastically hydrophobic when exposed to air (Figs. 5.11 & 5.12). To remove only the top K layers, bombardment with lower energy and low fluence is also sufficient [24, 172]. The slow increase of contact angle with N^+ ion fluence (Fig. 5.12 b) indicates that keV energy ions not only remove the top K but also lead to damage creation and intermixing of other constituents. The broken Al-O and Si-O bonds may also form active sites for hydrocarbon absorption. Therefore, a large number of chemically active Al and Si centers are created on the mica surface that adsorbs C elements from environment. The C adsorption on mica surface after bombardment is also reflected in XPS spectra (Fig. 5.9). Similar study of compositional change of mica surface due to RF plasma etching was also reported by Liu and Brown [158].

In case of Ar^+ ion bombardment the maximum (94°) is reached at minimum ion fluence (3×10^{17} ions/cm²). Bombardment with Ar^+ like heavier projectiles makes the surface more hydrophobic than N^+ like lighter projectiles. This is also consistent with XPS measurement of C peak; the adsorbed C is higher in case of Ar^+ ion bombardment (Figure 5.9 c). Being the heavier projectile, Ar^+ ions remove most of the K atoms from the top layer as well as create sufficient disorder in the aluminosilicate at minimum fluence. However, due to higher sputtering rate by Ar^+ ions, continuous bombardment exposes the next layer of mica where active sites are slightly less, therefore, shows slight decrease of contact angle with Ar^+ ion fluence (Fig. 5.12 c). Further, observed lower contact angle for N bombardment on mica may be due to the implantation of reactive nitrogen and consequent nitridation. Wan et al. [156] reported decrease of contact angle

due to formation of Si-N bond during nitrogen plasma implantation on Si wafer. In the present case, Si-N formation may be one of the reasons of lower contact angle compared to Ar bombardment. However, higher energy and higher fluence ion induced enhancement of contact angle of mica surface is mostly due to ion induced active site creation and consequent hydrocarbon adsorption.

In summary, energetic (12 keV) N^+ and Ar^+ ions can significantly modify the chemical nature of virgin mica surface and also develop regular ripple nanopattern by oblique angle bombardment. This physicochemical modification converts the super hydrophilic mica surface to a hydrophobic surface. Bombardment with keV energy ions erode the top K layer as well as break the bonds in the aluminosilicate layer. Therefore, hydrophobicity could be better controlled by keV energy ion beams. Further, heavier ions bombardment leads to substantial damage as well as erodes layers of mica due to higher sputtering yield compared to lighter ions. Chemically modified and nano-patterened mica like insulating surface might be used as a template for the synthesis of self-organized arrays of nanowires [164, 165] and for the biological deposition like protein folding [189].

5.3 Detailed investigation of surface chemical nature of virgin and ion beam modified muscovite mica surface

Mica is a very important substrate for the modification, the details of which are already discussed in the previous section. Here, we have studied in detail the chemical changes of virgin mica surface by the X-ray photoelectron spectroscopy (XPS) after Ar and N bombardment. We have already discussed in the previous section that energetic (keV) ion bombardment preferentially sputters the upper K atoms; as a result, more hydrocarbons are adsorbed on ion bombarded mica

surfaces compared to its virgin when the surface is exposed to the ambient atmosphere. In this section, we will mainly discuss how the chemical phase of different elements in mica change due to ion bombardment. The adsorbed carbons react with the Si and form silicon carbide (SiC) for both Ar and N bombarded mica surfaces. Due to the reactive nature of N, silicon nitride and aluminum nitride are also formed during N^+ ion bombardment.

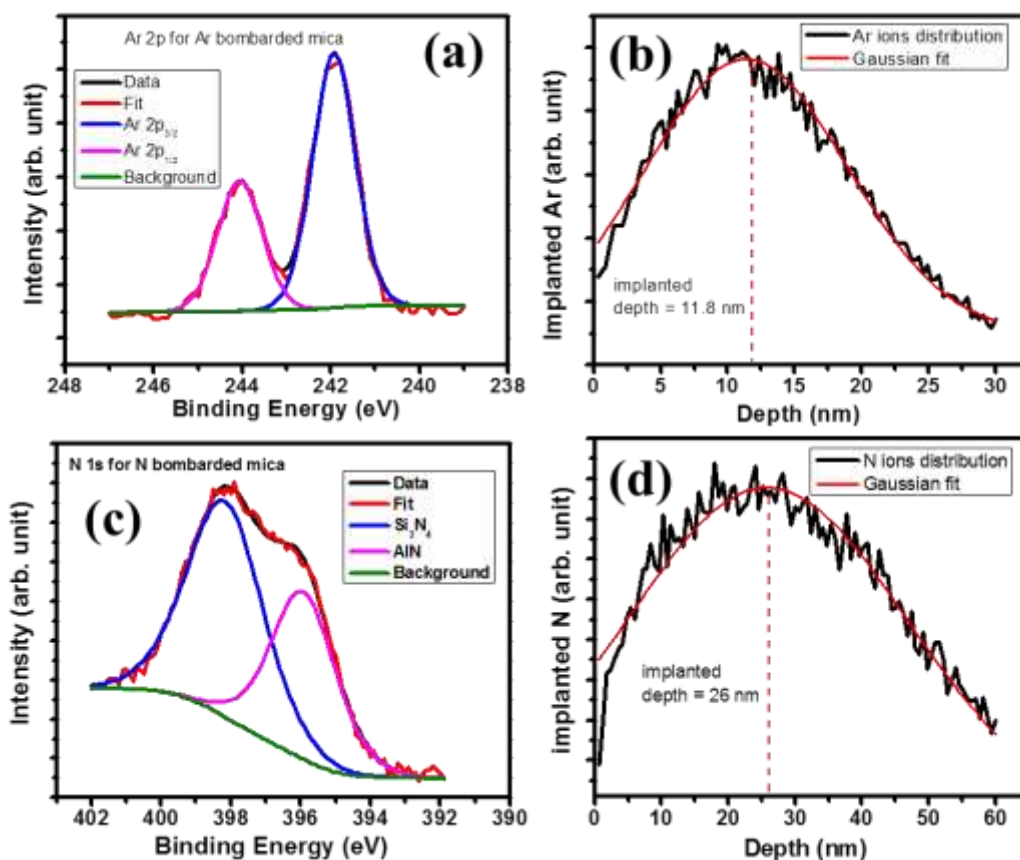


Figure 5.13: (a) High resolution XPS spectrum of Ar 2p for Ar bombarded mica, (b) 12 keV Ar ions distribution in mica calculated by TRIM. (c) N 1s core level XPS spectrum showing Si_3N_4 and AlN formation for N bombarded mica and (d) 12 keV N ions distribution in mica calculated by TRIM.

The XPS survey scan of virgin and ion bombarded mica was already shown and discussed in Figure 5.9. To investigate the presence and role of implanted Ar in mica, we recorded the high-resolution XPS spectrum of Ar 2p (Figure 5.13 a). The Ar 2p spectrum can be well fitted by two Gaussian-Lorentzian peaks one at 241.94 eV and another at 244.04 eV corresponding to Ar 2p_{3/2} and Ar 2p_{1/2}, respectively. The Ar 2p_{3/2} and Ar 2p_{1/2} are resolved with energy separation of 2.1 eV, which indicates the inertness of Ar ions in mica. An approximate distribution of Ar atoms in the mica is calculated by TRIM, which shows a penetration depth of 11.8 nm (Fig. 5.13 (b)).

The Ar atoms are generally trapped in the interstitial sites for implantation at low energy [190]. Similarly, to observe the influence of implanted N atoms in mica, XPS spectrum of N 1s core level is recorded for N bombarded mica surface (Fig. 5.13 c). N 1s spectrum is fitted by two Gaussian-Lorentzian peaks, one at 398.3 eV and another at 395.98 eV corresponding to Si₃N₄ and AlN, respectively. Also, the N atoms distribution in mica is shown in Figure 5.13 (d). N ions penetrate upto 26 nm, and it reacts with Si and Al by breaking of the Si-O, Al-O bonds in the aluminosilicate layer. The breaking of Si-O and Al-O bonds in the aluminosilicate layer was also previously shown after plasma treatment on mica [158]. TRIM calculations present that the mica surface is modified up to 30 nm for Ar and 60 nm for N, respectively, however sputtering loss of the top surface and chemical changes of mica due to Ar or N ion bombardment are not considered in TRIM calculation.

With continuous bombardment, the mica surface is readily amorphized, and the energetic ions modify the aluminosilicate layer. We have recorded the high-resolution core level XPS spectra of Si 2p, and Al 2p for the virgin and ion bombarded mica surfaces, which are shown in Figure 5.14. Figure 5.14 (a) displays Si 2p spectrum for virgin mica, which can be fitted by two

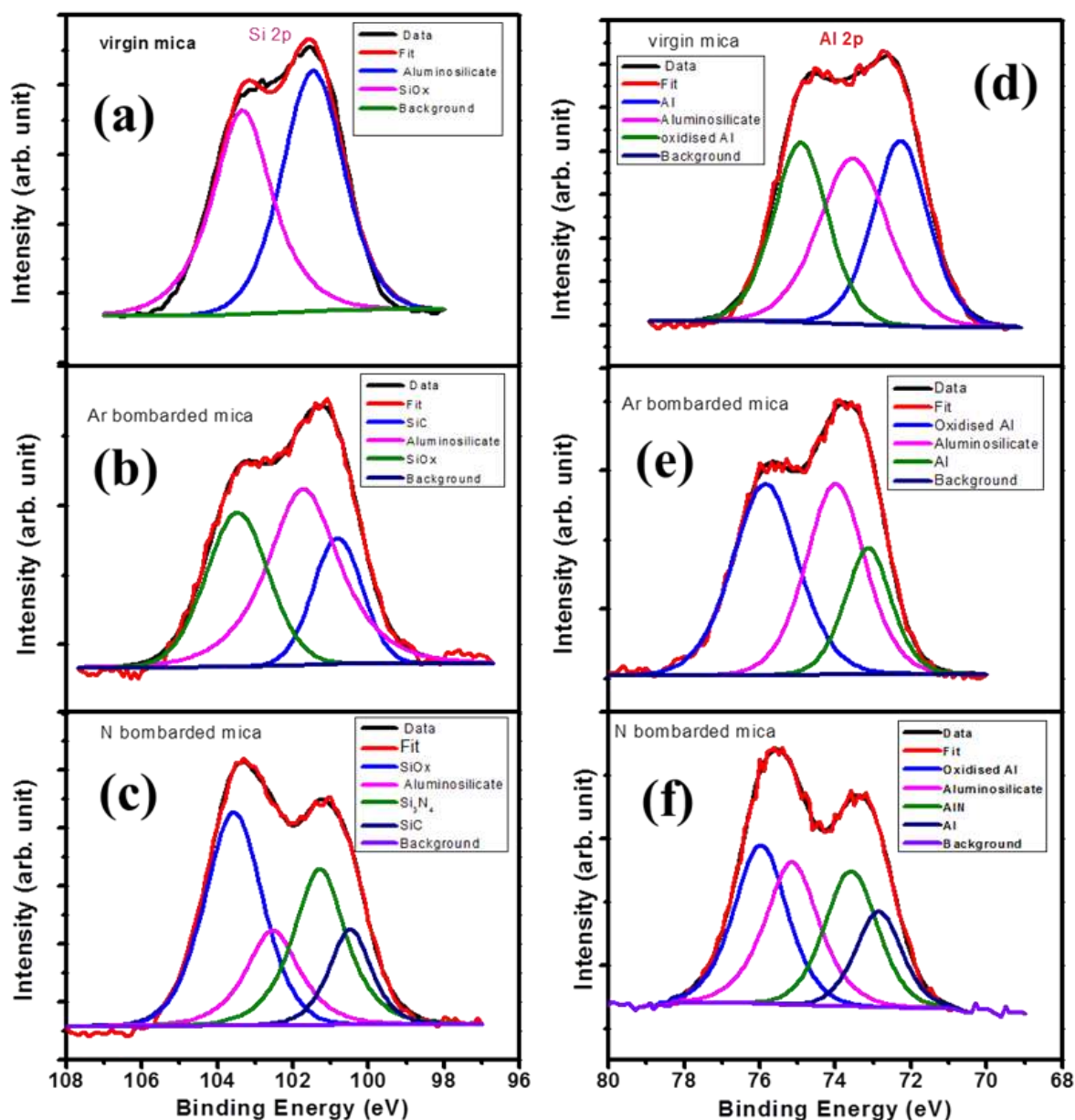


Figure 5.14 : High resolution XPS spectra of Si 2p and Al 2p for (a) & (d) virgin mica, (b) & (e) 12 keV Ar bombarded mica and (c) & (f) 12 keV N bombarded mica respectively.

Gaussian-Lorentzian peaks, one at $E_b=101.45$ eV and another at $E_b=103.34$ eV corresponding to aluminosilicate and SiO_x , respectively. Similarly, for Ar and N bombarded mica, Si 2p spectra as shown in Figures 5.14 (b) & (c) can be best fitted by three and four Gaussian-Lorentzian peaks, respectively. For Ar bombarded mica surface, SiC is observed to form in addition of the

aluminosilicate and SiO_x . However, for N bombarded surface silicon nitride (Si_3N_4) is also formed due to reactive N beam. We have already observed Si_3N_4 formation in N 1s spectrum (Fig. 5.13). Si_3N_4 is generally formed by N ion beam on Si surface [41, 71, 150]. The binding energies of all compounds of Si in mica before and after ion bombardment are given in Table 5.2 along with some reported values in the literature to compare our results.

Table 5.2: Some reported binding energies (eV) of Si 2p and their compounds along with the present experimental value.

Aluminosilicate/silicate	SiC	Si_3N_4	SiO_x	Ref.
101.4 – 102.4				[159]
	100.3			[191]
		101.3	102.5	[192]
		101.8	103.7	[193]
102	100.4	101.3	103.56	Present work
± 0.5	± 0.4		± 0.2	

Al 2p core level XPS spectra for virgin, as well as Ar and N bombarded mica surfaces are shown in Figures 5.14 (d)-(f). Al 2p spectra can be best fitted by three Gaussian-Lorentzian peaks corresponding to elemental Al, aluminosilicate, and oxidized Al for virgin and Ar bombarded surfaces. For Ar bombardment, the intensity of elemental Al decreases, whereas the intensities of aluminosilicate and aluminum oxide decrease slightly compared to the virgin mica. For N bombarded mica surface, an additional aluminum nitride (AlN) is found to form. AlN formation is also evident in N 1s spectrum (Fig. 5.13). The binding energies of the entire compound in Figure 5.14 (c) – (f) and some reported values from literature are shown in Table 5.3.

Table 5.3: Some reported binding energies (eV) of Al 2p and their compounds along with the present experimental value.

Al	Aluminosilicate/silicate	AlN	oxidized Al	Ref.
72.8		73.9		[194]
			75.9	[195]
	73.6/74.71	73.5	74.8	[195-197]
72.9	74	73.6	75.3	Present work
± 0.2	± 0.5		± 0.5	

The large depletion of positively charged K ions of the top layer of the mica surface by ion bombardment leads to adsorb hydrocarbon when the surface is exposed in the ambient atmosphere. The K depletion and C adsorption on mica after ion bombardment were also

previously observed [24, 34, 170]. The high-resolution XPS core level spectra of C 1s for virgin, as well as Ar and N bombarded mica are shown in Figures 5.15 (a)-(c). The deconvolution of C 1s peak is also shown in Figure 5.15 (a), which reveals that the observed single C 1s peak at binding energy $E_b \sim 285$ eV in the virgin mica corresponds to the elemental carbon. These

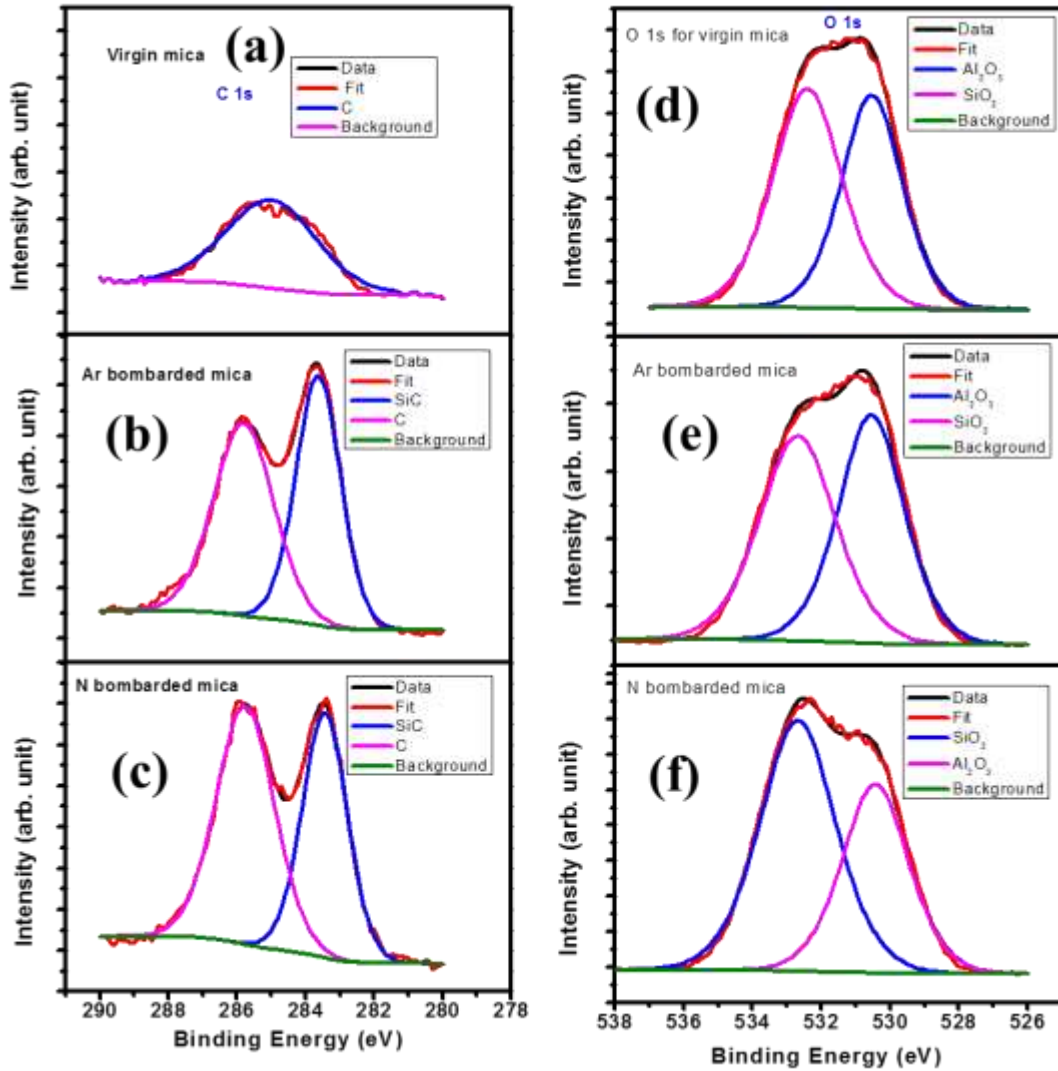


Figure 5.15: High resolution XPS spectra of C 1s and O 1s for (a) & (d) virgin mica, (b) & (e) 12 keV Ar bombarded mica and (c) & (f) 12 keV N bombarded mica respectively.

carbons come from the adventitious hydrocarbon contamination or adsorption from the surrounding, but for the Ar and N bombarded mica surfaces, C 1s core level spectra are well fitted by two peaks corresponding to C ($E_b \sim 285.8$ eV) and SiC ($E_b \sim 283.5$ eV), respectively. The shift of binding energy for carbon in case of ion bombarded mica may be due to partial oxidation of carbon [158]. SiC is formed by C adsorption and reaction with the Si in the aluminosilicate layer where some of the Si-O bonds are broken by ion bombardment.

We have previously observed SiC formation due to C ion implantation [40, 71], but in the present case, SiC formation process is quite different. Further, we have observed the O 1s core level spectra for both virgin and ion bombarded mica surfaces. The O 1s core level spectra are shown in Figures 5.15 (d) – (f), which show that in all cases O 1s is well fitted by two Gaussian-Lorentzian peaks, one at 532.4 ± 0.2 eV and another at 530.5 ± 0.1 eV corresponding to SiO₂ and Al₂O₃, respectively. In virgin mica, the peak intensities corresponding to SiO₂ and Al₂O₃ are almost same, whereas for ion bombarded mica, they are different. This is due to the sputtering of O atoms during ion bombardment. The binding energy of C 1s, O 1s, and N 1s for different compounds along with the reported values in the literature are shown in Table 5.4.

Table 5.4: Some reported binding energies (eV) of C 1s, N 1s, O 1s and their compound along with the present experimental value.

C region		O region		N region		Ref.
SiC	C	SiO ₂	Al ₂ O ₃	Si ₃ N ₄	AlN	
283.3	285.4	532.7	530.3	398.2	396.2	[191, 198-201]

283.2	284.8	532.5	530.7	397.8	396.4	[190, 196, 202-204]
283.4	285.4	532.4	530.5	398.3	395.98	Present work
± 0.2	± 0.4	± 0.2	± 0.1			

In summary, we have proposed the surface chemical treatment of mica surface by low energy inert and reactive ion bombardment. Detailed studies of the surface composition and the chemical states of the elements of freshly cleaved as well as ion bombardment mica surfaces by x-ray photoelectron spectroscopy (XPS) show that sputtering and ion implantation can be used to precisely control the chemical nature of the mica-like naturally available multilayered multicomponent surface. Depletion of K layer due to preferential sputtering opens active adsorption sites. Further, chemically reactive projectile ions (N) react with the aluminosilicate layer and modify by creating silicon nitride and aluminum nitride. It is also found that the chemisorption of C on ion beam modified mica surface forms SiC. Our results will motivate to tune the chemistry of mica surface by low energy ion bombardment and study the interaction of biomolecules with modified mica surface.

Chapter 6

6.1 Role of impurity in low energy Ar^+ ion beam on Si ripple pattern formation

The pattern formation on Si surface by energetic ion bombardment has brought a great interest in the scientific research for its potential applications. Several experimental observations of ripple pattern formation have been reported on the Si surface by varying ion species, energy (250 eV - 1 keV), and incident angles [17, 33, 106, 121, 174, 205-208]. As the Ar ion beam is very common for surface cleaning and depth profiling in surface science experiments, several groups have reported pattern formation on Si surface by very low energy Ar^+ ion (500 eV to 2 keV) bombardment [16, 17, 106, 121, 171, 174, 206-210]. However, the study is limited in the medium energy range 3 – 100 keV [8, 30, 40, 211-222], because a limited ion beam facility in this energy regime is used for nanopatterning. It is also interesting that the well defined pattern on Si is observed only for mass analyzed Ar^+ ion energy greater than 20 keV [30, 214-222], ripple pattern is not found in the energy range 3-20 keV [8, 10, 40, 211-213].

For very low energy (100 eV to 2 keV) Ar^+ ion beam, ion guns are generally attached to the vacuum chambers without the mass filtering system, whereas in typical ion implanter the energy is above 3 keV, and the beam is usually mass analyzed and isotopically pure. The unfiltered ion beam may contain N, C, O, and other common impurities. Pan et al. [190] observed silicon carbide (SiC) formation in an ultra-high vacuum chamber by low energy (1.5 keV) Ar^+ ion incorporation, although they did not study the pattern formation and role of contamination induced chemical effects on the pattern formation. Ozyadin et al. [28, 29] found that Si surface remained flat for normal incidence ion bombardment, but a disordered array of

nanodots was developed for co-deposition of trace amount of Mo atoms during bombardment. Ziberi et al. also admitted that the dot pattern formation by noble ion bombardment might be due to the unintentional contaminations from the various sources [16-19]. Hofsass and Engler pointed out the effect of contamination on pattern formation, where the contamination came from the target holder or were intentionally incorporated during ion bombardment [20-22]. Moon et al. [23] also observed the surface nanopatterning of Si targets irradiated with 2 keV Ar^+ ions under the concurrent Au impurity co-deposition from a gold target. Bradley gave several theories on pattern formation with external co-deposition of impurities [90-93]. Nevertheless, the contaminations in ion beam itself and consequent effects on nanopatterning have been overlooked.

In this chapter, we have investigated the pattern formation on Si by the mass analyzed pure and unanalyzed impure 3- 10 keV Ar ion beam and explored the role of beam impurities on Si ripple formation. It is established that if ion beam is not mass filtered, a mixture of ions bombards the surface, and the reactive species play the vital role for ripple formation.

The experimental details have already been discussed in the previous chapters. We have used 99.99% pure Ar gas to produce the Ar^+ beam in the ECR ion source. A small gas capsule in a gas manifold system was filled with the pure gas from an argon gas cylinder. The Ar gas is introduced to the ECR ion source from the capsule through a precisely controlled leak valve. Mixing of a trace amount of nitrogen and oxygen from the air during the transfer is unavoidable. The irradiation was carried out in two different ways one before the dipole magnet i.e., by mass unanalyzed ion beam and another after the dipole magnet, i.e., by mass analyzed ion beam. The schematic diagram of the irradiation experimental set up has already been shown in Figure 3.1 (Chapter 3). The morphologies of all the irradiated samples were investigated by AFM, whereas

the compositional change of the irradiated Si (100) samples with respect to virgin Si surface was investigated by X-ray photoelectron spectroscopy (XPS) as discussed in the previous chapter.

Figure 6.1 shows the surface morphologies of mass analyzed Ar^+ ion-bombarded Si surfaces with different ion energies. Figures 6.1 (a) – (d) show the AFM images of 3 – 10 keV Ar^+ ion-bombarded Si surfaces with ion fluence 7×10^{17} ions/cm² at an angle of incidence 60° with the surface normal. The irradiated surfaces amorphize after the irradiation and do not show any pattern, but a rough surface with rms roughness below 1 nm is observed as shown in Figure 6.1 (e). The absence of the pattern on Si surface by low energy (3-10 keV) mass analyzed Ar^+ ion bombardment at oblique angle was also reported earlier [10, 40]. However, the patterns are easily observed by other groups at lower energies (< 2 keV) [17, 33, 106, 121, 174, 205-208]. Ziberi et al. reported the ripple pattern formation on Si by noble gas ion beam (Ar^+ , Kr^+ , Xe^+) below 2 keV ion energy, but observed no pattern by Ne^+ ion beam [17]. They concluded that the mass of ion played a vital role in pattern formation. The description of mass dependence cannot explain the pattern formation by N, O & C ions and the absence of pattern by Ar ion of same energy (3-10 keV) [41]. It is observed that the kinematics of the Ar^+ ion with Si surface is not very much different for ion energy 1.3 to 10 keV [10]. Thus, the pattern formation by ion bombardment depends not only on the kinematics but also on the additional sources of instability i.e., initial perturbation [70], presence of surfactant [20], and external impurities [23]. One of the most possible sources of impurities could be the ion beam itself if it is not filtered properly. To examine the source of impurity, the chemistry of mass filtered and unfiltered Ar^+ ion-bombarded Si surfaces is investigated by X-ray Photoelectron Spectroscopy (XPS).

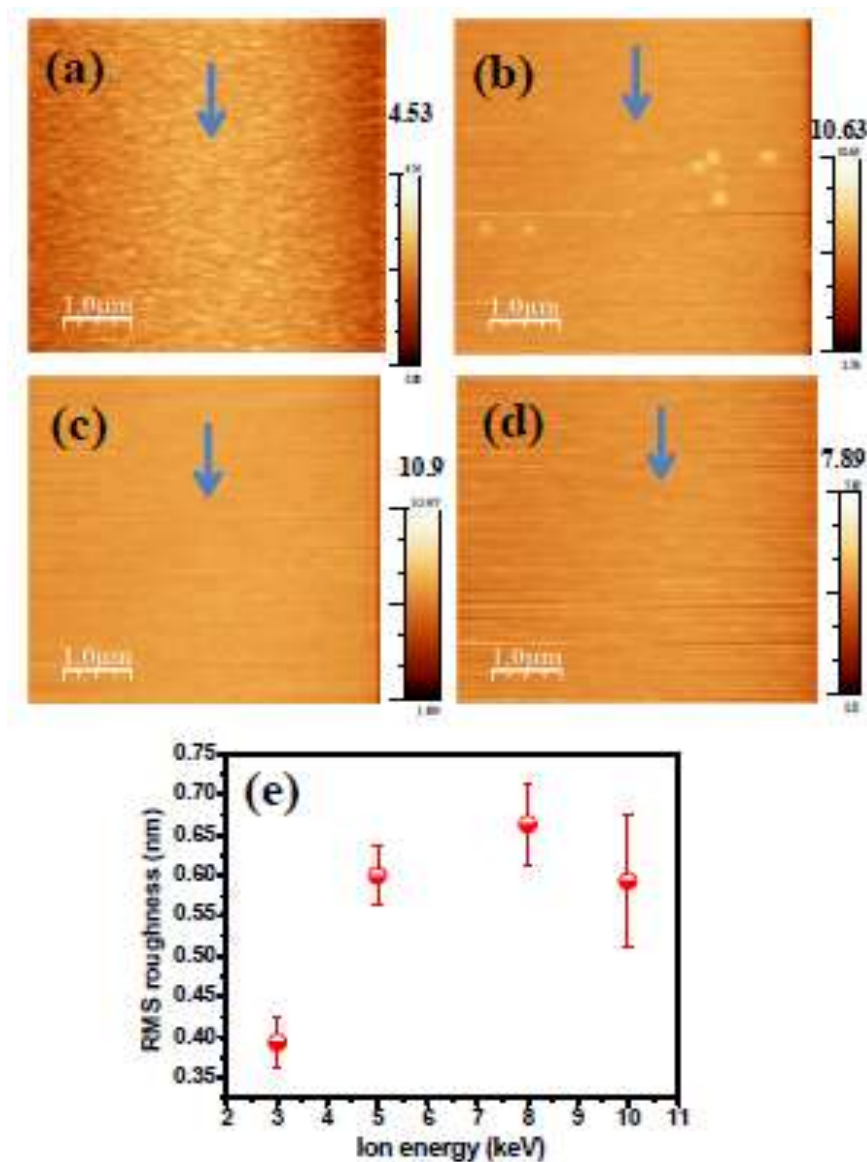


Figure 6.1 : AFM images of mass analyzed Ar bombarded Si surface with ion energy (a) 3 keV, (b) 5 keV, (c) 8 keV, and (d) 10 keV at an oblique angle of incidence 60° with constant ion fluence 7×10^{17} ions/cm². The arrow in each image indicates the ion beam direction, and the Z scale is shown with each image. (e) The RMS roughness of mass analyzed Ar bombarded Si surfaces with ion energy.

Figure 6.2 shows the XPS spectra of mass analyzed 5 keV and 10 keV Ar⁺ ion-bombarded Si as well as virgin Si surface. It is clear from the figure that the surface chemical state of Si has not changed due to 5 or 10 keV mass analyzed Ar⁺ ion bombardment. The oxide

peak for all the three surfaces in Figure 6.2 is for the native oxide layer, formed due to air exposure during sample transfer from the implantation chamber to the XPS system. The binding energies and concentrations of elemental Si and SiO_x for all the surfaces are mentioned in Figure 6.2. Similar oxide state at this binding energy was observed for oxide growth in Si nanowires (NWs) [223]. The implantation of Ar atoms is confirmed by high-resolution Ar 2p core level XPS spectrum (Fig. 6.4 a). Ar 2p_{1/2} and 2p_{3/2} are clearly resolved with separation of 2.1 eV, which indicates inertness of Ar within the Si matrix.

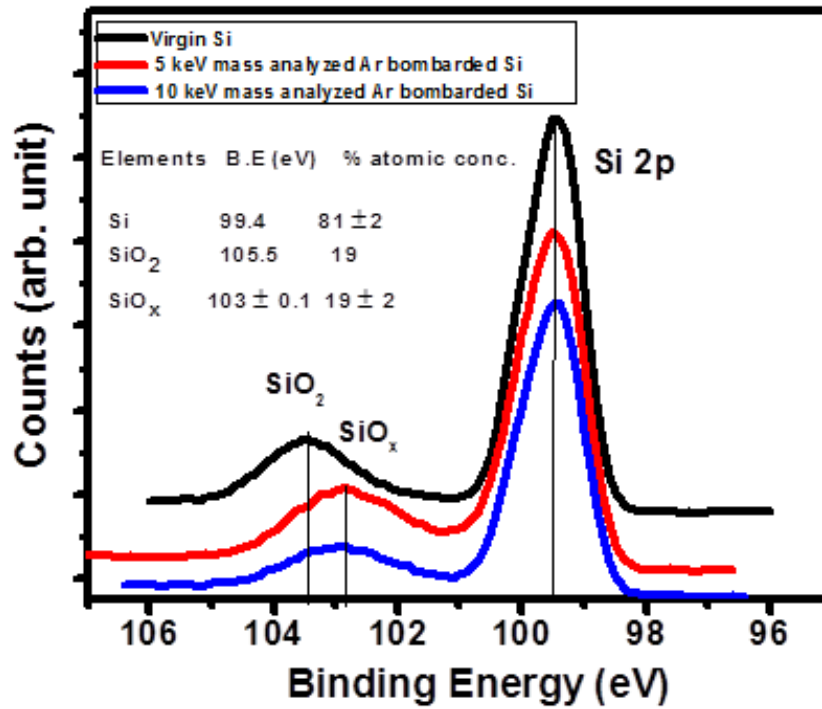


Figure 6.2 : High resolution Si 2p core level spectra of virgin Si, 5 keV, and 10 keV mass analyzed Ar bombarded Si.

The distribution of implanted 5 keV Ar atoms at 60° in Si as a function of depth is simulated by TRIM [11] and presented in Figure 6.3 (b). Ar atoms during irradiation transfer its energy to the target material and penetrate up to a certain depth. As the Si surface is amorphized by ion bombardment, the inert Ar atoms are trapped randomly in the amorphous layer. Well defined ripple formation on Si surface by Ar^+ ion beam at moderate ion fluence is only possible when the surface instability driven growth rate of ripple amplitude is appreciable. The appreciable amplitude of ripple can be achieved by Ar^+ ion energy more than 10 keV [30, 214-222], or at very high fluence [211, 212].

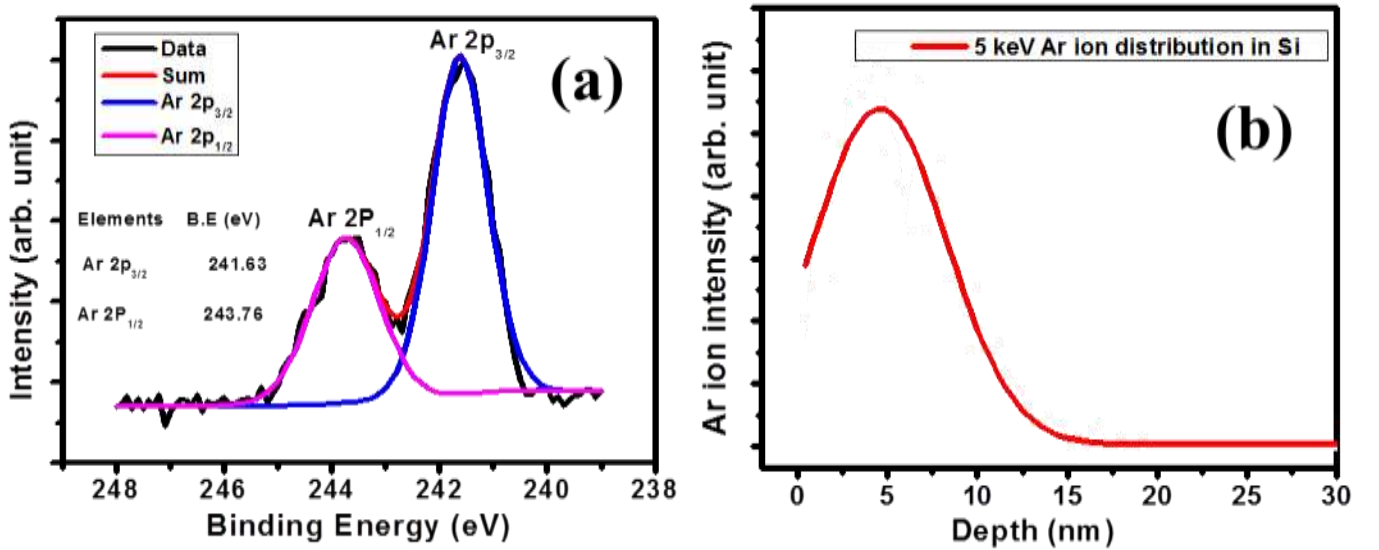


Figure 6.3: (a) High resolution Ar 2p core level spectra of 5 keV mass analyzed Ar bombarded Si surfaces. (b) TRIM calculation of implanted Ar distribution for 5 keV Ar bombarded Si at 60° .

Therefore, Si ripple formation by mass analyzed Ar^+ ions of energy up to 10 keV at moderate fluence is unlikely as the sputtering, mass redistribution of Si target atoms, and presence of inert ion implantation are not sufficient to generate instability for surface pattern formation. However, presence of additional reactive atoms/ions in the incident beam and the

subsequent surface chemical change may enhance the instability required for ripple pattern formation.

To verify our assumption, we bombarded the Si surfaces by impure Ar^+ beam of energy 3-10 keV without mass filtration. We kept the same ion beam parameters and ion surface geometry as before. The experiments were performed before the dipole magnet (mass analyzer) as shown in Figure 3.1. The AFM morphologies of Si surfaces after the bombardment with unanalyzed 3-10 keV Ar^+ beam are shown in Figures 6.4 (a) – (d). All the bombarded surfaces show well periodic nanoripple pattern. The rms roughness and ripple wavelength of the bombarded surfaces with ion energy are shown in Figures 6.4 (e) and (f). The rms roughness of the surfaces changes with ion energy within ± 1 nm, whereas the ripple wavelength increases with ion energy as usual.

To investigate the possible reason of nanopattern formation with unanalyzed ion beam, we took the mass spectrum of the ion beam as well as investigated the irradiated Si surfaces by XPS. The XPS survey of 5 keV and 10 keV Ar^+ ion bombarded as well as virgin Si surfaces with and without mass analyzer is shown in Figure 6.5 (a). The virgin Si surface contains Si, oxygen (O1s), and carbon (C1s). The presence of carbon and oxygen in Si is common [190]. Oxygen comes from the native oxide layer if it is exposed to air, and a trace amount of C remains during the Si wafer processing. We compare the XPS survey spectrum of virgin Si and the 5 & 10 keV mass filtered and unfiltered Ar^+ ions bombarded Si surfaces. For mass filtered Ar^+ ion bombardment, Ar peak is observed in addition to Si, C, and O peaks. It shows that the surface contains the same elements as in the virgin Si with an additional Ar peak, but in the case of unanalyzed Ar bombardment, a new N peak is found. It proves the presence of contamination in the mass unanalyzed ion-bombarded Si surfaces. The atomic concentration of different elements

in the virgin Si, 10 keV mass analyzed and mass unanalyzed Ar bombarded Si surfaces is shown in Figure 6.5(b).

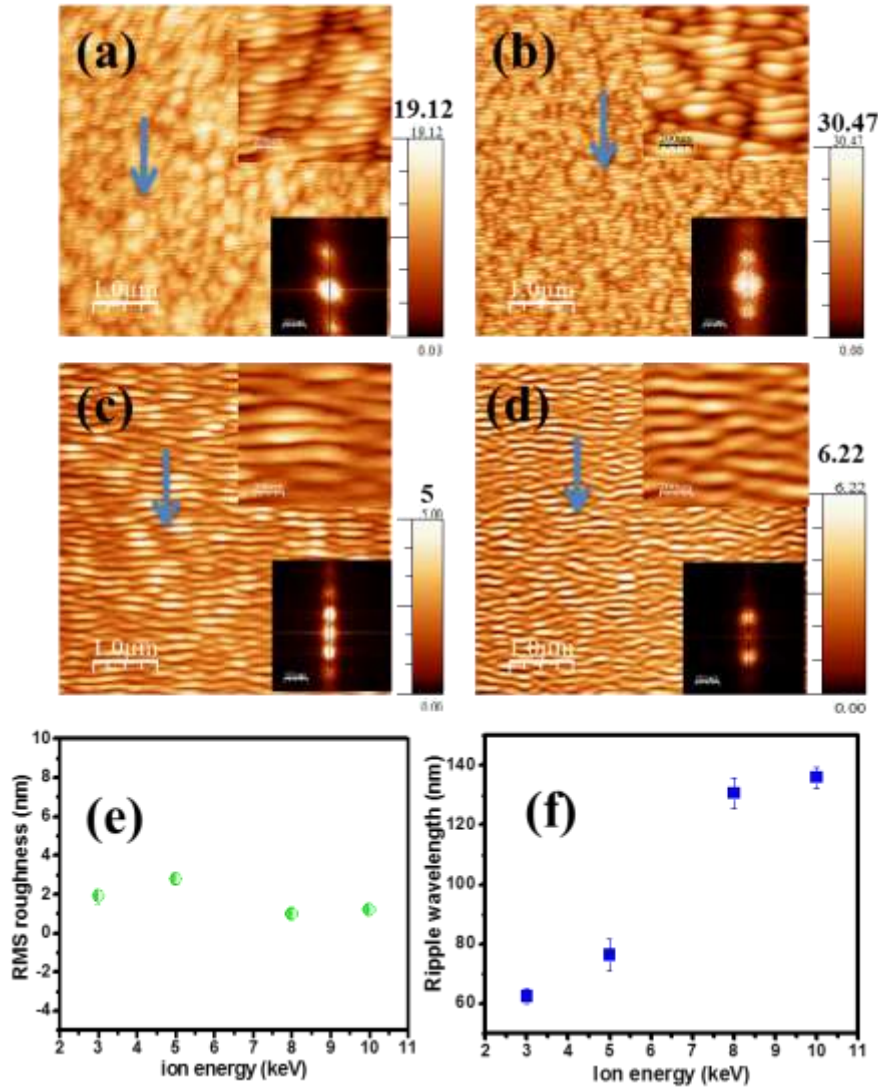


Figure 6.4 : AFM images ($5\mu\text{m} \times 5\mu\text{m}$) of without mass analyzed Ar bombarded Si surfaces with ion energy (a) 3 keV, (b) 5 keV, (c) 8 keV, and (d) 10 keV at oblique angle of incidence 60° with constant ion fluence 7×10^{17} ions/cm². The FFTs are shown in the corner of each image showing parallel mode ripple pattern formation. The $1\mu\text{m} \times 1\mu\text{m}$ scan AFM images are also shown in the upper corner of each AFM images. The arrows indicate the ion beam direction, and

also the Z scale is shown near each image. (e) The surface RMS roughness and (f) ripple wavelength of mass unanalyzed Ar bombarded Si surfaces with ion energy.

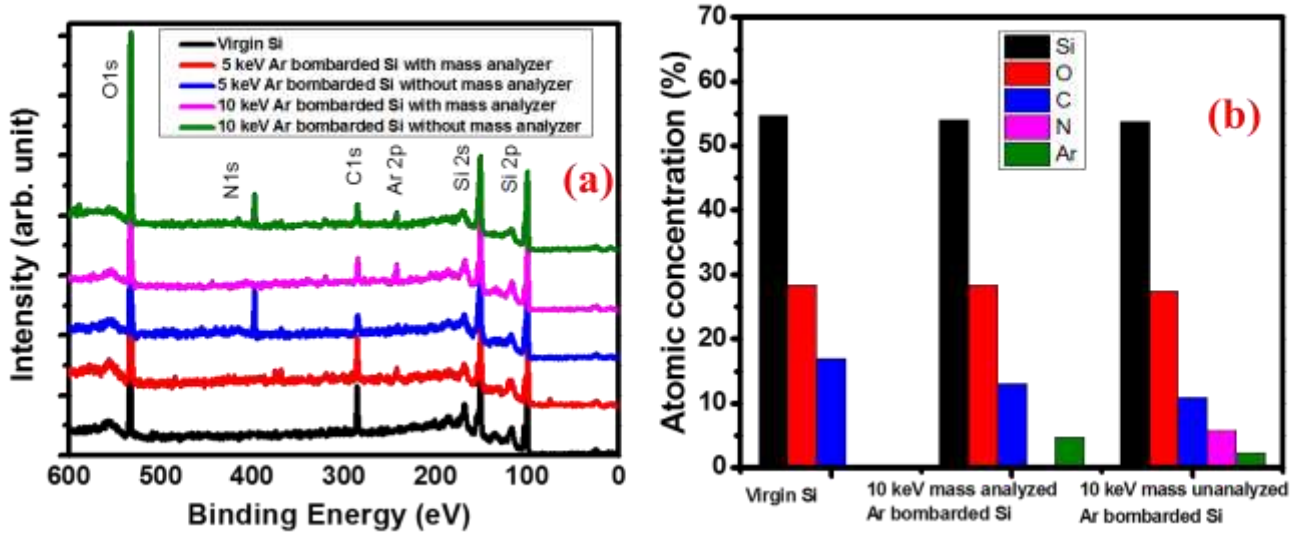


Figure 6.5: (a) XPS survey of virgin Si and ion bombarded Si surfaces with mass analyzed beam and without mass analyzed beam. (b) Atomic concentration of different elements in virgin Si, 10 keV mass analyzed, and mass unanalyzed Ar bombarded Si surfaces calculated from XPS survey.

To identify and quantify the presence of contamination in the unfiltered beam, we have recorded the mass spectrum of the ion beam, extracted at 5 keV by the same analyzing magnet. The mass spectrum for 5 keV ion beam is shown in Figure 6.6. Although the ion source was filled with 99.99% pure Ar gas, we found H, N, O, and C species along with Ar in the form of ions. The N and O impurities come from the air during the gas filling, whereas C comes from the vacuum pump oil and other unknown sources. Adsorbed water vapor on the wall of ion source chamber is the source of H and O. As the unanalyzed Ar ion beam is a mixture of H, Ar, O, N, and C ions, all of these ions bombard the Si surface when the beam is not filtered by the analyzing magnet. This type of beam contamination is very common for almost all type of ion

sources [224-226]. The contaminations in the Ar^+ beam specifically C, O, and N like reactive species change the chemical nature of the surface, which generates additional surface instability during ion bombardment.

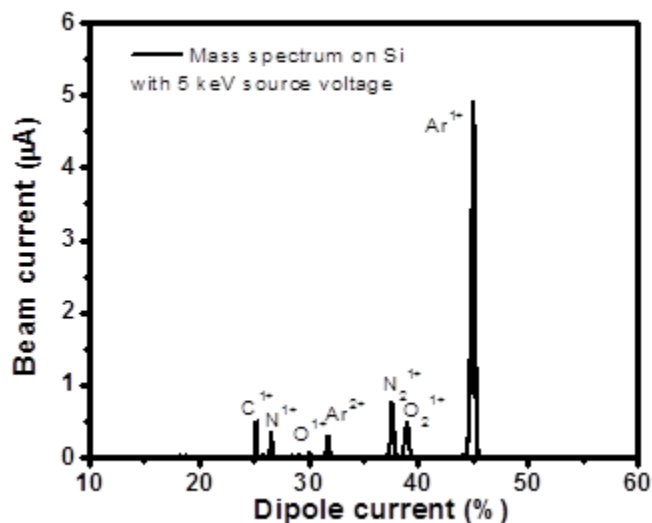


Figure 6.6: Mass spectrum on Si (100) sample by 5 keV source voltage extracted from ECR ion source

The change of surface chemistry due to the contaminated Ar^+ ion bombardment is further investigated in detail by high-resolution XPS measurements. Figures 6.7 (a) and (b) show the Si 2p core level spectra of Si surfaces, bombarded with the unfiltered Ar^+ ion (5 & 10 keV). The Si 2p peak can be fitted by four p-type Gauss-Lorentz peaks ($2p_{3/2} + 2p_{1/2}$) which contain elemental Si (B.E. = 99.2 ± 0.15 eV), SiC (B.E. = 100 ± 0.1 eV), Si_3N_4 (B.E. = 101.4 ± 0.2 eV), and SiO_2 (B.E. = 103 ± 0.2 eV). Also, the % area of unreacted Si and its compound are calculated from Figures 6.7 (a) & (b), which are shown in Table 6. 1.

Table 6.1. % area of unreacted Si and its compounds from Figures 6.7 (a) & (b).

	Unreacted Si	SiC	Si ₃ N ₄	SiO ₂
5 keV ion energy	34	36	16	14
10 keV ion energy	28	39	19	14

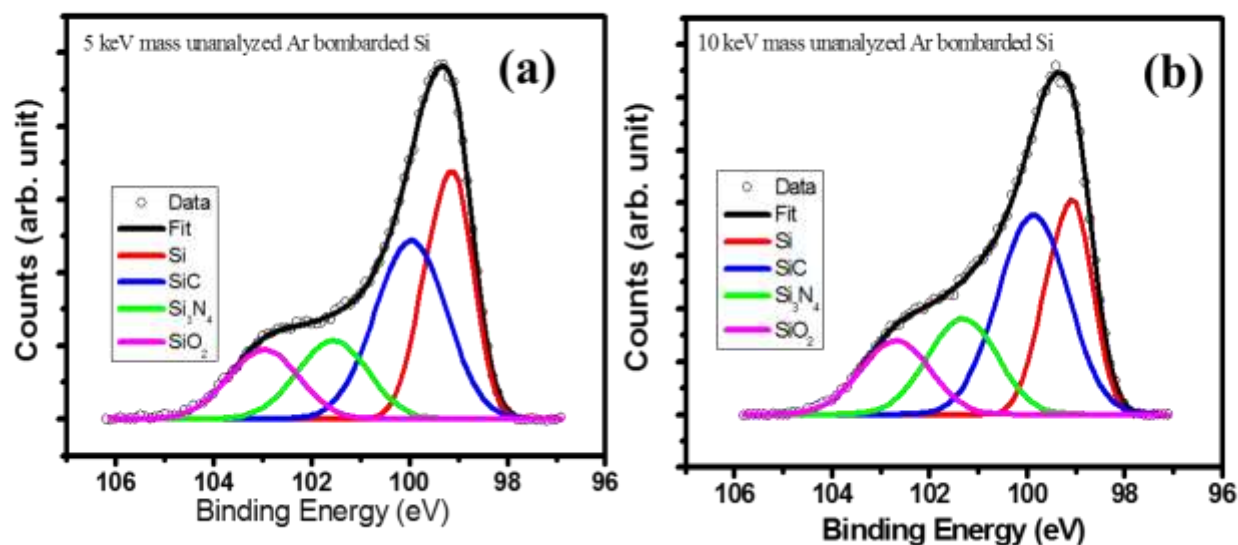


Figure 6.7 : High-resolution Si 2p core level spectra of (a) 5 keV mass unanalyzed and (b) 10 keV mass unanalyzed Ar bombarded surfaces showing chemical compound formation.

As C is present in all the samples, we have taken high-resolution spectra for C 1s for the virgin and Ar bombarded Si surfaces. It is found that C beam plays a different role when implanted in Si compared to the carbon commonly present on Si surface as contamination. Figures 6.8 (a) and (b) show the core level C 1s spectra of virgin Si and 10 keV mass selected Ar bombarded Si surfaces. No chemical change of as present C in Si is observed here. However, C 1s high-resolution spectrum from Si surface, bombarded with the unanalyzed contaminated

(contains C ion also) beam, shows chemical alteration of C 1s spectra. The spectrum, shown in Figure 6.8 (c), is fitted by three peaks at 282.88 eV, 284.7 eV, and 286.5 eV corresponding to silicon carbide (SiC), elemental C, and hydroxyl (C-OH), respectively. The peak at 282.88 eV confirms the SiC formation by C⁺ impurity ions, present in the mass unanalyzed ion beam. The formation of Si₃N₄ and SiC during N and C ion bombardment to Si surface was also previously observed [40, 41, 150]. Table 6.2 shows the binding energies (B.E) of Si, SiC, Si₃N₄, and SiO₂, reported earlier and measured in the present study. The hump at 286.5 eV is due to hydroxyl adsorption, which was also observed previously around this binding energy [24, 227]. Similar hydroxyl (C-OH) hump is also present at slightly higher binding energy for virgin and 10 keV mass analyzed Ar bombarded Si surfaces as shown in Figures 6.8 (a) and (b). The high-resolution Ar 2p core-level spectrum for 5 keV mass unanalyzed Si surface is also shown in Figure 6.8 (d), which displays the splitting of Ar 2p_{3/2} and 2p_{1/2} with binding energy separation of 2.1 eV. It again shows inertness in Si as is observed before for Si surface bombarded with mass selected Ar ions (Fig. 6.4a).

Table 6.2. Some reported binding energies (eV) of Si 2p, C 1s and their compound along with the present experimental value.

Si region				C region		Ref.
Si	SiC	Si ₃ N ₄	SiO ₂	SiC	C	
99.8	100.3			283.3	285.4	[191]
		101.3	102.4			[192]
99.3	100.1			283.2	284.8	[190]
99.4			103.2			[228]
		101.8	103.7			[193]
99.2 ± 0.15	100.0 ± 0.1	101.4 ± 0.2	103.0 ± 0.2	282.9	284.6	Present work

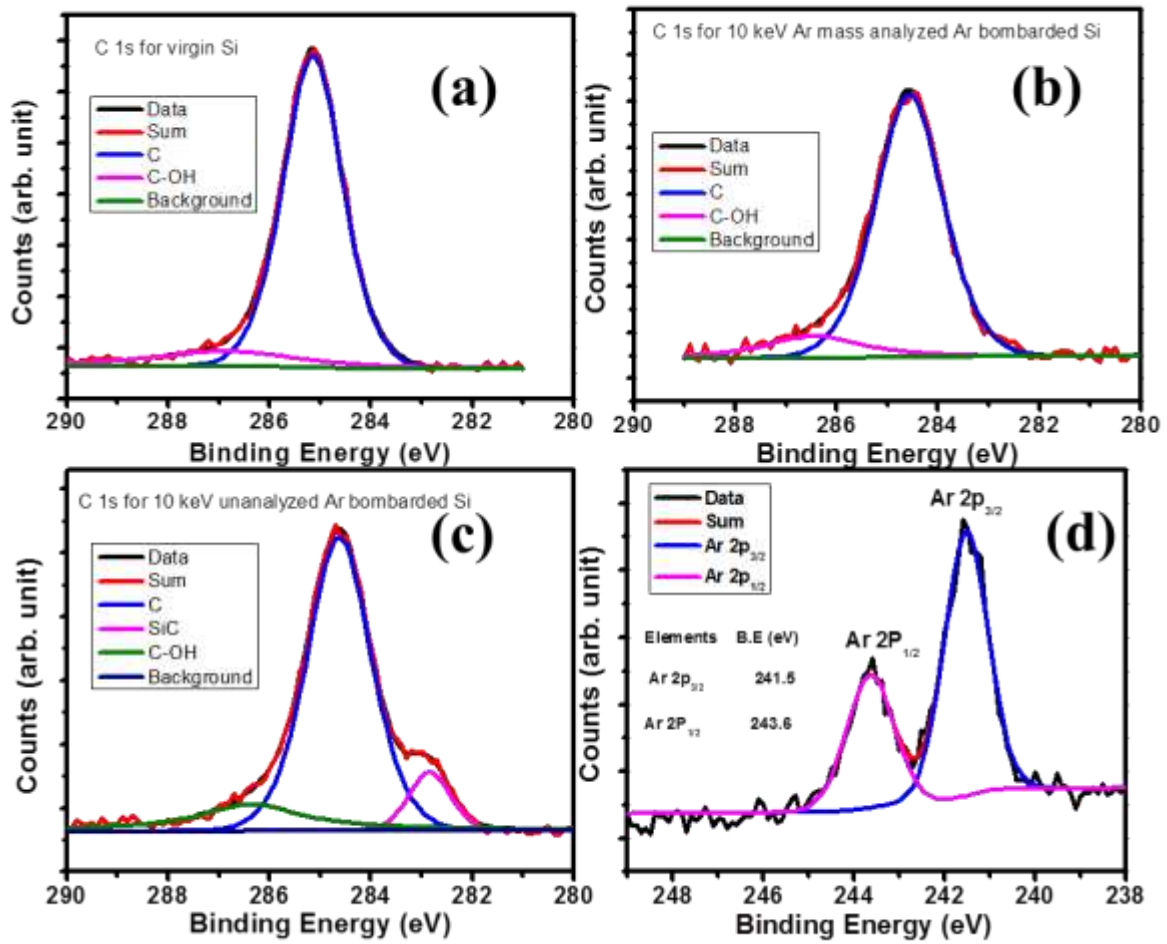


Figure 6.8: High resolution C 1s core level spectra of (a) virgin, (b) 10 keV mass analyzed, and (c) 10 keV mass unanalyzed Ar bombarded surfaces showing SiC formation. (d) Ar 2p core level spectrum for 5 keV mass unanalyzed Ar bombarded Si surface.

The absence of well-defined pattern by mass selected Ar⁺ beam indicates that when pure kinematics induced instabilities are not sufficient, reactive contaminants in the unanalyzed primary beam introduce the surface chemical inhomogeneity to generate required instability for the pattern formation. Ripple pattern formation is generally described on the basis of curvature dependent sputtering, mass redistribution, and effect of non-reactive implant species [5, 8, 10, 66, 93, 122, 174, 181]. Recently, Bradley has developed a new model of ripple formation

considering the co-deposition of inert [90] and reactive [92] impurities during ion bombardment. The coupled equations for the model of reactive impurities are given as [92]

$$\frac{\partial h}{\partial t} = -\Omega_1(F_A - F_D) - \Omega_2(F_B + \nabla \cdot \mathbf{J}_2) - \Omega_3 \nabla \cdot \mathbf{J}_3 \quad (1)$$

$$\Delta \frac{\partial n_3}{\partial t} = F_D - F_A - \nabla \cdot \mathbf{J}_3 \quad (2)$$

where, A and B denote the atoms of impurities and atoms of solid surface, respectively. F_A and F_B are the sputtered fluxes of species A and B. F_D is the flux of A atoms deposited on the surface. J_2 and J_3 are the surface current of B atoms and chemical compound of A & B atoms (AB_m molecule, m is integer). n_3 denotes the number density of AB_m molecules, and Δ is the deposited impurity layer thickness which is of the order of ion penetration depth. It has been shown in the model that the formation of compound destabilizes the surface due to unequal sputtering rate of elemental target material and its compound. If the sputtering rate of target material is more than the compound, the ripple patterns are formed. This model is applicable for the present case where reactive impurities in the Ar ion beam form silicon compounds. We have calculated the sputtering yield of Si and its compounds for 10 keV Ar bombardment at 60° angle of incidence by TRIM simulation. We have also calculated the erosion rate of pure Si and its compounds and found that the erosion rate is higher for pure Si than its compounds (Table 6.3). The ripple formation by Ar^+ ion in presence of reactive impurities is therefore consistent with the Bradley model [92]. Macko et al. also observed the higher erosion rate of Si than its metal silicides and found ripple patterns [19]. The formation of Si_3N_4 compound during 12 keV N^+ bombardments on the Si surface was observed where the unequal sputtering of Si_3N_4 & Si generated the surface instability for the ripple pattern formation [41]. We recently have reported the ripple pattern formation due to the preferential sputtering of different elements, presented on multi-elemental

mica, by 12 keV mass analyzed Ar bombardment [68]. For Si like mono-elemental surface, low energy noble ions cannot generate sufficient instability to form a pattern, hence, only a flat surface with very low roughness is formed even after long time bombardment. It was previously reported that the reactive O or C or N ion bombardment could generate instability on Si surface for ripple pattern formation [10, 31, 40-42, 213, 229-232]. Recently, it has been observed by Novakowski et al. [233] that the chemical phase of Si has changed to SiC by 100 eV He⁺ ion bombardment on Si surface. They have also found N 1s peak in XPS survey spectrum for ion bombarded surface, which indicates the presence of C and N contamination along with the He⁺ ion beam. In the coupled equations of Bradley model [92], only one type of co deposited metallic impurity (A) is considered, while the deposition of multiple reactive impurities in ionic state is somewhat different as they easily form multiple chemical compound by reacting with the Si atoms. This model may be more applicable for the present case if the specific amendments are applied. In summary, the present study with the surface chemical analysis establishes the fact that the ripple patterning on Si surface by the mass unanalyzed Ar⁺ ion (3-10 keV) is mainly due to the presence of reactive impurities in the ion beam.

Table 6.3. Sputtering yield (Y) and erosion rate (Y/ ρ) of several compounds of Si.

Composition	Y _{Si} (Si atoms per ion)	Y (atoms per ion)	ρ (atoms. nm ⁻³)	Y/ ρ (nm ⁻³ ion ⁻¹)
Si	7.48	7.48	50	0.1496
Si ₃ N ₄	3.1	9.4	95.5	0.0984
SiC	4.06	6.5	95	0.0684
SiO ₂	2.68	10.8	80	0.135

In summary, we have experimentally observed the mass analyzed and without mass analyzed Ar^+ ion beam induced pattern formation on Si surface. For the mass analyzed ion bombardment, no chemical change of the Si surface has taken place and a flat surface is formed, whereas for the mass unanalyzed ion bombardment, surface chemistry is significantly changed, and the well periodic ripple pattern is observed on the Si surface. This experimental understanding establishes the fact that the presence of contaminants with ion beam plays a key role in the low energy (3-10 keV) Ar^+ ion-induced ripple pattern formation on Si. Our results will give a boost to study the beam purity and the surface chemistry of the patterns, formed by mass unanalyzed ion beam. In case of reactive ion beam, the ions play the dual role of projectile and impurity which are deposited at the same angle, whereas in case of co-deposition, incident angles of projectile and impurity are different [19, 90, 92]; the ions are also chemically more reactive than co-deposited atoms. The present work will stimulate to extend the theoretical understanding by incorporating the effect of reactive impurities in the primary ion beam.

Chapter 7

Summary and outlook

The present thesis mainly involves the surface and interface modifications of Si (100) and muscovite mica by low energy (~ 10 keV) ion beam sputtering and implantation. Most of the studies of this thesis are related to the surface modification in terms of well periodic pattern formation. The interface and chemistry of the surfaces due to ion implantation are investigated in detail by cross-sectional Transmission Electron Microscopy (TEM) and X-ray Photoelectron Spectroscopy (XPS), respectively. The low energy ion beam technique offers the large scale modification on a surface, and it has precise control on concentration and depth, which has made this technique unique. Apart from surface modification, this technique also affects the compositional, electrical, magnetic, and mechanical properties of surface.

We have studied the formation of periodic nanostructure on Si surface and plasmon active nickel silicide (Ni_2Si) layer just below the surface, which are achieved simultaneously by a single step Ni^+ ion implantation. We have elaborated the potential application of the patterned and Ni_2Si embedded amorphous thin layer in solar devices. The presence of buried silicide layer enhances the optical absorption of Si surface in the visible spectrum by plasmon induced resonance energy transfer and direct electron transfer from plasmon to Si surface. This technique is more advantageous over other techniques, as it does not need multi-steps processes like annealing, deposition.

The energetic ion bombardment on Si like semiconducting surface leads to form well periodic ripple pattern at oblique angle incidence. The growth of ripple pattern on Si surfaces by several energetic (5-12 keV) N^+ ion bombardments is discussed. The horizontal and vertical

dimensions of the pattern are controlled in terms of ion energy. The experimentally observed horizontal dimension i.e., ripple wavelength and vertical dimension i.e., rms roughness are directly proportional to the theoretically calculated horizontal width of the collision cascade and ion penetration depth, respectively. We have also extended the optical and wettability study of the patterned surfaces. The hydrophobicity is well tuned by measuring water contact angle of N bombarded Si surfaces. We have observed the increase in optical absorption of N bombarded Si surfaces, which has potential application for the photovoltaic device as well as anti-reflective coating surface.

Next, we have studied the surface and interface modification of multi-elemental layered substrate muscovite mica. The periodic ripple pattern formation on mica by 12 keV Ar^+ and N^+ bombardment is discussed in detail. The growth of the pattern surfaces is explained in terms of several continuum models as well as dynamic scaling theory. The detailed scaling theory study aids to control the growth of nano-pattern on a solid surface by calculating different scaling exponents. Mica being a layered substrate, its chemical composition is immensely changed by ion bombardment, which has been investigated by XPS analysis. The K atoms, which are arranged at the top surface of mica, are sputtered most due to ion bombardment; as a result, the underlayer aluminosilicate is exposed to adsorb hydrocarbon from an ambient atmosphere. Both the Ar^+ and N^+ bombardment sputter K atoms, and the bombarded surfaces adsorb carbon from the ambient atmosphere. The interface of mica i.e., the aluminosilicate layer is also modified drastically by breaking Si-O and Al-O bonds as well as forming several chemical compounds during ion implantation. The inert Ar atoms are trapped in the aluminosilicate layer, whereas the reactive N atoms implant into the aluminosilicate layer and form nitride by reacting with Si & Al. The physical change i.e., the periodic ripple pattern formation and chemical change lead to

decrease the surface energy [24], hence, the superhydrophilic mica surface transforms to hydrophobic surface for both the ion bombarded surfaces.

Lastly, we have explored the critical role of impurities with primary ion beam itself on ripple pattern formation by inert ion bombardment. The pattern formation on Si surface by medium energy (3-12 keV) pure Ar^+ ion is forbidden. However, the pattern formation was observed by external metal incorporation [20, 21, 23, 28, 29] during normal incidence inert ion bombardment, but we have here studied the pattern formation in a new way on Si surface by impure Ar^+ ion bombardment. The reactive impurities (N^+ , O^+ , C^+) with Ar^+ ion beam and consequent chemical alteration of Si surface play the major role on Si pattern formation.

Overall, the studies, presented in this thesis, demonstrate the ion beam induced periodic pattern formation for the basic understanding of ion-solid interaction and for the potential applications. The plasmon active buried layer formation by just single step ion implantation on Si surface is a new way to extend the study for photovoltaic application. The investigation of detailed chemistry of an important atomically flat multi-elemental mica surface opens up to study the chemical modifications by ion bombardment. We have explored that hydrophobicity can be precisely tuned by ion beam parameters. The most important finding of this thesis is the idea of impurities with ion beam itself and role of beam impurities on Si pattern, which will aid to investigate the surface chemistry of the substrate by mass unanalyzed ion bombardment. Our works will open up the scopes to study further in continuation to the present results like the pattern formation on Si and mica surfaces by energetic ion bombardment can be investigated by changing conventional geometry of ion incident angle. We have studied the modification of mica surface by ion bombardment in detail; the interaction of biological substances like protein, DNA with modified mica surface could be an interesting study. Also, the study of mica surface is

limited to Ar^+ and N^+ ion only, so the study of other ions like C^+ , O^+ will explore the interaction mechanism of mica surface with those ions. The pattern formation with impure mass unanalyzed inert ion beam suggests that the chemical nature of Si surface by low energy (~ 500 eV) mass unanalyzed inert ion bombardment should be investigated for conclusion whether the pattern is for the pure dynamics of inert ion bombardment or purely chemical change of Si. We believe that our work is able to solve some of the problems in the field of ion beam induced material science study.

References

- [1] T.W.H. Oates, A. Keller, S. Facsko, A. Mücklich, *Plasmonics*, 2 (2007) 47.
- [2] J. Fassbender, T. Strache, M.O. Liedke, D. Marko, S. Wintz, K. Lenz, A. Keller, S. Facsko, I. Monch, J. McCord, *New J. Phys*, 11 (2009) 125002.
- [3] M. Liedke, M. Körner, K. Lenz, F. Grossmann, S. Facsko, *Appl. Phys. Lett.*, 100 (2012) 242405.
- [4] M. Navez, C. Sella, D. Chaperot, *C.R. Acad. Sci.*, 254 (1962) 240.
- [5] R.M. Bradley, J.M.E. Harper, *J. Vac. Sci. Technol. A*, 6 (1988) 2390.
- [6] P. Sigmund, *J. Mater. Sci.*, 8 (1973) 1545.
- [7] J. Muñoz-García, L. Vázquez, M. Castro, R. Gago, A. Redondo-Cubero, A. Moreno-Barrado, R. Cuerno, *Mater. Sci. Eng. R*, 86 (2014) 1.
- [8] G. Carter, V. Vishnyakov, *Phys. Rev. B* 54 (1996) 17647.
- [9] C.S. Madi, E. Anzenberg, K.F. Ludwig, M.J. Aziz, *Phys. Rev. Lett.*, 106 (2011) 066101.
- [10] R.M. Bradley, H. Hofsass, *J. Appl. Phys.*, 120 (2016) 074302.
- [11] J.F. Ziegler, M.D. Ziegler, J.P. Biersack, *Nucl. Instr. Meth. Phys. Res. B*, 268 (2010) 1818–1823
- [12] I. Horcas, R. Fernández, J.M. Gómez-Rodríguez, J. Colchero, J. Gómez-Herrero, A.M. Baro, *Rev. Sci. Instrum.*, 78 (2007) 013705.
- [13] P. Eaton, W. West, "Substrates for AFM", pp. 87-89 in *Atomic Force Microscopy*, Oxford University Press, 2010.
- [14] S. Singh, D.J. Keller, *Biophysical Journal*, 60 (1991) 1401.
- [15] T. Thundat, D.P. Allison, R.J. Warmack, G.M. Brown, K.B. Jacobson, J.J. Schrick, T.L. Ferrell, E. Henderson, W. Heckl, S.M. Lindsay, *Scanning Microscopy*, 6 (1992) 911.

- [16] B. Ziberi, F. Frost, B. Rauschenbach, Appl. Phys. Lett., 88 (2006) 173115.
- [17] B. Ziberi, F. Frost, T. Höche, B. Rauschenbach, Phys. Rev. B, 72 (2005) 235310.
- [18] S. Macko, F. Frost, B. Ziberi, D.F. Förster, T. Michely, Nanotechnology, 21 (2010) 085301.
- [19] S. Macko, F. Frost, M. Engler, D. Hirsch, T. Höche, J. Grenzer, T. Michely, New J. Phys., 13 (2011) 073017.
- [20] H. Hofsass, K. Zhang, Nucl. Instrum. Methods Phys. Res. B, 267 (2009) 2731.
- [21] M. Engler, F. Frost, S. Müller, S. Macko, M. Will, R. Feder, D. Spemann, R. Hübner, S. Facsko, T. Michely, Nanotechnology, 25 (2014) 115303.
- [22] K. Zhang, M. Brötzmann, H. Hofsäss, New J. Phys., 13 (2011) 013033.
- [23] B. Moon, S. Yoo, J.-S. Kim, S.J. Kang, J. Muñoz-García, R. Cuerno, Phys. Rev. B, 93 (2016) 115430.
- [24] A. Keller, M. Fritzsche, R. Ogaki, I. Bald, S. Facsko, M. Dong, P. Kingshott, F. Besenbacher, J. Chem. Phys., 134 (2011) 104705.
- [25] M.A. Makeev, A.L. Barabasi, Appl. Phys. Lett., 71 (1977) 2800.
- [26] R. Cuerno, A.L. Barabasi, Phys. Rev. Lett. , 74 (1995) 4746
- [27] M.A. Makeev, R. Cuerno, A.-L. Barabási, Nucl. Instrum. Methods Phys. Res. B, 197 (2002) 185.
- [28] G. Ozaydin, A.S. Özcan, Y. Wang, K.F. Ludwig, H. Zhou, R.L. Headrick, D.P. Siddons, Appl. Phys. Lett., 87 (2005) 163104.
- [29] G. Ozaydin-Ince, K.F.L. Jr, J. Phys.: Condens. Matter, 21 (2009) 224008.
- [30] G. Carter, M.J. Nobes, F. Paton, J.S. Williams, J.L. Whitton, Radiat. Eff. Defects Solids, 33 (1977) 65.
- [31] J.J. Vajo, R.E. Doty, E. Cirlin, J. Vac. Sci. Technol. B, 14 (1996) 2709.

- [32] E. Chason, T.M. Mayer, B.K. Kellermann, D.N. McIlroy, H.A. J, Phys. Rev. Lett., 72 (1994) 3040.
- [33] J. Erlebacher, M.J. Aziz, E. Chason, M.B. Sinclair, J.A. Floro, Phys. Rev. Lett., 82 (1999) 2330.
- [34] A. Metya, D. Ghose, S.A. Mollick, A. Majumdar, J. Appl. Phys., 111 (2012) 074306.
- [35] T.M. Mayer, E. Chason, A.J. Howard, J. Appl. Phys., 76 (1994) 1633.
- [36] S. Rusponi, G. Constantini, C. Boragno, U. Valbusa, Phys. Rev. Lett., 81 (1998) 2735.
- [37] U. Valbusa, C. Boragno, F.B.d. Mongeot, Journal of Physics: Condensed Matter, 14 (2002) 8153.
- [38] S. Rusponi, C. Boragno, U. Valbusa, Phys. Rev. Lett., 78 (1997) 2795.
- [39] D. Bhowmik, P. Karmakar, AIP Conference Proceedings, 1953 (2018) 100071.
- [40] S. Bhattacharjee, P. Karmakar, V. Naik, A.K. Sinha, A. Chakrabarti, Appl. Phys. Lett., 103 (2013) 181601.
- [41] P. Karmakar, B. Satpati, J. Appl. Phys., 120 (2016) 025301.
- [42] D. Bhowmik, S. Bhattacharjee, D. Lavanyakumar, V. Naik, B. Satpati, P. Karmakar, Appl. Surf. Sci., 422 (2017) 11.
- [43] G.A. Prinz, Science, 282 (1998) 1660.
- [44] M.A. Reed, C. Zhou, C. Muller, T. Burgin, J. Tour, Science 278 (1997) 252.
- [45] J.-H. Lee, T.T. Paull, Science, 308 (2005) 551.
- [46] M. Ranjan, T.W.H. Oates, S. Facsko, W. Möller, Optics Lett., 35 (2010) 2576.
- [47] F. Bisio, R. Moroni, F.B.d. Mongeot, M. Canepa, L. Mattera, Phys. Rev. Lett., 96 (2006) 057204.
- [48] B. Teshome, S. Facsko, A. Keller, Nanoscale Res. Lett., 6 (2014) 1790.

- [49] S. Majumder, I. Mishra, U. Subudhi, S. Varma, Appl. Phys. Lett. , 103 (2013) 063103.
- [50] M.A. Garcia, J. Rickards, R. Cuerno, R. Trejo-Luna, J. Cañetas-Ortega, L.R.d.l. Vega, L. Rodríguez-Fernández, Phys. Rev. Appl., 8 (2017) 064027.
- [51] M. Nastasi, J.W. Mayer, Ion Implantation and Synthesis of Materials, Springer - Verlag, Berlin Heidelberg, 2006.
- [52] P.S. W. KB, J. Sanders, Matematisk-Fysiske Meddelelser Udgivet af det Kongelige Danske Videnskabernes Selskab, 37 (1970) 1.
- [53] W. Bolse, Mater. Sci. Eng. :R: Reports, 12 (1994) vii-viii, 53-122.
- [54] P. Sigmund, Phys. Rev., 184 (1969) 383.
- [55] O.B. Duchemin, An Investigation of Ion Engine Erosion by Low Energy Sputtering, in, California Institute of Technology, 2001.
- [56] R. Behrisch, W. Eckstein, Sputtering by particle bombardment Springer-Verlag, Berlin, Heidelberg, 2007.
- [57] W. Eckstein, R. Preuss, J. Nucl. Mater., 320 (2003) 209.
- [58] Y. Yamamura, S. Shindo, Radiat. Eff. Defects Solids, 80 (1984) 57.
- [59] M. Moseler, P. Gumbsch, C. Casiraghi, A.C. Ferrari, J. Robertson, Science, 309 (2005) 1545.
- [60] J.A. DeRose, T. Thundat, L.A. Nagahara, S.M. Lindsay, Surf. Sci., 256 (1991) 102.
- [61] N. Kalyanasundaram, J.B. Freund, H.T. Johnson, J. Phys.: Condens. Matter, 21 (2009) 224018.
- [62] N. Kalyanasundaram, M. Ghazisaeidi, J.B. Freund, H.T. Johnson, Appl. Phys. Lett., 92 (2008) 131909.

- [63] S.A. Norris, J. Samela, L. Bukonte, M. Backman, F. Djurabekova, K. Nordlund, C.S. Madi, M.P. Brenner, M.J. Aziz, *Nat. Commun.*, 2 (2011) 276.
- [64] M. Castro, R. Cuerno, *Appl. Surf. Sci.*, 258 (2012) 4171.
- [65] S.A. Norris, *Phys. Rev. B*, 85 (2012) 155325.
- [66] O. Bobes, K. Zhang, H. Hofstäss, *Phys. Rev. B* 86 (2012) 235414.
- [67] W. Moller, *Nucl. Instrum. Methods Phys. Res., Sect. B*, 322 (2014) 23.
- [68] D. Bhowmik, D. Chowdhury, P. Karmakar, *Surf. Sci.*, 679 (2019) 86.
- [69] R.M. Bradley, H. Hofsäss, *J. Appl. Phys.*, 120 (2016) 074302.
- [70] P. Karmakar, S.A. Mollick, D. Ghose, A. Chakrabarti, *Appl. Phys. Lett.*, 93 (2008) 103102.
- [71] D. Bhowmik, M. Mukherjee, P. Karmakar, *Nucl. Instr. Meth. Phys. Res. B*, 444 (2019) 54-61.
- [72] D. Bhowmik, P. Karmakar, *AIP Conference Proceedings* 1832 (2017) 080019.
- [73] A. Lopez-Cazalilla, D. Chowdhury, A. Ilinov, S. Mondal, P. Barman, S.R. Bhattacharyya, D. Ghose, F. Djurabekova, K. Nordlund, S.A. Norris, *J. Appl. Phys.*, 123 (2018) 235108.
- [74] R. Cuerno, H.A. Makse, S. Tomassone, S.T. Harrington, H.E. Stanley, *Phys. Rev. Lett.*, 75 (1995) 4464.
- [75] A.-L. Barabasi, H.E. Stanley, *Fractal concepts in surface growth*, Cambridge university press, 1995.
- [76] M. Kardar, G. Parisi, Y.C. Zhang, *Phys. Rev. Lett.*, 56 (1986) 889.
- [77] S. Park, B. Kahng, H. Jeong, A.L. Barabási, *Phys. Rev. Lett.*, 83 (1999) 3486.
- [78] D. Chowdhury, D. Ghose, *Mater. Res. Express*, 3 (2016) 125003.
- [79] S. Facsko, T. Bobek, A. Stahl, H. Kurz, T. Dekorsy, *Phys. Rev. B*, 69 (2004) 153412.

- [80] S. Facsko, T. Dekorsy, C. Koerdts, C. Trappe, H. Kurz, A. Vogt, H.L. Hartnagel, *Science*, 285 (1999) 1551.
- [81] F. Frost, A. Schindler, F. Bigl, *Phys. Rev. Lett.*, 85 (2000) 4116.
- [82] M. Paniconi, K. Elder, *Phys. Rev. E*, 56 (1997) 2713.
- [83] H. Chate, P. Manneville, *Phys. Rev. Lett.*, 58 (1987) 112.
- [84] R. Cuerno, K.B. Lauritsen, *Phys. Rev. E*, 52 (1995) 4853.
- [85] R.M. Bradley, J. M. E. Harper, *J. Vac. Sci. Technol. A*, 6 (1988) 2390
- [86] B. Davidovitch, M.J. Aziz, M.P. Brenner, *Phys. Rev. B*, 76 (2007) 205420.
- [87] B. Ziberi, F. Frost, B. Rauschenbach, *Surf. Sci.*, 600 (2006) 3757.
- [88] H. Hofsass, K. Zhang, A. Pape, O. Bobes, M. Brotzmann, *Appl. Phys. A*, 111 (2013) 653.
- [89] D. Chen, G. Yang, J. Li, D. Hirsch, Y. Liu, F. Frost, Y. Hong, *Appl. Phys. Lett.*, 113 (2018) 033102.
- [90] R.M. Bradley, *Phys. Rev. B*, 83 (2011) 195410.
- [91] R.M. Bradley, *Phys. Rev. B*, 85 (2012) 115419.
- [92] R.M. Bradley, *Phys. Rev. B*, 87 (2013) 205408.
- [93] R.M. Bradley, *J. Appl. Phys.*, 119 (2016) 134305.
- [94] M.A. Auger, L. Vázquez, O. Sánchez, M. Jergel, R. Cuerno, M. Castro, *J. Appl. Phys.*, 97 (2005) 123528.
- [95] M.A. Auger, L. Vázquez, R. Cuerno, M. Castro, M. Jergel, O. Sánchez, *Phys. Rev. B*, 73 (2006) 045436.
- [96] B. Mohanty, H. Choi, Y. Cho, *Euro. Phys. Lett.*, 93 (2011) 26003
- [97] B.C. Mohanty, H.-R. Choi, Y.S. Cho, *J. Appl. Phys.*, 106 (2009) 054908.
- [98] A.S. Mata, S.C.F. Jr, I.R. Ribeiro, S.O. Ferreira, *Phys. Rev. B*, 78 (2008) 115305.

- [99] M. Saitou, Phys. Rev. B, 66 (2002) 073416.
- [100] M. Gedda, N.V.V. Subbarao, D.K. Goswami, Langmuir, 30 (2014) 8735.
- [101] A. Pal, J.C. Mahato, B.N. Dev, D.K. Goswami, ACS Appl. Mater. Interfaces, 5 (2013) 9517.
- [102] W.L. Chan, E. Chason, J. Appl. Phys., 101 (2007) 121301.
- [103] D. Chowdhury, D. Ghose, Appl. Surf. Sci., 324 (2015) 517.
- [104] A. Keller, R. Cuerno, S. Facsko, W. Möller, Phys. Rev. B, 79 (2009) 115437.
- [105] Y. Zhao, G.-C. Wang, T.-M. Lu, Characterization of Amorphous and Crystalline Rough Surface: Principles and Applications, Academic Press, San Diego, London, 2001.
- [106] A. Keller, S. Facsko, Materials, 3 (2010) 4811.
- [107] Y.-P. Zhao, J.T. Drotar, G.-C. Wang, T.-M. Lu, Phys. Rev. Lett., 82 (1999) 4882.
- [108] R. Pastor-Satorras, D.H. Rothman, J. Stat. Phys. 93(3/4), (1998) 477.
- [109] B. Schmittmann, G. Pruessner, H.-K. Janssen, Phys. Rev. E, 73 (2006) 051603.
- [110] E. Vivo, M. Nicoli, M. Engler, H. Michely, L. Vázquez, R. Cuerno, Phys. Rev. B, 86 (2012) 245427.
- [111] S. Zhu, L.M. Wang, X.T. Zu, X. Xiang, Appl. Phys. Lett., 88 (2006) 43107-43107.
- [112] H.A. Atwater, A. Polman, Nature Materials, 9 (2010) 205-213.
- [113] K.R. Catchpole, A. Polman, Applied Physics Letters, 93 (2008) 191113.
- [114] J. Muller, B. Rech, J. Springer, M. Vanecek, Solar energy, 77 (2004) 917-930.
- [115] A.R. Silva, J. Miyoshi, J.A. Diniz, I. Doi, J. Godoy, Energy Procedia, 44 (2014) 132-137.
- [116] J.Y. Huang, S.H. Li, M.Z. Ge, L.N. Wang, T.L. Xing, G.Q. Chen, X.F. Liu, S.S. Al-Deyab, K.Q. Zhang, T. Chen, Y.K. Lai, J. Mater. Chem. A, 3 (2015) 2825.

- [117] H. Tsuji, T. Sagimori, K.i. Kurita, Y. Gotoh, J. Ishikawa, *Surf. Coat. Technol.*, 158 (2002) 208-213.
- [118] R. Sachan, C. Gonzalez, O. Dyck, Y. Wu, H. Garcia, S.J. Pennycook, P.D. Rack, G. Duscher, R. Kalyanaraman, *Nanomaterials and Energy*, 2 (2012) 11.
- [119] P. Karmakar, B. Satpati, *Appl. Phys. Lett.*, 104 (2014) 231601.
- [120] B. Kahng, H. Jeong, A.L. Barabasi, *Appl. Phys. Lett.*, 78 (2001) 805.
- [121] J.C. Perkinson, E. Anzenberg, M.J. Aziz, K.F. Ludwig Jr, *Physical Review B*, 89 (2014) 115433.
- [122] M.P. Harrison, R.M. Bradley, *Phy. Rev. B*, 89 (2014) 245401.
- [123] E. Verleysen, H. Bender, O. Richard, D. Schryvers, W. Vandervorst, *Journal of Microscopy*, 240 (2010) 75-82.
- [124] R.F. Egerton, *Rep. Prog. Phys.*, 72 (2009) 016502.
- [125] Neil P. Dasgupta, S. Xu, H.J. Jung, A. Iancu, R. Fasching, R. Sinclair, F.B. Prinz, *Advanced Functional Materials*, 22 (2012) 3650.
- [126] G. Priyadarshini, M. Chakraborty, *Bull. Mater. Sci.*, 37 (2014) 1265.
- [127] H. Garcia, J. Trice, R. Kalyanaraman, R. Sureshkumar, *Physical Review B*, 75 (2007) 045439.
- [128] H. Sun, H.-C. Wu, S.-C. Chen, C.-W.M. Lee, X. Wang, *Nanoscale Res. Lett.*, 12 (2017) 224.
- [129] T. Basu, D.P. Datta, T. Som, *Nanoscale Res. Lett.*, 8 (2013) 289.
- [130] M. Lipiński, *Arch. Mater. Sci. Eng.*, 46 (2010) 69.
- [131] M. Lipinski, P. Zieba, S. Jonas, S. Kluska, M. Sokolowski, H. Czternastek, *Opto-Electronics Rev.*, 12 (2004) 41.

- [132] T. Iwahashi, M. Morishima, T. Fujibayashi, R. Yang, J. Lin, D. Matsunaga, J. Appl. Phys., 118 (2015) 145302.
- [133] S. Duttagupta, F. Ma, B. Hoex, T. Mueller, A.G. Aberle, Energy Procedia 18 (2012) 78.
- [134] S.V. Deshpande, E. Gulari, J. Appl. Phys., 77 (1995) 6534.
- [135] H. Charifi, A. Slaoui, J.P. Stoquert, H. Chaib, A. Hannour, World Journal of Condensed Matter Physics, 6 (2016) 7.
- [136] S. Agathopoulos, P. Nikolopoulos, J. Biomed. Mater.Res., 29 (1995) 421.
- [137] X.M. Yang, Z.W.Zhong, E.M.Diallo, Z.H.Wang, W.S.Yue, Mater. Sci. Semicond. Process., 26 (2014) 25.
- [138] S.K. Garg, D.P. Datta, J. Ghatak, I. Thakur, K. Khare, D. Kanjilal, T. Som, RSC Adv., 6 (2016) 48550
- [139] T. Kumar, U.B. Singh, M. Kumar, S. Ojha, D. Kanjilal, Curr. Appl. Phys., 14 (2014) 312.
- [140] D. Bhowmik, P. Karmakar, Nucl. Instrum. Methods Phys. Res. B, 422 (2018) 41.
- [141] M.T. Spuller, D.W. Hess, J. Electrochem. Soc., 150 (2003) 476.
- [142] A. Metya, D. Ghose, N.R. Ray, Appl. Surf. Sci., 293 (2014) 18.
- [143] D. Bhowmik, P. Karmakar, Surf. Interface Anal., (2019) 1-7.
- [144] R.N. Wenzel, Ind. Eng. Chem., 28 (1936) 988.
- [145] B. Bhushan, Y.C. Jung, Ultramicroscopy, 107 (2007) 1033.
- [146] H. Gau, S. Herminghaus, P. Lenz, R. Lipowsky, Science, 283 (1999) 46.
- [147] R. Blossey, Nat. Mater., 2 (2003) 301.
- [148] C.P. Saini, A. Barman, M. Kumar, B. Satpati, T. Som, A. Kanjilal, J. Appl. Phys., 119 (2016) 134904.

- [149] D. Qi, N. Lu, H. Xu, B. Yang, C. Huang, M. Xu, L. Gao, Z. Wang, L. Chi, *Langmuir*, 25 (2009) 7769.
- [150] S. Bhattacharjee, D. Lavanyakumar, V. Naik, S. Mondal, S.R. Bhattacharyya, P. Karmakar, *Thin Solid Films*, 645 (2018) 265.
- [151] H. Hofsass, O. Bobes, K. Zhang, *J. Appl. Phys.*, 119 (2016) 035302.
- [152] T. Young, *Philos. Trans. R. Soc. London*, (1805) 65-87.
- [153] C. Neinhuis, W. Barthlott, *Annals of Botany*, 79 (1997) 667.
- [154] A. Arafat, K. Schroen, L.C.P.M.d. Smet, E.J.R. Sudholter, H. Zuilhof, *J. Am. Chem. Soc.*, 126 (2004) 8601.
- [155] D.K. Agarwal, N. Maheshwari, S. Mukherji, R. Rao, *RSC Adv.*, 6 (2016) 17606-17616.
- [156] G.J. Wan, R.K.Y. Fu, P. Yang, J.P.Y. Ho, X. Xie, N. Huang, P.K. Chu, *Nucl. Instrum. Methods Phys. Res. B*, 242 (2006) 296.
- [157] J.J.M. Benavente, H. Mogami, T. Sakurai, K. Sawada, *PLoS ONE*, 9 (2014).
- [158] Z.-H. Liu, N.M.D. Brown, *J. Phys. D : Appl. Phys.*, 31 (1998) 1771.
- [159] P.K. Hansma, J.P. Cleveland, M. Radmacher, D.A. Walters, P.E. Hillner, M. Bezanilla, M. Fritz, D. Vie, H.G. Hansma, C.B. Prater, J. Massie, L. Fukunaga, J. Gurley, V. Elings, *Appl. Phys. Lett.*, 64 (1994) 1738.
- [160] L. Cai, H. Tabata, T. Kawai, *Appl. Phys. Lett.*, 77 (2000) 3105.
- [161] S. Ferrero, A. Piednoir, C.R. Henry, *Nano Lett.*, 1 (2001) 227.
- [162] H. Proehl, R. Nitsche, T. Dienel, K. Leo, T. Fritz, *Phys. Rev. B*, 71 (2005) 165207.
- [163] H. Proehl, T. Dienel, R. Nitsche, T. Fritz, *Phys. Rev. Lett.*, 93 (2004) 097403.
- [164] S. Camelio, D. Babonneau, D. Lantiat, L. Simonot, F. Pailloux, *Phys. Rev. B*, 80 (2009) 155434.

- [165] A. Toma, B.Š. Batič, D. Chiappe, C. Boragno, U. Valbusa, M. Godec, M. Jenko, F.B.d. Mongeot, J. Appl. Phys. , 104 (2008) 104313.
- [166] M.v.d. Veen, M.C. Stuart, W. Norde, Colloids and Surfaces B, 54 (2007) 136.
- [167] C. Jeworrek, O. Hollmann, R. Steitz, R. Winter, C. Czeslik, Biophys. J., 96 (2009) 1115.
- [168] F. Thibaudau, J. Cousty, E. Balanzat, S. Bouffard, Phys. Rev. Lett., 67 (1991) 1582.
- [169] R. Ritter, G. Kowarik, W. Meissl, A.S. El-Said, L. Maunoury, H. Lebius, C. Dufour, M. Toulemonde, F. Aumayr, Vacuum, 84 (2010).
- [170] R. Buzio, A. Toma, A. Chincarini, F.B.d. Mongeot, C. Boragno, U. Valbusa, Surf. Sci., 601 (2007) 2735.
- [171] D. Chowdhury, D. Ghose, Adv. Sci. Lett., 22 (2016) 105.
- [172] A. Metya, D. Ghose, AIP Conference Proceedings, 1591 (2014) 1015.
- [173] A. Metya, D. Ghose, Appl. Phys. Lett., 103 (2013) 161602.
- [174] E. Anzenberg, C.S. Madi, M.J. Aziz, J.K.F. Ludwig, Phys. Rev. B 84 (2011) 214108.
- [175] J. Munoz-Garcia, M. Castro, R. Cuerno, Phys. Rev. Lett. , 96 (2006) 086101.
- [176] A. Keller, S. Roßbach, S. Facsko, WolfhardMöller, Nanotechnology, 19 (2008) 13.
- [177] C.C. Umbach, R.L. Headrick, K.-C. Chang, Phys. Rev. Lett., 87 (2001) 246104.
- [178] A. Moreno-Barrado, M. Castro, R. Gago, L. Vázquez, J. Muñoz-García, A. Redondo-Cubero, B. Galiana, C. Ballesteros, R. Cuerno, Phys. Rev. B, 91 (2015) 155303.
- [179] C. Herring, J. Appl. Phys., 21 (1950) 301.
- [180] W.W. Mullins, J. Appl. Phys., 30 (1959) 77.
- [181] R.M. Bradley, H. Hofsäss, J. Appl. Phys., 116 (2014) 234304.
- [182] D. Flamm, F. Frost, D. Hirsch, Appl. Surf. Sci., 179 (2001) 95.
- [183] P. Karmakar, D. Ghose, Nucl. Instrum. Methods Phys. Res. B, 230 (2005) 539.

- [184] T. Som, T.K. Chini, Y.S. Katharia, S. Tripathy, D. Kanjilal, *Appl. Surf. Sci.*, 256 (2009) 562.
- [185] K.G. Bhattacharyya, *Journal of Electron Spectroscopy and Related Phenomena*, 63 (1993) 289.
- [186] K. Müller, C.C. Chang, *Surf. Sci.*, 14 (1969) 39.
- [187] K.G. Bhattacharyya, *Langmuir*, 5 (1989) 1155.
- [188] H. Poppa, A.G. Elliot, *Surf. Sci.*, 24 (1971) 149.
- [189] Atkins, Peter, J.d. Paula, Oxford University Press, Oxford, UK, 2006.
- [190] J.S. Pan, A.T.S. Wee, C.H.A. Huan, H.S. Tan, K.L. Tan, *J. Appl. Phys.*, 79 (1996) 2934.
- [191] I. Kusunoki, Y. Igari, *Appl. Surf. Sci.*, 59 (1992) 95.
- [192] J. Dai, W. Gao, B. Liu, X. Cao, TaoTao, Z. Xie, H. Zhao, D. Chen, H. Ping, R. Zhang, *Appl. Surf. Sci.*, 364 (2016) 886.
- [193] K. Azuma, S. Ueno, Y. Konishi, KazuhiroTakahashi, *Thin Solid Films*, 580 (2015) 111.
- [194] J.A. Taylor, J.W. Rabalais, *J. Chem. Phys.*, 75 (1981) 1735.
- [195] B. Ealet, M.H. Elyakhloufi, E. Gillet, M. Ricci, *Thin Solid Films*, 250 (1994) 92.
- [196] L. Rosenberger, R. Baird, E. McCullen, G. Auner, G. Shreve, *Surf. Interface Anal.*, 40 (2008) 1254.
- [197] C.D. Wagner, D.E. Passoja, H.F. Hillery, T.G. Kinisky, H.A. Six, W.T. Jansen, J.A. Taylor, *J. Vac. Sci. Technol.*, 21 (1982) 933.
- [198] F. Rueda, J. Mendialdua, A. Rodriguez, R. Casanova, Y. Barbaux, L. Gengembre, L. Jalowiecki, *J. Electron Spectrosc. Relat. Phenom.*, 82 (1996) 135.
- [199] J.A. Kovacich, D. Lichtman, *J. Electron Spectrosc. Relat. Phenom.*, 35 (1985) 7-18.
- [200] G.M. Ingo, N. Zacchetti, D.d. Sala, C. Coluzza, *J. Vac. Sci. Technol. A*, 7 (1989) 3048.

- [201] T. Hagio, A. Takase, S. Umebayashi, J. Mater. Sci. Lett. , 11 (1992) 878.
- [202] T.A. Dang, C.N.J. Chau, Electrochem. Soc., 143 (1996) 302.
- [203] T.L. Barr, Appl. Surf. Sci., 15 (1983) 1.
- [204] J. Finster, E.D. Klinkenberg, J. Heeg, Vacuum, 41 (1990) 1586.
- [205] C.S. Madi, H.B. George, M.J. Aziz, J. Phys.: Condens. Matter, 21 (2009) 224010.
- [206] S.A. Pahlovy, S.F. Mahmud, K. Yanagimoto, I. Miyamoto, J. Vac. Sci. Technol.,A, 29 (2011) 021015.
- [207] C.S. Madi, M.J. Aziz, Appl. Surf. Sci., 258 (2012) 4112.
- [208] T. Basu, J.R. Mohanty, T. Som, Appl. Surf. Sci., 258 (2012) 9944.
- [209] M. Engler, T. Michely, Phys. Rev. B, 93 (2016) 085423.
- [210] D. Chowdhury, D. Ghose, S.A. Mollick, Vacuum, 107 (2014) 23.
- [211] G.W. Lewis, G. Kiriakides, G. Carter, M.J. Nobes, Surf. Interface Anal., 4 (1982) 141.
- [212] G. Carter, G.W. Lewis, M.J. Nobes, J. Cox, W. Begemann, Vacuum, 34 (1984) 445-450.
- [213] S. Bhattacharjee, P. Karmakar, A. Chakrabarti, Nucl. Instrum. Methods Phys. Res., Sect. B, 278 (2012) 58-62.
- [214] G. Carter, M.J. Nobes, Vacuum, 45 (1994) 539-546.
- [215] G. Carter, V. Vishnyakov, Y.V. Martynenko, M.J. Nobes, J. Appl. Phys., 78 (1995) 3559.
- [216] T.K. Chini, M.K. Sanyal, S.R. Bhattacharyya, Phys. Rev. B, 66 (2002) 153404.
- [217] T.K. Chini, F. Okuyama, M. Tanemura, K. Nordlund, Phys. Rev. B, 67 (2003) 205403.
- [218] T.K. Chini, D.P. Datta, S.R. Bhattacharyya, J. Phys.: Condens. Matter, 21 (2009) 224004.
- [219] D.P. Datta, T.K. Chini, Phys. Rev. B, 69 (2004) 235313.
- [220] D.P. Datta, T.K. Chini, Phys. Rev. B, 71 (2005) 235308.

- [221] S. Hazra, T.K. Chini, M.K. Sanyal, J. Grenzer, U. Pietsch, Phys. Rev. B, 70 (2004) 121307.
- [222] T. Kumar, A. Kumar, D.C. Agarwal, N.P. Lalla, D. Kanjilal, Nanoscale Res. Lett., 8 (2013) 336.
- [223] M.Y. Bashouti, K. Sardashti, J. Ristein, S. Christiansen, Nanoscale Res. Lett., 8 (2013) 41.
- [224] M. Paul, D. Berkovits, I. Ahmad, F. Borasi, J. Caggiano, C.N. Davids, J.P. Greene, B. Harss, A. Heinz, D.J. Henderson, W. Henning, C.L. Jiang, R.C. Pardo, K.E. Rehm, R. Rejoub, D. Seweryniak, A. Sonzogni, J. Uusitalo, R. Vondrasek, Nucl. Instrum. Methods Phys. Res., Sect. B, 172 (2000) 688.
- [225] S. Momota, Y. Nojiri, M. Saihara, A. Sakamoto, H. Hamagawa, K. Hamaguchi, Rev. Sci. Instrum., 75 (2004) 1497.
- [226] H. Koivisto, J. Arje, R. Seppala, M. Nurmi, Nucl. Instrum. Methods Phys. Res., Sect. B, 187 (2002) 111.
- [227] A.J. Kinloch, K.T. Tan, F. Watts, The Journal of Adhesion, 82 (2006) 1117-1132.
- [228] X.-r. Yu, H. Hantsche, Surf. Sci. and interface analysis, 20 (1993) 555.
- [229] Y. Homma, A. Takano, Y. Higashi, Appl. Surf. Sci., 203-204 (2003) 35-38.
- [230] V.K.Smirnov, D.S.Kibalov, S.A.Krivelevich, P.A.Lepshin, E.V.Potapov, R.A.Yankov, W.Skorupa, V.V.Makarov, A.B.Danilin, Nucl. Instrum. Methods Phys. Res. B 147 (1999) 310.
- [231] S.A. Mollick, D. Ghose, J. Appl. Phys., 106 (2009) 044309.
- [232] Z.X. Liu, P.F.A. Alkemade, Appl. Phys. Lett., 79 (2001) 4334.
- [233] T.J. Novakowski, J.K. Tripathi, A. Hassanein, J. Vac. Sci. Technol. B, 36 (2018) 051202.